2019

Physics and applications of exceptional points

Qi Zhong
Michigan Technological University, qizhong@mtu.edu

PHYSICS AND APPLICATIONS OF EXCEPTIONAL POINTS

By

Qi Zhong

A DISSERTATION

Submitted in partial fulfillment of the requirements for the degree of

DOCTOR OF PHILOSOPHY

In Physics

MICHIGAN TECHNOLOGICAL UNIVERSITY

2019

This dissertation has been approved in partial fulfillment of the requirements for the Degree of DOCTOR OF PHILOSOPHY in Physics.

Department of Physics

Dissertation Advisor:	*Dr. Ramy El-Ganainy*
Committee Member:	*Dr. Miguel Levy*
Committee Member:	*Dr. Jae Yong Suh*
Committee Member:	*Dr. Durdu Guney*
Department Chair:	*Dr. Ravindra Pandey*

Dedication

To my physics teachers in my life

who provided their shoulders for me to stand on to see further.

Contents

List of Figures

Preface

In this dissertation, I will present my work on theory and applications of exceptional points in non-Hermitian and parity-time-(PT-)symmetric systems. First chapter gives a brief introduction of PT symmetry and exceptional points (EPs). Chapter 2 is reproduced from the paper *Physical Review A 97 (2), 020105 (2018).* Chapter 3 is reproduced from the paper *Scientific Reports 9 (1), 134 (2019).* Chapter 4 is reproduced from the paper *Nature Communications 9 (1), 4808 (2018).* Chapter 5 is reproduced from the paper *Physical Review Letters 122 (15), 153902 (2019).* Chapter 6 is based on a manuscript (*arXiv:1904.13005*) accepted by Physical Review Applied.

All the work in the dissertation was supervised by Prof. Ramy El-Ganainy in Department of Physics.

Acknowledgments

Firstly, I would like to express my sincere gratitude to my advisor Prof. Ramy El-Ganainy for the continuous support of my Ph.D. study and related research, for his patience, motivation, and immense knowledge. In the last three years, we had numerous discussions on the project we were working and some other scientific topics, which developed my professional skills and enriched my knowledge in all respects. Prof. El-Ganainy also encouraged me to attend academic conferences and introduced me to his colleagues.

I would also like to thank the finical support and the service from the China Scholarship Council (CSC). I also appreciate the help from consuls Lei Jin, Hao Chen, and Shaohua Zhang in Consulate-General of the People's Republic of China in Chicago, and Pengfei Qiu in Nanjing University when I changed the study program.

I appreciate Prof. Robert Nemiroff and Department chair Prof. Ravindra Pandey for their support when I switched to physics department. And I learned a lot from Prof. Nemiroff in the two years when I was under the supervision of him. During five years in Physics department and Michigan Tech, the support and help are everywhere and countless, just like the real numbers in the range of $[2014, 2019]$. I would like to acknowledge the support from Henes Center for Quantum Phenomena, Graduate

Student Government for travel grants, and Graduate School for Doctoral Finishing Fellowships. Special thanks to Prof. Jacek Borysow, Prof. Yoke Khin Yap, Prof. Alex Kostinski and Wil Slough.

I would like to thank all my committee members Prof. Miguel Levy, Prof. Jae Young Suh and Prof. Durdu Guney, for the time and efforts on revising and commenting on my thesis.

I would also like to thank Prof. Demetrios Christodoulides for his guidance and hospitality during my exchange visit at CREOL, the College of Optics and Photonics at the University of Central Florida.

Last but not least, I would like to thank my parents, my sister and my dearest wife, for their support all the time.

List of Abbreviations

2D	Two-Dimentional
BC	Branch Cut
BPT	Broken Parity-Time
CW	Clockwise
CCW	Counterclockwise
DP	Diabolic Point
EP	Exeptional Point
ES	Exceptional Hypersurface
EPN	Exceptional Points of order N
FDTD	Finite Difference Time Domain
FWHM	Full Width at Half Maximum
MI	Mott Insulator
OA	Optical Amplifier
PT	Parity-Time
SF	Superfluid
SMM	Scattering Matrix Method
SVD	Singular Value Decomposition
TCMT	Temporal Coupled Mode Theory

Abstract

Exceptional points (EPs) are singularities that arise in non-Hermitian physics. Crossing EPs is believed to be related with phase transitions between parity-time-(PT-)symmetric phase and broken PT phase. Owing to their peculiar topology, EPs can remotely induce observable effects when encircled by closed trajectories in the parameter space. In this dissertation, first of all, we investigate the extreme dynamics of non-Hermitian systems near higher order EPs constructed using the bosonic algebra method. The strong power oscillations for certain initial conditions can occur as a result of the peculiar eigenspace geometry and its dimensionality collapse near these singularities. And in the PT phase near EPs, the logarithm of the maximum optical power amplification scales linearly with the order of EPs. Secondly, we show that the theoretical framework linking EPs to phase transitions in PT-symmetric Hamiltonians is incomplete. Particularly, the application of the squaring operator to a J_x PT lattice can result in a system that can cross an EP without undergoing a symmetry breaking, which is elucidated by invoking the notion of phase diagrams in the parameter space. We also develop a general approach for encircling EPs by utilizing permutation operators and the representation theory, and reveal that loops that enclose the same EPs starting from the same point and traveling in the same direction, do not necessarily share the same end outcome. Instead, this equivalence can be established by invoking the topological notion of homotopy. All these findings

are general with far reaching implications in various fields ranging from photonics and atomic physics to microwaves and acoustics.

In the aspect of applications, current research efforts focus only on systems supporting isolated EPs characterized by increased sensitivity to external perturbations, which makes them potential candidates for building next generation optical sensors. On the downside, they are very sensitive to fabrication errors and experimental uncertainties. To overcome this problem, we propose a photonic structure exhibits a hypersurface of EPs embedded in a larger space, in which perturbations due to back reflection/scattering force the operating point out of the exceptional surface, leading to enhanced sensitivity. Also, this proposed structure can relax the finite gain-bandwidth product limitation in optical amplifiers and allows for building a new generation of optical amplifiers that exhibits better gain-bandwidth scaling relations.

Chapter 1

Introduction

Physics is a subject that tries to reveal the principle of how the universe works and mathematics is its fundamental and powerful tool. In a mathematical model of a physics system, the behavior at some points, not in the real space but in the parameter space, can be completely and fundamentally different compared to their neighboring points. These critical points are called singularities and the most famous two examples are the initial singularity (the starting point of universe) in the Big Bang model and the gravitational singularity in black holes based on general relativity. In this dissertation, we will deal with one kind of singularity called exceptional points (EPs) at which two or more eigenvalues and their corresponding eigenvectors simultaneously coalesce. Exceptional points are singularities that arise in non-Hermitian systems

that exchange energy with their surrounding environment. A particular group of non-Hermitian systems respecting parity-time (PT) symmetry can exhibit real eigenvalues, a feature that is believed can only exist in Hermitian systems. More interesting, a PT-symmetric system can experience the transition between PT phase and broken PT phase when crossing EPs.

In last decades, tremendous progresses have been made, both in theory and experimental implementations of non-Hermitian systems in different platforms, such as photonics, atomic physics, and acoustics. For more information, see recent reviews[1, 2, 3, 4]. The theoretical results about exceptional points, in Chapter 2, 3 and 4, are explained with the help of optical platforms, however, these finds are general with far reaching implications in various fields. The experimental designs in the Chapter 4 and 5 use optical devices directly. In this chapter, a brief introduction on non-Hermitian physics, PT-symmetric photonics and exceptional points is presented.

1.1 Non-Hermitian physics and PT symmetry

1.1.1 Non-Hermitian physics

In closed physical systems, conservation of energy is the most fundamental condition. In quantum physics, this requirement demands that the Hamiltonian H should

be Hermitian, namely $H^\dagger = H$ and the symbol '†' stands for Hermitian conjugate. Hamiltonians can be written in the form of matrices for discrete systems in the Heisenberg picture. Mathematically, the Hermitian conjugate of a matrix is the transposed conjugate, that is $H^\dagger \equiv (H^*)^\mathsf{T}$, in which '*' is complex conjugate and 'T' is transpose. A Hermitian Hamiltonian can guarantee that its eigenvalues must be real and its eigenstates are orthogonal with each other.

As mentioned before, Hermitian condition is based on the ideal assumption of complete isolation of a system from its surrounding environment. However, in many situations, the studied system would inevitably exchange energy with its environment, resulting in a non-Hermitian Hamiltonian. Non-Hermitian Hamiltonians have complex eigenvalues and the imaginary part of eigenvalues stand for the gain or loss rate of the system, since the solution can be written in the basis of $\exp(-i\lambda_n t) = \exp[-i\mathrm{Re}(\lambda_n)t]\exp[\mathrm{Im}(\lambda_n)t]$. Note that photonics is a nature good candidate for engineering non-Hermitian Hamiltonians, since dissipation is ubiquitous in optics, arising from material absorption as well as radiation leakage. On the other hand, gain can be implemented by optical or electrical pumping or through parametric processes.

An important milestone in the theory of non-Hermitian physics was the discovery, by Carl Bender and Stefan Boettcher, that a large class of non-Hermitian Hamiltonians can exhibit entirely real spectra as long as they respect parity-time (PT) symmetry

[5]. The introduction of PT symmetry concept later in optics, has led to an explosion of research activities[6]. Before this, loss exists naturally in photonics and is believed as a bad factor. Now, researchers introduce loss in purpose to engineer the system to explore the exotic features that can not be achieved in Hermitian system.

1.1.2 Parity-time (PT) symmetry

In the context of quantum mechanics, symmetries describe features of spacetime and particles which are unchanged under some transformation, which are also denoted as operators $\hat{O}$. Parity symmetry corresponds to a parity transformation $\hat{P}$, which is the flip of the sign of spatial coordinates. In addition, the time reversal symmetry corresponds to time reversal operator $\hat{T}$, which reverses the flow of time as the name implies. The $\hat{P}$ operator, $\hat{T}$ operator and their combination $\hat{P}\hat{T}$ operator are illustrated as below:

$$\begin{cases} \hat{P} : (x, y, z, t) \rightarrow (-x, -y, -z, t) \\ \hat{T} : (x, y, z, t) \rightarrow (x, y, z, -t) \\ \hat{P}\hat{T} : (x, y, z, t) \rightarrow (-x, -y, -z, -t) \end{cases} \tag{1.1}$$

In quantum mechanics, momentum operator $\hat{p}$, position operator $\hat{r} = (\hat{x}, \hat{y}, \hat{z})$ and the unit imaginary number i are widely used and their transformation under $\hat{P}\hat{T}$ operator

are:

$$\hat{P}\hat{T} : \hat{p} \to \hat{p}, \hat{r} \to -\hat{r}, i \to -i \tag{1.2}$$

A Hamiltonian respecting parity-time (PT) symmetry means it commute with the parity-time operator $\hat{P}\hat{T}$, that is $[\hat{H}, \hat{P}\hat{T}] = 0$. For the sake of illustration, let us consider the Schrödinger equation for a single particle in one-dimensional (1D) space:

$$i\hbar\frac{\partial}{\partial t}\psi(x,t) = \hat{H}\psi(x,t),\ \hat{H} = \frac{\hat{p}^2}{2m} + \hat{V}(x), \tag{1.3}$$

where the momentum operator is $\hat{p} = i\hbar\dfrac{\partial}{\partial x}$, and $\hat{V}(x)$ is related with the potential function $V(x)$. In general, the potential function $V(x)$ is a real-valued function of x, however, here it should be treated as a complex function for more general cases. The transformation of Hamiltonian $\hat{H}$ under the $\hat{P}\hat{T}$ operator is

$$\hat{H} = \frac{\hat{p}^2}{2m} + \hat{V}(x) \xrightarrow{\hat{P}\hat{T}} \hat{H}' = \frac{\hat{p}^2}{2m} + \hat{V}^*(-x) \tag{1.4}$$

It can be shown that a necessary condition for PT symmetry to hold ($\hat{H} = \hat{H}'$) is that the complex potential satisfy $V^*(-x) = V(x)$, which means the real and imaginary part of $V(x)$ is an even and odd function, respectively. In addition, the physics meaning of imaginary part of $V(x)$ is the gain or loss of the system. It can be proven that the condition of $V^*(-x) = V(x)$ is equivalent to $[\hat{H}, \hat{P}\hat{T}] = 0$.

PT symmetry attracted much attention and is becoming a much concerned forefront direction since it was proposed in 1998 by Carl Bender and Stefan Boettcher [5], partially because it reveals that real-valued spectrum can exist in PT-symmetric Hamiltonian, which was believed can only exist in Hermitian Hamiltonian. Even though the potentials in PT-symmetric Hamiltonian are complex, the real-value spectrum means these systems can be experimentally observed. It needs to be emphasized that a PT-symmetric Hamiltonian does not guarantee real eigenvalues. In the parameter space of a PT-symmetric Hamiltonian, the eigenvalues are real in some regions, while are complex in some other regions, denoted as PT phase and broken PT phase, which will be discussed in detail in next section.

1.1.3 PT phase and broken PT phase

As mention above, it has been realized that a PT-symmetric Hamiltonian $\hat{H}$, defined by $[\hat{H}, \hat{P}\hat{T}] = 0$, is not sufficient to ensure a real spectrum, as formally PT-symmetric Hamiltonians can undergo a phase transition to the spontaneously broken symmetry regime, in which complex eigenvalues appear.

Suppose a PT-symmetric Hamiltonian $\hat{H}$ only has two eigenstate ψ_1 and ψ_2 with corresponding eigenvalues $\lambda_1 \neq \lambda_2$, that is $\hat{H}\psi_{1,2} = \lambda_{1,2}\psi_{1,2}$. Since $[\hat{H}, \hat{P}\hat{T}] = 0$, we

can do the following derivation:

$$\begin{aligned} \hat{H}(\hat{P}\hat{T}\psi_1) &= \hat{P}\hat{T}\hat{H}\psi_1 \\ &= \hat{P}\hat{T}\lambda_1\psi_1 \\ &= \lambda_1^*(\hat{P}\hat{T}\psi_1). \end{aligned} \tag{1.5}$$

Similar for ψ_2. It is clear that the two new states $\hat{P}\hat{T}\psi_{1,2}$ are also eigenstates of H with eigenvalues $\lambda_{1,2}^*$. Therefore, one solution is $\hat{P}\hat{T}\psi_{1,2} = \psi_{1,2}$ (neglect the phase change of $\psi_{1,2}$) and $\lambda_{1,2}^* = \lambda_{1,2}$, indicating $\lambda_{1,2}$ are real values. In this case, we say $\psi_{1,2}$ respect PT symmetry and the system is at PT-symmetric phase or PT phase for short. On the other hand, another possible solution is $\hat{P}\hat{T}\psi_{1,2} = \psi_{2,1}$ and $\lambda_{1,2}^* = \lambda_{2,1}$, indicating applying $\hat{P}\hat{T}$ operator to one eigenstate yields another eigenstate, and $\lambda_{1,2}$ are complex numbers and complex conjugate with each other. In this scenario, the system is at broken PT (BPT) phase even though the Hamiltonian H still respects PT symmetry. The PT-symmetric Hamiltonian $\hat{H}$ can vary with one or multiple parameters, and parameter points at which the phase transition between PT and BPT phase happen are called exceptional points (EPs). Exceptional points are singularities in non-Hermitian Hamiltonians and will be described in detail later in this chapter.

1.2 PT symmetry in optics

The above discussion about non-Hermitian physics, PT symmetry and PT phase is based on quantum mechanics, but these results are generally applicable to all fields in physics. To explore the features and properties of aforementioned exceptional points, which is also the keyword of this dissertation, we need to use a specific optical model to illustrate the role of EPs. Before that, we will discuss the PT symmetry in optics first in this section.

Optics and photonics have proven to be the ideal platform to experimentally observe the PT symmetry, since the key point of PT symmetry is tunning the gain and loss of the system and this is easy to achieved in optics. Dissipation is ubiquitous in optics, such as material absorption and radiation leakage to the environment. In addition, gain can be implemented through stimulated emission, which involves optical or electrical pumping of energy through an external source, or through parametric processes in nonlinear optics.

The optical analog of PT-symmetric quantum mechanics was first proposed in 2007 [7] and then experimentally observed in 2010 [8]. Experimental study on PT-symmetric classical optical systems has stimulated many applications such as loss-induced transparency [9], non-reciprocal light propagation [10, 11], and PT-symmetric single-mode

lasers [12, 13]. For more information, see recent reviews[1, 2, 3, 4].

Investigation of PT-symmetric optical setups was initiated by invoking the mathematical analogy between single-particle Schrödinger equation in Eq. (1.3) and the paraxial equation of electromagnetic wave propagation under the slowly varying envelope approximation [2]:

$$i\frac{\partial}{\partial z}E(x,z) = \left[-\frac{1}{2k_0 n_0}\frac{\partial^2}{\partial x^2} + V(x)\right]E(x,z), \tag{1.6}$$

where the propagation distance z along the optical axis plays the role of time, $E(x,z)$ is the transverse component of the electric field, k_0 is the free-space wavevector and $V(x) = k_0 n(x)$ is the complex optical potential with the background index n_0. Similar to $V(x) = V^*(-x)$ in Eq. (1.3), the PT symmetry condition requires $n(x) = n^*(-x)$, as illustrated in Fig. 1.1 (a).

A simplified and discretized version of PT-symmetric optical setups is implemented by two coupled waveguides or two coupled microcavities, as shown in Fig. 1.1 (b) and (c). In this dissertation, Chapter 3, 4 and 5 involve the coupled waveguides structure and we will give a simple description on this here.

Within the optical coupled mode formalism, the dynamic evolution of electric field $E_i = a_i \exp(i\omega t - i\beta z)$ $(i = 1, 2)$ in two coupled identical waveguides can be described

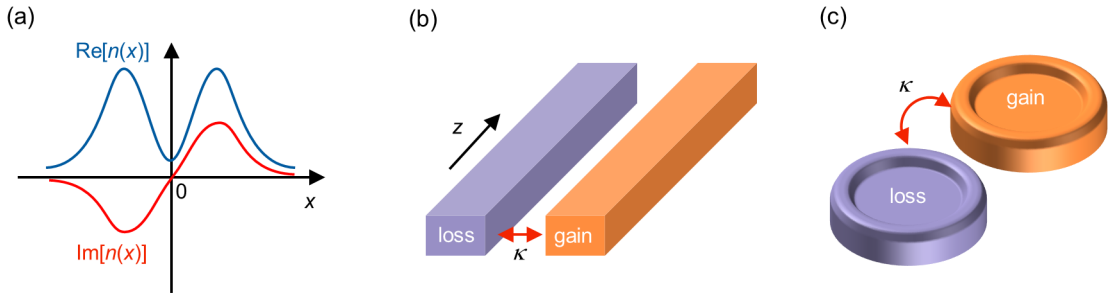

Figure 1.1: (a) PT symmetry requires $n(x) = n^*(-x)$, which means $\mathrm{Re}[n(x)]$ is an even function while $\mathrm{Im}[n(x)]$ is an odd function. Two typical photonic implementations of PT symmetry are (b) coupled waveguides and (c) coupled microcavities.

by:

$$\begin{cases} i\dfrac{da_1}{dz} = \kappa a_2 + (\beta_0 - ig)a_1, \\ i\dfrac{da_2}{dz} = \kappa a_1 + (\beta_0 + ig)a_2, \end{cases} \tag{1.7}$$

where $a_{1,2}$ represent field amplitudes in waveguide 1 and 2, κ is the coupling coefficient between these two waveguides, and β_0 is the propagation constant for passive waveguides. Waveguide 1 experiences loss $-g$, while waveguide 1 is applied with gain g. We can rewrite Eq. (1.7) in the form

$$\begin{aligned} i\frac{d}{dz}\boldsymbol{a} &= H\boldsymbol{a}, \\ H &= \begin{bmatrix} \beta_0 - ig & \kappa \\ \kappa & \beta_0 + ig \end{bmatrix}. \end{aligned} \tag{1.8}$$

In the real domain of g and κ(we will discuss the situation when g and κ in the complex domain in Chapter 4), this effective Hamiltonian H respects PT symmetry when since H is invariant under the operation: $\hat{P}$ $(a_1 \leftrightarrow a_2)$ and $\hat{T}$ $(i \to -i)$. The eigenvalues of

H are $\lambda_{1,2} = \beta_0 \pm \sqrt{\kappa^2 - g^2}$ and the associated eigenvectors are $\boldsymbol{v}_{1,2} = (1, \pm e^{\pm i\theta})$ with $\theta = \arcsin(g/\kappa)$. Both eigenvalues are real and the eigenvectors satisfy $\hat{P}\hat{T}\boldsymbol{v}_{1,2} = \boldsymbol{v}_{1,2}$ (neglecting the phase term) in the domain $g \in [0, \kappa)$, while the eigenvalues become complex conjugate and the eigenvectors satisfy $\hat{P}\hat{T}\boldsymbol{v}_{1,2} = \boldsymbol{v}_{2,1}$ (neglecting the phase term) in the domain $g \in (\kappa, +\infty)$. And the critical point $g = \kappa$ separating these two domain, or PT phase and broken PT phase as mentioned, are called exceptional point (EP). The physical model in Eq. (1.8) is the cornerstone of the context in Chapter 2, 3 and 4.

1.3 Exceptional points in non-Hermitian physics

In the previous section, the concept of exceptional points was introduced naturally in the PT-symmetric coupled waveguides. In PT-symmetric systems, exceptional points separate PT phase and broken PT phase. And at the EP ($g = \kappa$) of the Hamiltonian in Eq. (1.8), the two eigenvalues and their corresponding eigenvectors simultaneously coalesce to $\lambda_{1,2} = \beta_0$ and $\boldsymbol{v}_{1,2} = (1, i)^{\mathsf{T}}$. This exceptional point is also called a second-order EP, and an Nth-order EP is formed by the coalescence of N eigenvectors. In contrast with exceptional points, a similar concept called diabolic point (DPs) also cause the degeneracy of eigenvalues but the eigenstates still remain orthogonal. The incompleteness of the eigenbases at EPs leads to peculiar consequences and will be discussed in Chapter 2.

Despite that we introduced the notion of exceptional points through a PT-symmetric Hamiltonian, EPs are ubiquitous in non-Hermitian systems. The mathematical reason behind this is that the solution of eigenvalues for non-Hermitian Hamiltonian associates with multivalued complex functions, which holds a kind of singularities called branch points universally [14]. And exceptional points are referred to branch points.

Recently, the exotic features of EPs have been subject of intense studies[7, 8, 15, 16] with various potential applications in laser science[12, 13, 17, 18], optical sensing[19, 20, 21], photon transport engineering[22, 23] and nonlinear optics[24, 25] just to mention few examples.

Chapter 2

Power-law scaling of extreme dynamics near exceptional points

2.1 Introduction

One of the intriguing features of non-Hermitian Hamiltonians is the breakdown of eigenstate orthogonality (as defined by the Hermitian inner product) [26]. In the most extreme case, two or more distinct eigenstates can even become identical (share the same eigenvalue and eigenvector), giving rise to eigenspace dimensionality collapse at the so called exceptional points (EPs) [27, 28, 29, 30, 31, 32]. An exceptional point

The contents in this chapter were previously published in Physical Review A 97 (2), 020105 (2018). Refer Appendix A.1 for granted permission to be republished.

of order N (denoted as EPN) is formed by the coalescence of N eigenvectors to form an 'exceptional vector'. The incompleteness of the eigenbases at these special points leads to important consequences such as the divergence of Petermann factor [33, 34, 35, 36, 37] and ultra-sensitivity to external perturbations [19, 38]. While systems exhibiting EP2 have been intensively investigated both at the theoretical and experimental levels, higher order EPs (mostly of order three) have so far received little attention [39, 40, 41, 42, 43, 44, 45], partly due to implementation difficult in the laboratory. Recently however, two groundbreaking experimental works have successfully demonstrated systems operating at a third order exceptional point using acoustic [46] and optical [20] platforms. More complex schemes supporting even higher order exceptional points can be constructed by using bosonic algebra [41].

Even though higher order EPs are expected to demonstrate most of the general features of their counterpart second order singularities, a quantitative description of the extreme dynamics near EPN is still lacking. In particular, power oscillations near EP2 in parity-time- (PT-) symmetric systems have been investigated in [7, 15, 16, 47]. Additionally, transient power growth in non-Hermitian optical setups have been recently studied using pseudo-spectrum techniques [48]. Here we investigate the extreme dynamics in PT-symmetric [5, 8, 9, 11, 12, 13, 22, 49, 50, 51, 52, 53, 54, 55, 56, 57, 58, 59] Hamiltonian having higher order EPs [41].

By employing complementary numerical and analytical approaches, we are able to

quantify the maximum value of the extreme optical power amplification for any higher order EPN when the system approaches it from the PT phase. The main results of this work are: (1) establishing the link between the dynamical evolution near EPs and the geometry of the eigenbases associated with the underlying PT system; (2) demonstrating that the maximum power amplification follow a power-law dependence on the order N of the EP. Though our results are very general, for illustration purpose, we concentrate in our discussion on photonic implementations.

In the remaining of this chapter, for sake of generality we use dimensionless quantities. Physical parameters can be always calculated depending on the details of the physical system of interest.

2.2 Power oscillations near exceptional points: a geometric perspective

2.2.1 General solutions for coupled optical arrays

Consider a discrete non-Hermitian Hamiltonian H of dimensions $N \times N$ (we do not treat infinite dimensions cases here). Within the optical coupled mode formalism, this Hamiltonian can describe for example an array of coupled waveguides or resonators,

and will obey the equation $i\frac{d\boldsymbol{a}}{dz} = H\boldsymbol{a}$. Here $\boldsymbol{a} = (a_0, a_1, ..., a_{N-1})^{\mathrm{T}}$ is the electric field amplitude vector and, assuming coupled waveguides, z is the propagation distance (for coupled cavities, z is replaced by the evolution time t). Suppose $\boldsymbol{e}_k$ are the right eigenvectors of H. Non-orthogonality implies that $\langle \boldsymbol{e}_k, \boldsymbol{e}_l \rangle = \boldsymbol{e}_k^* \cdot \boldsymbol{e}_l \neq 0$ where $\langle\rangle$ is the Hermitian inner product, the symbol '$*$' is the complex conjugate and '$\cdot$' denotes the vector product without any further conjugation. A non-Hermitian inner product that restores orthogonality (also called biorthogonality) can be also defined: $\langle \tilde{\boldsymbol{e}}_k, \boldsymbol{e}_l \rangle = \boldsymbol{e}_k \cdot \boldsymbol{e}_l = 0 (k \neq l)$, where $\tilde{\boldsymbol{e}}_k = \boldsymbol{e}_k^*$ is the transpose of the left eigenvectors of H.

The general solution for the equation of motion for H is $\boldsymbol{a}(z) = \sum_{k=1}^{N} C_k \boldsymbol{e}_k \exp(-i\lambda_k z)$, where λ_k are eigenvalues of H and the coefficients C_k are determined by the initial condition $\boldsymbol{a}_I = \boldsymbol{a}(z=0) = \sum_{k=1}^{N} C_k \boldsymbol{e}_k$. In the rest of this chapter, we will use the normalization $\langle \boldsymbol{e}_k, \boldsymbol{e}_k \rangle = \langle \boldsymbol{a}_I, \boldsymbol{a}_I \rangle = 1$. As a direct outcome of the non-Hermiticity, the total power $P(z) \equiv \langle \boldsymbol{a}(z), \boldsymbol{a}(z) \rangle$, is not conserved but rather varies along the propagation distance. In non-Hermitian systems that do not exhibit gain, the evolution of $P(z)$ will be decaying oscillations. We are interested mainly in the oscillatory part which, in some cases, can be isolated by a simple gauge transformation that results in PT-symmetric Hamiltonian [9]. The oscillatory behavior of these systems can be quantified either by using the total power behavior $P(z)$ or its z averaged value $\langle P \rangle \equiv \frac{1}{L}\int_0^L P(z)dz$, where for perfect periodic variation L is the period of one

cycle and otherwise $L \to \infty$. In this section we will use the latter to develop the geometric intuition behind the phenomena of extreme power oscillation near EPs. An obvious advantage of using $\langle P \rangle$ is its direct dependence on the coefficients C_k: $\langle P \rangle = \sum_{k=1}^{N} |C_k|^2$. By considering the geometry of the non-orthogonal eigenbases, we now show that the quantity $\langle P \rangle$ takes large values in the vicinity of an exceptional point, which in turn indicates large oscillatory amplitudes.

2.2.2 Geometric perspective

Let us first focus on the simple case of second order exceptional point, EP2. As demonstrated in Fig. 2.1(a), in an orthogonal coordinate system (left panel) the projections of any vector cannot exceed the length of the vector itself. On the other hand, if the two basis vectors are almost parallel, a vector which is nearly orthogonal to the bases can exhibit very large projection coefficients, diverging in the limit when the two base vectors become identical thus signaling the incompleteness of the bases. This argument can be generalized to higher dimensions as demonstrated schematically in Fig. 2.1(b). Particularly, if an $N \times N$ Hamiltonian H exhibits an exceptional point of order N, EPN, all the eigenvectors of H become nearly 'parallel' to the exceptional vector $\boldsymbol{v}_{\mathrm{e}}$ (the notion of parallel vectors is defined here in the Hermitian sense). Thus the projection coefficients of a vector $\boldsymbol{a}_I$ which lies in $N-1$ hyperplane orthogonal to $\boldsymbol{v}_{\mathrm{e}}$ are large, implying a large value of $\langle P \rangle$. This behavior can be also understood by

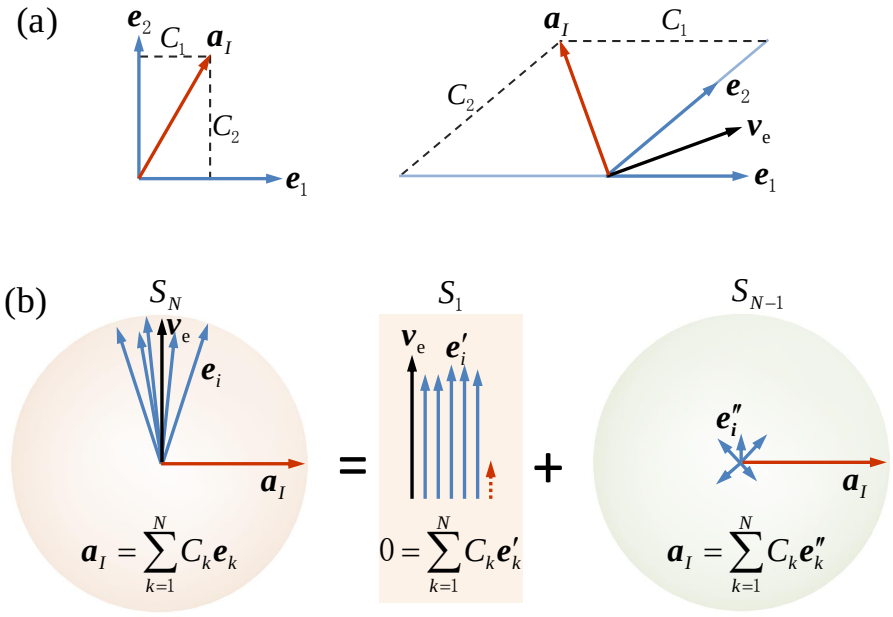

Figure 2.1: Geometric intuitive illustration of the origin of extreme fluctuations in the vicinity of exceptional points in two and N dimensional spaces as described in details in the text are depicted in panels (a) and (b), respectively. In (b), the vectors $\boldsymbol{e}_i'$ and $\boldsymbol{e}_i''$ are components of $\boldsymbol{e}_i$ in the directions parallel and perpendicular to $\boldsymbol{v}_e$, respectively. Since the components $\boldsymbol{e}_i''$ are small and the vector $\boldsymbol{a}_I$ is orthogonal to $\boldsymbol{v}_\mathrm{e}$, it follows that the coefficients C_k must have large values.

using the notion of biorthogonality. Particularly, since $C_k = \langle \tilde{\boldsymbol{e}}_k, \boldsymbol{a}_I \rangle \,/\, \langle \tilde{\boldsymbol{e}}_k, \boldsymbol{e}_k \rangle$ and by noting that the 'complex length' of the exceptional vector (i.e. the quantity $\sqrt{\langle \tilde{\boldsymbol{v}}_\mathrm{e}, \boldsymbol{v}_\mathrm{e} \rangle}$) is zero, it is clear that C_k becomes larger when $\boldsymbol{e}_k \sim \boldsymbol{v}_\mathrm{e}$ as long as $\langle \tilde{\boldsymbol{e}}_k, \boldsymbol{a}_I \rangle > \langle \tilde{\boldsymbol{e}}_k, \boldsymbol{e}_k \rangle$ which can happen when $\boldsymbol{a}_I \perp \boldsymbol{v}_\mathrm{e}$ (though this is not necessarily guaranteed for all vectors in the orthogonal subspace).

2.2.3 An example of H with EPN

Having presented this intuitive picture, we next proceed by considering a concrete example of PT symmetric Hamiltonians having higher order exceptional points [41]:

$$H_N = \begin{bmatrix} ig_0 & \kappa_0 & \dots & 0 & 0 \\ & & \vdots & & \\ \dots & \kappa_{n-1} & ig_n & \kappa_n & \dots \\ & & \vdots & & \\ 0 & 0 & \dots & \kappa_{N-2} & ig_{N-1} \end{bmatrix}, \tag{2.1}$$

where the non-Hermitian (gain or loss) and coupling coefficients follow the rules $g_n = g(2n - N + 1)$ and $\kappa_n = \kappa\sqrt{(n+1)(N-n-1)}$ (n=0,1,2,...,$N-1$), with the real-valued quantities g and κ representing scaling parameters. The reason for the unusual numbering of the matrix elements (starting from 0 instead of 1) will be clear in the next section. As has been shown in [41], H_N generalizes the canonical PT symmetric toy model H_2. Particularly, when $\tilde{g} \equiv g/\kappa < 1$, H_N is in the PT phase. The transition to the broken phase ($\tilde{g} > 1$) is marked by an Nth-order exceptional point at $\tilde{g} = 1$. Here we are interested in the situation where g approaches κ from below where the system is still in the PT phase.

One possible measure to characterize the relationship between the eigenvectors of H_N is the Hermitian angle [60, 61] which is defined between two complex vectors $\boldsymbol{v}$ and

$\boldsymbol{u}$ as $\cos\Theta(\boldsymbol{v},\boldsymbol{u}) \equiv \frac{|\langle \boldsymbol{v},\boldsymbol{u}\rangle|}{|\boldsymbol{v}||\boldsymbol{u}|}$ with $\Theta(\boldsymbol{v},\boldsymbol{u}) \in [0,\pi/2]$. Fig. 2.2 presents a comparison between the minimum Hermitian angle $\Theta_{\rm e}$ associated with the eigenvectors of H_N for different values of N. Note that $\Theta_{\rm e}$ is smaller for larger values of N, indicating a faster collapse of the eigenspace dimensionality as $\tilde{g} \to 1$. Consequently, one expects more 'violent' power oscillation for larger N values. In the following section, we confirm and quantify this behavior analytically.

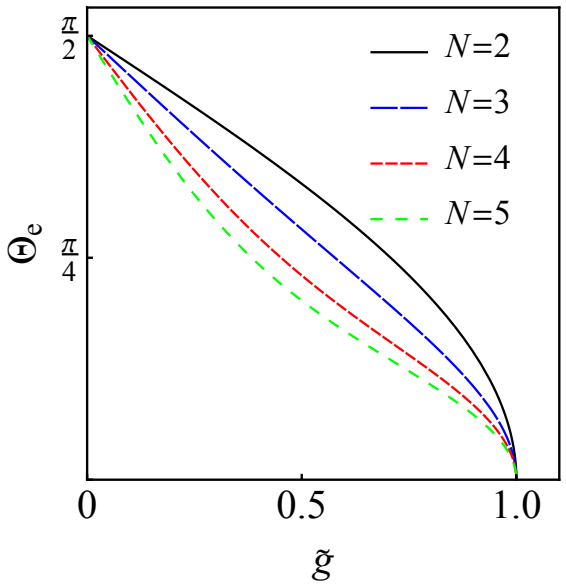

Figure 2.2: The minimum Hermitian angle $\Theta_{\rm e}$ between any two eigenvectors of the PT Hamiltonians H_N for different values of N as a function of the non-Hermitian parameter $\tilde{g}$. Clearly, $\Theta_{\rm e}$ is smaller for larger N, indicating faster eigenspace dimensionality collapse near higher order exceptional points. This in turn suggests that more 'violent' dynamics take place near EPN with higher orders. Our analysis in the next section confirms and quantifies this prediction.

2.3 Exact results using bosonic algebra

In this section, we employ the bosonic algebra method to study spectrum and propagation dynamics of a system described by H_N. In contrast to the previous section, here we focus on $P(z)$ rather than its z average.

2.3.1 Bosonic algebra

To do so, we consider the non-Hermitian two-side non-interacting Bose-Hubbard model that were used to construct H_N:

$$\hat{H} = -ig(\hat{b}_1^\dagger \hat{b}_1 - \hat{b}_2^\dagger \hat{b}_2) + \kappa(\hat{b}_1^\dagger \hat{b}_2 + \hat{b}_1 \hat{b}_2^\dagger), \tag{2.2}$$

where $\hat{b}_{1,2}^\dagger$ and $\hat{b}_{1,2}$ are the bosonic creation and annihilation operators of oscillators 1 and 2, and we assumed $\hbar = 1$. In the bases $|N_p - n, n\rangle$ representing a Fock state with $N_p - n$ and n bosons in sites 1 and 2 respectively (i.e. a total number of N_p bosonic particles), the matrix representation of $\hat{H}$ is H_N [41], where $N = N_p + 1$.

Before we proceed, we emphasize that the model in Eq. (2.2) does not represent an actual PT symmetric quantum system [53, 62, 63, 64] but is rather used as a mathematical tool to facilitate the analysis. Motivated by the fact that the

Hamiltonian H_N is generated from $\hat{H}$ in Eq. (2.2) by populating the latter with N_p particles and by noting that $\hat{H}$ is obtained from quantizing H_2 [41], we now focus on the $\hat{H}$ and consider the following normalized input state at $z = 0$: $|I(q_1, q_2)\rangle = \frac{1}{\sqrt{N_p!}}(q_1\hat{b}_1^\dagger + q_2\hat{b}_2^\dagger)^{N_p}|0,0\rangle$ with $|q_1|^2 + |q_2|^2 = 1$. This state can be also cast in the form $|I(q_1, q_2)\rangle = \sum_{n=0}^{N_p} a_n |N_p - n, n\rangle$ with the expansion coefficients given by $a_n = \sqrt{\frac{N_p!}{(N_p-n)!n!}} q_1^{N_p-n} q_2^n$. Although this particular construction of $|I(q_1, q_2)\rangle$ does not span all the vector space when $N_p > 1$, we will see later that it suffices for our calculations.

The output state at distance z can be written as:

$$\begin{aligned} |O\rangle &= e^{-i\hat{H}z}|I\rangle \\ &= \frac{1}{\sqrt{N_p!}} e^{-i\hat{H}z}(q_1\hat{b}_1^\dagger + q_2\hat{b}_2^\dagger)^{N_p} e^{i\hat{H}z} e^{-i\hat{H}z}|0,0\rangle \\ &= \frac{1}{\sqrt{N_p!}}[e^{-i\hat{H}z}(q_1\hat{b}_1^\dagger + q_2\hat{b}_2^\dagger)e^{i\hat{H}z}]^{N_p}|0,0\rangle\,, \end{aligned} \tag{2.3}$$

where we used the fact that $e^{-i\hat{H}z}|0,0\rangle = |0,0\rangle$. Next we define $\hat{b}_{1,2}^\dagger(z) \equiv e^{-i\hat{H}z}\hat{b}_{1,2}^\dagger e^{i\hat{H}z}$, which leads to the equation of motion $i\frac{d}{dz}[\hat{b}_1^\dagger(z), \hat{b}_2^\dagger(z)]^{\mathrm{T}} = H_2[\hat{b}_1^\dagger(z), \hat{b}_2^\dagger(z)]^{\mathsf{T}}$, admitting the formal solution $[\hat{b}_1^\dagger(z), \hat{b}_2^\dagger(z)]^{\mathrm{T}} = e^{-iH_2 z}[\hat{b}_1^\dagger, \hat{b}_2^\dagger]^{\mathrm{T}} \equiv U(z)(\hat{b}_1^\dagger, \hat{b}_2^\dagger)^{\mathrm{T}}$. By substituting

in (2.3), we then obtain:

$$\begin{aligned} |O\rangle =& \frac{1}{\sqrt{N_p!}}[q_1\hat{b}_1^\dagger(z) + q_2\hat{b}_2^\dagger(z)]^{N_p}\,|0,0\rangle \\ =& \frac{1}{\sqrt{N_p!}}[q_1(z)\hat{b}_1^\dagger + q_2(z)\hat{b}_2^\dagger]^{N_p}\,|0,0\rangle\,, \\ =& \sum_{n=0}^{N_p} a_n(z)\,|N_p-n,n\rangle\,, \end{aligned} \tag{2.4}$$

where $a_n(z) = \sqrt{\dfrac{N_p!}{(N_p-n)!n!}}[q_1(z)]^{N_p-n}[q_2(z)]^n$ with the z dependent quantities $q_1(z) = q_1U_{11}(z) + q_2U_{21}(z)$ and $q_2(z) = q_1U_{12}(z) + q_2U_{22}(z)$ and the elements of $U(z) \equiv e^{-iH_2z}$ are:

$$U(z) = \begin{bmatrix} \cos(\lambda z) - \frac{g}{\lambda}\sin(\lambda z) & -i\frac{\kappa}{\lambda}\sin(\lambda z) \\ -i\frac{\kappa}{\lambda}\sin(\lambda z) & \cos(\lambda z) + \frac{g}{\lambda}\sin(\lambda z) \end{bmatrix}, \tag{2.5}$$

where $\lambda = \sqrt{\kappa^2 - g^2}$.

Note that within the coupled mode formalism of waveguides (or cavities) arrays, the states $|N_p - n, n\rangle$ represents waveguide number n while the coefficients $a_n(z)$ describe the associated field amplitudes (see [41] for more details). Therefore, the total power is given by $P(z) = \sum_{n=0}^{N-1}|a_n(z)|^2$. When the input power is taken to be unity, the expression for the maximum amplification thus becomes $G_N = \max[P_N(z)]$.

2.3.2 Search the maximum amplification in a subspace

For the case of $N = 2$, it is easy to show that, apart from a phase factor, the initial optimal vector leading to the maximum amplification is $\boldsymbol{a}_I^{\mathrm{opt}} = (q_1, q_2)^{\mathrm{T}} = \frac{1}{\sqrt{2}}(1, -i)^{\mathrm{T}}$. Under these condition, the power oscillations dynamics are given by:

$$P_2^{\mathrm{opt}}(z) = 1 + \frac{2\tilde{g}}{1-\tilde{g}} \sin^2(\lambda z), \tag{2.6}$$

and this initial condition let $G_2 = \frac{1+\tilde{g}}{1-\tilde{g}}$. Note that the Hermitian angle between $\boldsymbol{a}_I^{\mathrm{opt}}$ and $\boldsymbol{v}_{\mathrm{e}}$ is $\pi/2$, i.e., $\boldsymbol{a}_I^{\mathrm{opt}}$ is orthogonal to $\boldsymbol{v}_{\mathrm{e}}$, in agreement with the discussion in the previous section.

The general case for $N > 2$ is more subtle. In principle, one has to chose the optimal initial vector that results in the maximum amplification from the set of all initial conditions $|I'\rangle = \sum_{n=0}^{N_p} q_n (\hat{b}_1^\dagger)^{N_p-n} (\hat{b}_2^\dagger)^n |0,0\rangle$. The input state $|I\rangle$ however describes only a subset of all initial states. Within this subspace, the output is

$$\begin{aligned} P_N(z) &= \sum_{n=0}^{N_p} |a_n(z)|^2 \\ &= \sum_{n=0}^{N_p} \frac{N_p!}{(N_p-n)!n!} [|q_1(z)|^2]^{N_p-n} [|q_2(z)|^2]^n \\ &= (|q_1(z)|^2 + |q_2(z)|^2)^{N_p} \\ &= [P_2(z)]^{N-1} \end{aligned} . \tag{2.7}$$

It is straightforward to see that even when $N > 2$, the optimal vector still corresponds to $|I(q_1, q_2)\rangle$ with $(q_1, q_2) = \frac{1}{\sqrt{2}}(1, -i)$. In that case, the power dynamics and the maximum G_N are given by:

$$P_N^{\text{opt}}(z) = [1 + \frac{2\tilde{g}}{1-\tilde{g}} \sin^2(\lambda z)]^{N-1}, \tag{2.8}$$

and

$$G_N(\tilde{g}) = \max[P_N^{\text{opt}}(z)] = (\frac{1+\tilde{g}}{1-\tilde{g}})^{N-1}. \tag{2.9}$$

Note that here also $\boldsymbol{a}_I^{\text{opt}}$ is perpendicular to the exceptional vector $\boldsymbol{v}_{\text{e}}$ which in higher dimensions can be generated from the expression for $|I(q_1, q_2)\rangle$ by substituting $(q_1, q_2) = \frac{1}{\sqrt{2}}(1, i)$.

2.3.3 Confirm the global maximum by SVD

Even though Eq. (2.9) is derived by using a subset of all the possible initial conditions, we expect it to hold when all the possible initial conditions are considered since all the Hamiltonians H_N are generated from $\hat{H}$. To confirm this intuition, we will now employ a numerical technique based on singular value decomposition (SVD) to establish that the value of G_N as obtained by Eq. (2.9) indeed provide the global maximum [48]. This method is an exact optimization problem that determines the maximum

possible optimal amplification for any given propagation distance z by considering all possible initial conditions. Furthermore it determines the corresponding initial conditions that lead to such maximum power growth. In particular, it can be shown analytically that the maximum possible power amplification at a given z is equal to the largest singular value of the propagator of the problem or equivalently of the matrix norm of the propagator $e^{-iH_N z}$ (where the norm of a matrix M is generally defined $\|M\| \equiv \sup_{\boldsymbol{u}} \|M\boldsymbol{u}\|/\|\boldsymbol{u}\|$, where $\|\boldsymbol{u}\|$ is the usual Euclidean norm of the vector $\boldsymbol{u}$). In other words we have $G_N^{\text{opt}}(z) = ||e^{-iH_N z}||^2 = (\max[\sigma_N])^2$, where σ_N are the singular values associated with $e^{-iH_N z}$. The right singular eigenvector of the propagator determines the specific initial conditions that lead to the maximum amplification. The global maximum can be then found by maximizing $G_N^{\text{opt}}(z)$ with respect to z by scanning $z \in [0, L]$, to obtain $G'_N(\tilde{g}) = \max[G_N^{\text{opt}}(z)]$. Fig. 2.3(a) depicts the values of G'_N and G_N versus the order of the exceptional point N on a log scale. A prefect agreement is found between th value of G_N and the global maximum as obtained by SVD.

Eq. (2.9) is the central result of this work and demonstrating that maximum amplification is given by G_N and follows a power-law dependence on the order of the exceptional point, with oscillation dynamics becoming more pronounced for larger N. An interesting observation is that, when $\tilde{g} \sim 1$, one can recast G_N in the form: $G_N(K_2) = (4K_2)^{N-1}$, where $K_2 = (1 - \tilde{g}^2)^{-1}$ is the Petermann factor associated with H_2.

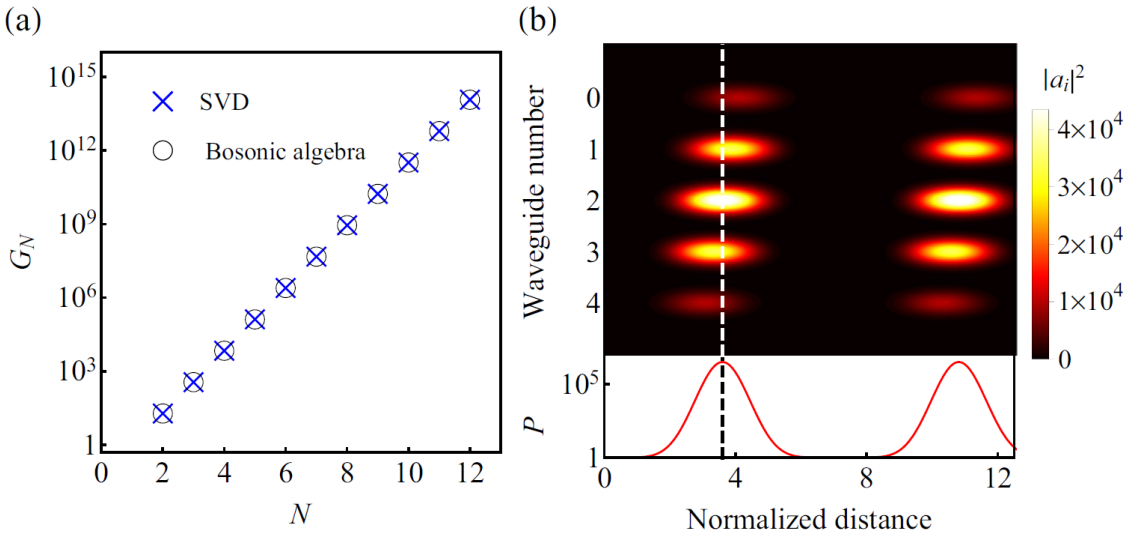

Figure 2.3: (a) A plot of G_N and G'_N against N when ($\tilde{g} = 0.9$) given by Eq. (2.9) on a log scale. Clearly the expression (2.9) for G_N provides the global value of the maximum amplification and it follows a power law dependence on N. (b) Propagation dynamics in a waveguide array implementing a 5th-order EP, i.e. described by H_5, under the optimal input excitation: $\boldsymbol{a}_I = \frac{1}{4}(1, -2i, -\sqrt{6}, 2i, 1)^{\mathrm{T}}$. The top panel presents the intensities in the individual waveguides while the lower panel plots the total intensity in normalized units. Note that the dynamics is oscillatory and that the maximum of the intensity in each waveguide does not necessarily occur at the same distance where the total intensity assume its maximum value.

Finally, we also study the propagation dynamics of the optimal initial condition for the case of H_5. Fig. 2.3(b) present the evolution of the power in the individual waveguides (top panel) as well as the total power (lower panel). An important observation here is that the propagation distance at which the total power attains its maximum value does not necessarily correspond to the maximum power in the individual channels.

2.4 Conclusions

In this chapter, we have investigated the behavior of PT symmetric systems having higher order exceptional points. Our analysis, relying on the bosonic algebra method, showed that for systems operating near exceptional points, the maximum possible amplification scales with the power of N (the order of the EP). These results have been confirmed by employing an exact numerical optimization techniques based on singular value decomposition. Given the recent success in implementing third order exceptional points in acoustic and photonic systems and the continuing effort to realize even more complex structures, our results provide a valuable insight into the generic behavior near EPs which may help direct future research in this field.

Chapter 3

Crossing exceptional points without phase transition

3.1 Introduction

Exceptional points (EPs) are peculiar singularities associated with multivalued complex function [14]. They also arise as special degeneracies in the spectra of parity-time-(PT-) symmetric (and in general non-Hermitian) Hamiltonians at which the eigenvalues and the corresponding eigenvectors become identical [5, 49], thus signaling a

The contents in this chapter were previously published in Scientific Reports 9 (1), 134 (2019). Refer Appendix A.2 for granted permission to be republished.

collapse of the eigenspace dimensionality, which in turn gives rise to a host of intriguing effects in the vicinity of these singularities [30, 31]. One particular characteristic feature that has been studied thoroughly in literature is phase transitions across EPs in PT-symmetric arrangements [65]. When the symmetry of the eigenvectors are studied as a function of one parameter of the PT Hamiltonian, one finds that on one side of the EP, the eigenvectors respect PT symmetry (i.e. they commute with the PT-symmetric operators) whereas on the other side of the EP, they violate the PT symmetry (in fact applying PT operator to one eigenvector yields another eigenvector). This phase transition between the PT phase and broken PT (BPT) phase, which is also known as PT spontaneous symmetry breaking, is accompanied by complex eigenvalue bifurcation. This behavior has been experimentally demonstrated in various physical platforms in optics [8, 9, 11, 12], electronics [22] and acoustics [66]. For more information, see refs.[1, 2].

In light of these intense theoretical and experimental activities, it is perhaps not surprising that EPs are always associated PT phase transitions. What is surprising though, is the lack of any rigorous mathematical proof for this statement. In this chapter, we show that this is not a coincidence, and that this widely accepted picture of PT phase transition is in fact incomplete.

Before we proceed, we briefly review the archetypal discrete PT-symmetric Hamiltonian, which was the subject of detailed investigation in several studies [7, 8, 9, 11, 12].

It consists of two coupled elements, having coupling coefficient κ and balanced gain/loss profile characterized by the non-Hermitian parameter γ. This Hamiltonian respects PT symmetry in the κ–γ plane. However, as γ is varied from $\gamma < \kappa$ to $\gamma > \kappa$, the associated eigenvectors undergoes a spontaneous symmetry breaking from the PT phase to the BPT phase [1, 2]. The transition point separating these two phases ($\gamma = \kappa$) is an EP. This behavior, which we call canonical PT phase transition, has been reported in more complex discrete and continuous systems. This in turn led to the common belief that crossing EPs along straight lines and PT phase transitions are inseparable notions.

In this chapter, we show that this is not the whole story and that this picture is indeed incomplete. To do so, we use the squaring operator to construct a simple Hamiltonian that violates the canonical PT phase transition in the following sense: as one parameter is varied continuously and monotonically along a straight line, the system crosses an EP without any PT symmetry breaking. As we will shortly see, this is an outcome of the non-trivial topological features incurred on the Riemann surface by the squaring operation. For more detailed discussion on how square and square root operations can give rise to altogether new topological structures, see ref.[67].

3.2 Results

3.2.1 Squaring Hamiltonian and its eigenvalues

To this end, consider the following family of PT Hamiltonians H_M (which can be generated by using the recursive bosonic algebra method [41]) whose matrix elements are given by:

$$H_M(n,l) = i2n\gamma\delta_{n,l} + \kappa g_{n+1}\delta_{n,l-1} + \kappa g_n \delta_{n,l+1}, \tag{3.1}$$

where γ and κ are the gain (or loss) and coupling coefficients, respectively and $g_n = \sqrt{(N+n)(N-n+1)}$; with $n, l = -N, -N+1, ..., N-1, N$ and $M = 2N$. Note that the value of N can be integer or half-integer.

The eigenvalues of H_M are given by $\mu_{M,m} = (M-2m)\sqrt{\kappa^2-\gamma^2}$ where $m = 0, 1, 2, ..., M$ [41]; and they feature higher order EPs [20, 39, 45, 68] at $\gamma = \kappa$ with a phase transition across this point from PT phase ($\gamma < \kappa$) to the BPT phase ($\gamma > \kappa$) [41, 69]. The crucial observation here is that the eigenvalues are pure real (imaginary) in the PT (BPT) phase. Let us now consider a new Hamiltonian $\mathcal{H}_M = H_M^2$. First we note that $\mathcal{H}_M$ respects PT symmetry since $PT\mathcal{H}_M(PT)^{-1} = PTH_M(PT)^{-1}PTH_M(PT)^{-1} = \mathcal{H}_M$. Furthermore, The eigenvalues of $\mathcal{H}$ are given by $\lambda = \mu^2$. The eigenspectrum of $\mathcal{H}_M$ is thus composed of

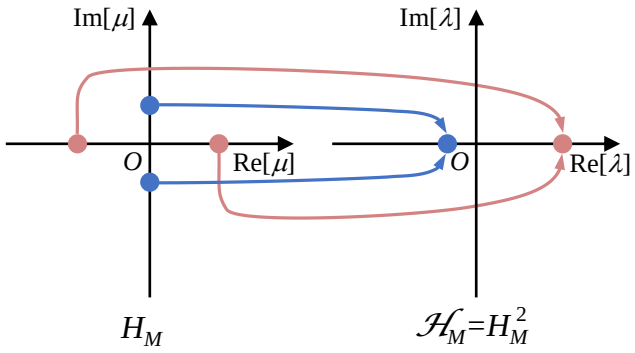

Figure 3.1: Illustration of the spectral properties of H_M and $\mathcal{H}_M = H_M^2$, as discussed in details in the text.

degenerate subspaces with positive real eigenvalues when $\gamma < \kappa$ and negative real eigenvalues when $\gamma > \kappa$. A schematic representation of how this degeneracy arise is shown in Fig. 3.1. Clearly, the spectrum of $\mathcal{H}_M$ does not undergo complex eigenvalue bifurcation as the parameter γ is swept across a straight line that passes through the point $\gamma = \kappa$.

3.2.2 Construct eigenstates respecting PT symmetry

Additionally, an important consequence of the two-fold degeneracy of the spectrum of $\mathcal{H}_M$ is that, it is always possible to construct PT symmetric eigenstates for any γ and κ which is not the case for H_M.

First of all, both Hamiltonians respect PT symmetry. Furthermore, the spectrum of H_M is in the PT or BPT phases when $\gamma < \kappa$ and $\gamma > \kappa$, respectively. Given that in

these two regimes, both H_M and $\mathcal{H}_M$ share the same eigenvectors, it may appear that $\mathcal{H}_M$ should also undergoes phase transition to the BPT as γ is increased beyond κ. As we have seen however, this is not the case and the eigenvalues of $\mathcal{H}_M$ remain real in all regimes. To reconcile these two observations, we recall that the spectrum of $\mathcal{H}_M$ consists of degenerate manifolds. Thus it is always to use superposition between any two degenerate two states to form a new bases that respect PT symmetry. For instance, consider two conjugate eigenstates of H_M, say $|\phi_{1,2}(\gamma)\rangle$ and having eigenvalues $\pm\mu$. For $\gamma < \kappa$, we will denote these eigenstates as $|\phi_{1,2}^{\mathrm{PT}}\rangle$ since they satisfy PT symmetry: $PT\,|\phi_{1,2}^{\mathrm{PT}}\rangle = |\phi_{1,2}^{\mathrm{PT}}\rangle$. On the other hand, when $\gamma > \kappa$, we will denote them by $|\phi_{1,2}^{\mathrm{BPT}}\rangle$ as they now break the PT symmetry: $PT\,|\phi_{1,2}^{\mathrm{BPT}}\rangle = |\phi_{2,1}^{\mathrm{BPT}}\rangle$. Note here that, without any loss of generality, we assumed a normalization of the eigenstates such that the action of the PT operator on them does not produce any scaling. When considering the phases of $\mathcal{H}_M$, both $|\phi_{1,2}(\gamma)\rangle$ are degenerate with an eigenvalue $\lambda = \mu^2$. Thus even when $\gamma > \kappa$, we can for new states $|\psi_\pm\rangle = e^{i(\pi/4\mp\pi/4)}(|\phi_1^{\mathrm{BPT}}\rangle \pm |\phi_2^{\mathrm{BPT}}\rangle)$. It is straightforward to verify that both $|\psi_\pm\rangle$ satisfy PT symmetry with $PT\,|\psi_\pm\rangle = |\psi_\pm\rangle$. We note that this behavior of $\mathcal{H}_M$ is a peculiarity of the particular model but is not a necessary condition for crossing an EP without phase transitions. Another peculiarity of $\mathcal{H}_M$ is the possibility additional exceptional vectors at the EP as compared with H_M. For example, while H_3 has only one exceptional vector, for $\mathcal{H}_3$ there are two independent exceptional vectors.

3.2.3 Confirmation of EP at $\gamma = \kappa$

It thus appears that the point $\gamma = \kappa$ is not associated with phase transition. Naturally, one would then ask if it is an EP. In order to check this and without in loss of generality, we consider the case where $M = 3$ (the Hamiltonian $\mathcal{H}_3$ has dimensions 4×4) and we set $\kappa = 1$. In general the Hamiltonian $\mathcal{H}_3$ has four different eigenstates forming two degenerate subspaces. Figure 3.2(a) depicts the Hermitian angle (Θ) between the two planes consisting of the degenerate eigenvectors (see Appendix at the end of this chapter for the definition of Hermitian angle between two planes). One indeed sees that at $\gamma = 1$, the two planes are identical ($\Theta = 0$), which indicates a collapse of the eigenspace dimensionality as would be expected at an EP. Interestingly however, at this point $\mathcal{H}_3$ exhibit two different eigenvectors whereas H_3 has only one.

Next, we also use the notion of pseudospectrum [70] to study the system sensitivity close to the point $\gamma = 1$ in order to confirm its EP character. The ϵ-pseudospectrum of a matrix A, denoted as $\sigma_\epsilon(A)$, is typically defined as:

$$\sigma_\epsilon(A) = \{\lambda' \in \mathbb{C} : \lambda' \in \sigma(A + E) : ||E|| \leq \epsilon\} \tag{3.2}$$

Here $\sigma(A)$ denotes the eigenvalue spectrum of A and $||...||$ is a matrix norm. Basically, it is a measure of how the eigenvalues of the original system vary in response for small

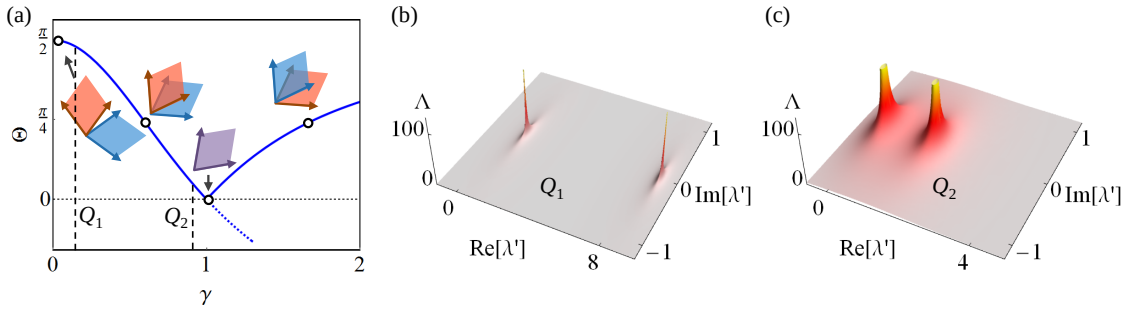

Figure 3.2: (a) The Hermitian angle Θ between the two planes spanned by the degenrate eigenvectors of that Hamiltonian $\mathcal{H}_3$ as a function of the non-Hermitian parameter γ. At the point $\gamma = 1$, the two planes are parallel, indicating a reduction of the eigenspace dimensionality. (b) and (c) depict the parameter $\Lambda = ||(\mathcal{H}_3 - \lambda' I)^{-1}||$ as a function of the complex parameter λ'. Close to the point $\gamma = 1$, the system exhibits sensitivity to perturbation as indicated by the large values of Λ over a wider area in the λ' plane (see SI for discussion on pseudospectrum). These results confirm that $\gamma = 1$ is indeed an EP of $\mathcal{H}_M$.

perturbations. Near EPs, these variations are very large. This definition was used in connection with non-Hermitian photonics [48]. Another equivalent, more practical definition is:

$$\sigma_\epsilon(A) = \{\lambda' \in \mathbb{C} : ||(A - \lambda' I)^{-1}|| \geq \frac{1}{\epsilon}\} \tag{3.3}$$

where I is the unitary matrix. In the main text we plot the quantity $\Lambda \equiv ||(\mathcal{H} - \lambda' I)^{-1}||$ as a function of the complex parameter λ'. Near EPs, we expect a spread for the high values of Λ over a large area in the λ' plane.

Figures 3.2(b) and (c) plot the values of $\Lambda = ||(\mathcal{H}_3 - \lambda' I)^{-1}||$ as a function of the parameter λ' for two different cases when $\gamma = 0.1$ (away from the EP) and $\gamma = 0.9$ (close to the EP). The spread of the high values of Λ in the λ' plane indicates the system sensitivity to perturbations. As can be inferred from the figure, this is indeed

the case in the vicinity of point $\gamma = 1$. Based on the above analysis, we indeed conclude that, as the Hamiltonian $\mathcal{H}_3$ is swept across the straight line passing through the point $\gamma = 1$, it crosses an EP without experiencing a phase transition. The above example thus presents a very interesting scenario that demonstrates the possibility of violating the canonical PT symmetry breaking.

3.2.4 Phase diagram of PT and BPT phase

In order to better understand these results within a general framework that encompass all the possible different situations, we invoke the notion of phase diagrams. In statistical mechanics and nonlinear dynamics, phase diagrams are used to classify the system's behavior into different phases as a function of some external parameters. In the context of our discussion of $\mathcal{H}_3$, one should in general study the classification of the eigenstates as a function of 32 different parameters (16 complex matrix entries). Fortunately, we can gain an insight into the behavior of $\mathcal{H}_3$ by considering a low dimensional projection of this higher dimensional parameter space. Here we do so by fixing κ and de-correlate some of the other parameters by allowing $\mathcal{H}_3(1,1)$ and $\mathcal{H}_3(4,4)$ to vary as a function of γ_1 while the rest of the matrix elements vary with γ_2. This choice provides a 2D projection of the phase diagram while at the same time guarantees that $\mathcal{H}_3$ still respect PT symmetry.

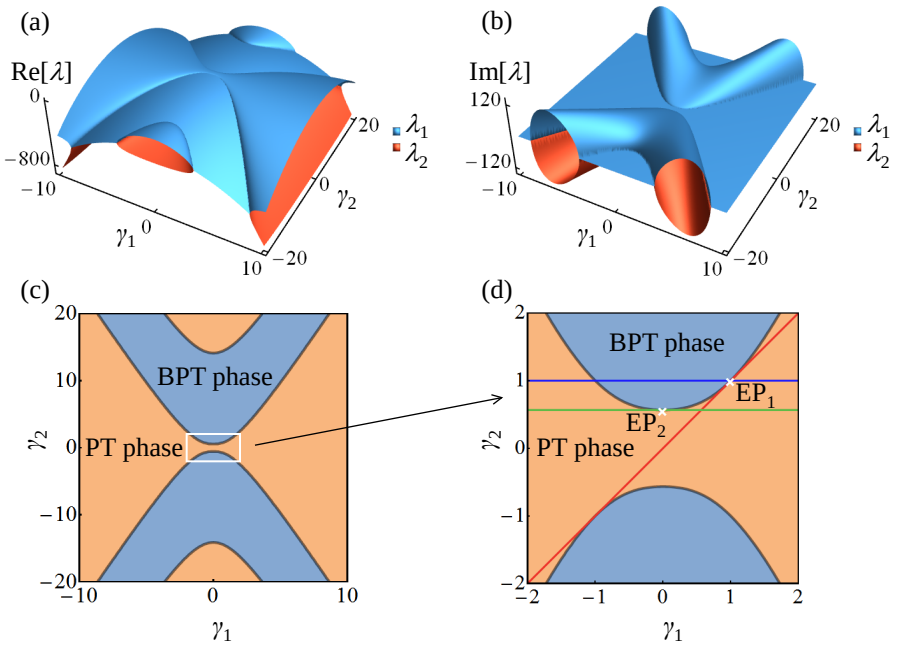

Figure 3.3: (a) and (b) Riemann surfaces for real and imaginary components of the spectrum of $\mathcal{H}_3$ are depicted as a function of the two parameters $\gamma_{1,2}$ (see text for details). (c) The phase diagram associated with (a) and (b). (d) Magnified view of the central part of (c). The red line represents the trajectory $\gamma_1 = \gamma_2$ corresponding to Fig. 3.2 (a) and crosses EP_1 without phase transition. Other trajectories such as that shown by the green line and cross EP_2 can also demonstrate similar behavior. On the other hand, the horizontal trajectory having $\gamma_2 = 1$ (blue line) is associated with phase transition.

Figure 3.3(a) and (b) depict the Riemann surfaces for the real and imaginary components of the eigenvalues of $\mathcal{H}_3$ in the γ_1–γ_2 plane, where one can identify the distinct PT phases. Figure 3.3(c) plots the phase diagram as extracted from Fig. 3.3(a) and Fig. 3.3(d) presents a more detailed blow up of the area surrounded by the rectangle in (c). Figure 3.3(d) clearly demonstrates the different phases are separated by curved lines of EPs. As one varies one or more of the system's parameter, the behavior can be very different depending on the trajectory taken in the parameter space. For example, no phase transition is observed if γ_1 is varied while $\gamma_2 = 0$.

On the other hand, fixing $\gamma_2 = 1$ and sweeping γ_1 from negative to positive values will lead to a PT-BPT phase transition followed by a BPT-PT transition (blue line). One can also fix $\gamma_2 = \sqrt{100 - 12\sqrt{69}} \approx 0.566$ to a value that guarantees that the line swept by varying γ_1 will just touch one EP without any phase transition (green line touching EP_2). The particular case we discussed earlier for $\mathcal{H}_3$ corresponds to the line $\gamma_1 = \gamma_2$ which also touches the boundary at one EP (red line crossing EP_1) without any phase transition. The concept of higher dimensional phase diagram thus provides a unified umbrella to treat all the rather special cases of phase transition, reverse phase transition, EP without phase transition, no EP and no phase transition as well as multiple phase transitions. This generalized perspective is very important to complex non-Hermitian systems and design next generation experiments.

As a side note, we emphasize that the exceptional lines separating the different phases in Fig. 3.3 curves in the parameter space, which are very different from previous studies that demonstrated exceptional lines in the Fourier space [16, 71].

3.3 Conclusions

In summary, we have revisited the concept of PT phase transition across EPs and demonstrated that, contrary to the common belief, crossing an EP along straight lines (the case of curved trajectories is rather trivial) in the parameter space can take

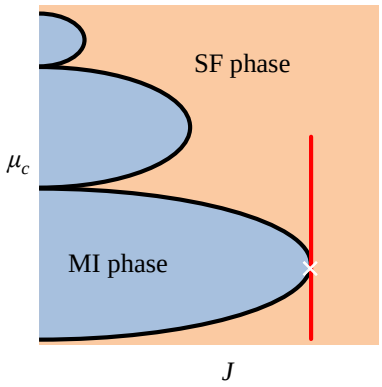

Figure 3.4: Generic phase diagram of the Bose-Hubbard model in a one dimensional lattice as a function of the hopping parameter J and the chemical potential μ_c. A trajectory along the red line can cross the critical point without any transition from the superfluid (SF) phase to the Mott insulator (MI) phase.

place without PT spontaneous symmetry breaking. We have explained these results by introducing the concept of PT phase diagram and its different projections in the parameter space that characterize a PT symmetric Hamiltonian.

Our results also raise interesting questions about the evolution along closed loops [72, 73, 74, 75, 76, 77, 78, 79] in these higher dimensional parameter spaces, which we plane to investigate elsewhere. Finally it is instructive to compare the behavior discovered here in this work with other systems studied in condensed matter physics. For example, by referring to the phase diagram of the quantum phase transition associated with the Bose-Hubbard Hamiltonian of interacting chain [80, 81, 82] (Fig. 3.4), we can see that it is possible to choose a trajectory that crosses the critical point on the boundary between the superfluid (SF) and Mott insulator (MI) phases from the SF side without having a phase transition.

Appendix 3A: Hermitian angle between eigenplanes

In Fig. 3.2(a), we plotted the Hermitian angle between two planes. Here we present the details of these calculations. Assume we have two planes defined by the vectors $v_{1,2}$ and $v_{3,4}$, respectively. One can then define the quantities $v_1 \wedge v_2$ and $v_3 \wedge v_4$ (called blades) and their inner product:

$$\langle v_1 \wedge v_2, v_3 \wedge v_4 \rangle = \begin{vmatrix} \langle v_1, v_3 \rangle & \langle v_1, v_4 \rangle \\ \langle v_2, v_3 \rangle & \langle v_2, v_4 \rangle \end{vmatrix}, \tag{3.4}$$

where $\langle , \rangle$ is the Hermitian inner product and $|...|$ is the determinant. Then the Hermitian angle Θ between these two planes is given by [83]:

$$\cos\Theta = \frac{|\langle v_1 \wedge v_2, v_3 \wedge v_4 \rangle|}{\sqrt{\langle v_1 \wedge v_2, v_1 \wedge v_2 \rangle \langle v_3 \wedge v_4, v_3 \wedge v_4 \rangle}}, \tag{3.5}$$

where $\Theta \in [0, \pi/2]$.

Chapter 4

Winding around Non-Hermitian Singularities

4.1 Introduction

Non-Hermitian singularities arise in multivalued complex functions[14, 84] as points where the Taylor series expansion fails. In the context of non-Hermitian Hamiltonians, these points, commonly referred to as exceptional points (EPs) feature special degeneracies where two or more eigenvalues along with their associated eigenfunctions become identical[29, 32]. An EP of order N (EPN) is formed by

The contents in this chapter were previously published in Nature Communications 9 (1), 4808 (2018). Refer Appendix A.3 for granted permission to be republished.

N coalescing eigenstates. Recently, the exotic features of EPs have been subject of intense studies[7, 8, 15, 16] with various potential applications in laser science[12, 13, 17, 18], optical sensing[19, 20, 21], photon transport engineering[22, 23] and nonlinear optics[24, 25] just to mention few examples. For recent reviews, see refs. [1, 2].

Very often, EPs are points of measure zero in the eigenspectra of non-Hermitian Hamiltonians which makes them very difficult to access, even with careful engineering. Yet, their effect can be still felt globally. Particularly, an intriguing aspect of non-Hermitian systems is the eigenstate exchange along loops that trace closed trajectories around EPs. In this regard, stroboscopic encircling of EP2 (EP of order 2) has been studied theoretically[85, 86] and demonstrated experimentally in various platforms such as microwave resonators[72, 73] and exciton-polariton setups[74]. Additionally, Berry's phase around EPs has been also theoretically investigated in details[87, 88, 89, 90]. Complementary to these efforts, the dynamic encircling of EPs was shown to violate the standard adiabatic approximation[75, 76, 77, 91]. These predictions were recently confirmed experimentally by using microwave waveguides platforms[78] and optomechanical systems[79].

Notably, the aforementioned studies focused only on systems having only one EP of order two. Richer scenarios involving multiple and/or higher order EPs have been

largely neglected, with rare exceptions that treated special systems (admitting simple analytical solutions) on a case by case basis[40, 92]. This gap in the literature is probably due to the complexity of the general problem and its perceived experimental irrelevance. However, recent progress in experimental activities that explore the physics of non-Hermitian systems are quickly changing the research landscape, and controlled experiments that probe more complicated structures with multiple EPs will be soon within reach. These developments beg for a general approach that can provide a deeper theoretical insight into these complex systems.

In this chapter, we bridge this gap by introducing a general formalism for treating the eigenstate exchange along arbitrary loops enclosing multiple EPs. More specifically, our approach utilizes the power of group theory together with group representations to decompose the final action of any loop into more elementary exchange processes across the relevant branch cuts (BCs). This formalism simplifies the analysis significantly, which in turn allows us to gain an insight into the problem at hand and unravel a number of intriguing results: Trajectories that encircle the same EPs starting from the same initial point and having the same direction do not necessarily lead to an identical exchange between the eigenstates; Establishing such equivalence between the loops (i.e. same eigenstate exchange) is guaranteed only by invoking the topological notion of homotopy. As a bonus, our approach can also paint a qualitative picture of the dynamical properties of the system.

4.2 Results

4.2.1 General formalism for encircling multiple EPs.

Before we start our analysis, we first describe the simple case of EP2. These are special points associated with the multivalued square root function in the complex plane. The Riemann surface of this function is shown in Fig. 4.1(a). Clearly, as two parameters are varied in the complex plane to trace a closed loop, the initial point on the surface ends up on a different sheet. This process can be also viewed by considering the projection on the complex plane after adding a BC. As we mentioned before, this simple scenario has been studied in the literature in both the stroboscopic and dynamical cases. Consider however what happens in more complex situations where there are more than one EP. For instance, Fig. 4.1b depicts a case with three EPs. One can immediately see that this scenario exhibits an additional complexity that is absent from the previous case. Namely, there are now different ways for encircling the same EPs (as shown by the solid and dashed loops in the figure). This in turn raises the question as whether these loops lead to the same results or not. These are the type of questions that we would like to address in this work. As we will see, in resolving these questions, our analysis also reveals several peculiar scenarios.

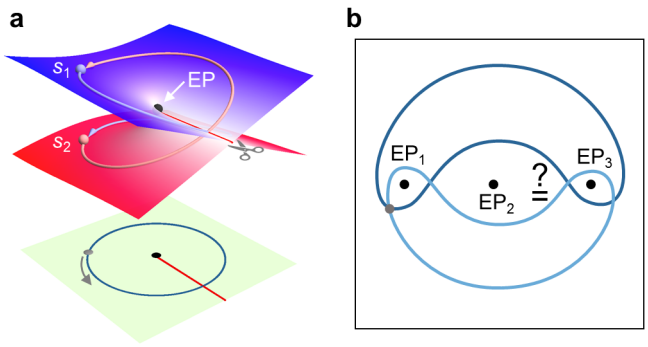

Figure 4.1: Different ways of encircling multiple expectational points (EPs). (a) Illustration of Riemann surface associated with the square root function associated with an archetypal 2×2 non-Hermitian Hamiltonian. A loop that encircles the EP starting from the state s_1 will map it onto s_2 and vice versa. In the complex plane projection, this is represented by adding a branch cut as shown by the red line. The gray arrow in the projection plane indicates the encircling direction. (b) A scenario that exhibits three EPs. In this case, loops can encircle the same EPs in different ways as illustrated by the two loops (solid/dashed lines) that enclose EP$_{1,3}$ starting from the same point (gray dot).

To this end, let consider an n-dimensional non-Hermitian discrete Hamilton. The Riemann surface associated with the real (or imaginary) part of its eigenvalues will consist of n sheets corresponding to different solution branches. We will label these n branches as b_1, b_2, ..., b_n. In the complex plane, these branches are separated by BCs. Thus, an initial point on any trajectory in the complex plane will correspond to n initial eigenstates, which we will label as s_1, s_2, ..., s_n. The eigenvalue for each state s_i will be denoted by λ_i. As the encircling parameters are varied, the eigenstates will move along the trajectory, crossing from one branch to another across the BCs. The crucial point here is that, we will always fix the initial subscript of the state as it

changes. We now describe the initial configuration on the trajectory by the mapping:

$$\mathcal{C}_0 = \begin{bmatrix} \tilde{s}_0 \\ \tilde{b}_0 \end{bmatrix}, \tag{4.1}$$

where $\tilde{s}_0 = (s_1, s_2, ..., s_n)$ and $\tilde{b}_0 = (b_1, b_2, ..., b_n)$ are two ordered sets. In our notation, $\mathcal{C}_0$ maps (or associates) every element of $\tilde{s}_0$ to the corresponding element in $\tilde{b}_0$. Note that we can change the orders of the elements in both $\tilde{s}_0$ and $\tilde{b}_0$ identically without changing $\mathcal{C}_0$. In other words, we have several different ways for the same configuration. As the loop crosses BCs, the exchange between the eigenstates will result in new configurations which, again, can be described in different ways. Two particular choices are interesting here. In the first one, we always fix $\tilde{s}_0$ and allow the elements of $\tilde{b}_0$ to shuffle, effectively creating a new $\tilde{b}$. In the second, we just do the converse. We will call these two equivalent notations the s- and b-frames, respectively. This is explained by the cartoon picture in Fig. 4.2(a).

The first step in our analysis is to choose a scheme for sorting the eigenstates and locating the BCs accordingly. We will discuss the details of the sorting later but for now we assume that we have a certain number of BCs and we label each one with a unique integer value (positive for a crossing in certain direction and negative for reverse crossing). Next we determine how the eigenstates are redistributed across an infinitesimal trajectory across each BC (see discussion later on sorting schemes). For every loop, we then create an ordered list σ that contains the number of the crossed

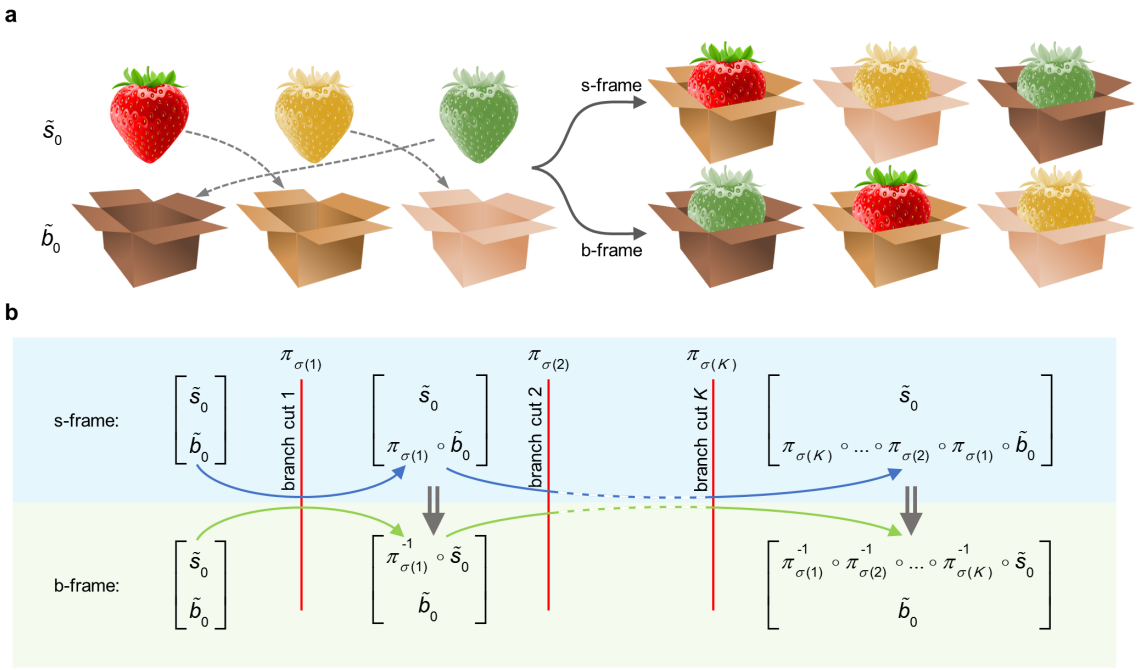

Figure 4.2: Different permutation frames. (a) A simple illustration of the two different frames used for representing the same configuration. (b) A summary of the mathematical formulation of the concept depicted in (a) (see main text for more details).

BCs in the order they are crossed by the loop. In other words, the element $\sigma(j)$ is the number of the j-th crossed BC. Clearly the set σ will be in general different from loop to another and even can be different for the same loop depending on the initial point or the encircling direction. Then the final configuration in both the s- and b-frames is given by:

$$\mathcal{C}^{\mathrm{s}}_{\sigma} = \begin{bmatrix} \tilde{s}_0 \\ \tilde{b}_\sigma \end{bmatrix} \equiv \begin{bmatrix} \tilde{s}_0 \\ \mathcal{P}[\prod \pi_{\sigma(j)}] \circ \tilde{b}_0 \end{bmatrix}, \tag{4.2}$$

$$\mathcal{C}^{\mathrm{b}}_{\sigma} = \begin{bmatrix} \tilde{s}_\sigma \\ \tilde{b}_0 \end{bmatrix} \equiv \begin{bmatrix} \{\mathcal{P}[\prod \pi_{\sigma(j)}]\}^{-1} \circ \tilde{s}_0 \\ \tilde{b}_0 \end{bmatrix}, \tag{4.3}$$

where $\mathcal{P}$ denotes the ordering operator which arranges the multiplication of the permutation operators $\pi_{\sigma(j)}$ from right to left according to the order of crossing the BCs; and the product runs across the index j. For example, if $\sigma = (3, 1, 2)$, then the $\mathcal{P}[\prod \pi_{\sigma(j)}] = \pi_{\sigma(3)} \circ \pi_{\sigma(2)} \circ \pi_{\sigma(1)} = \pi_2 \circ \pi_1 \circ \pi_3$. The permutation operator π_k associated with BC k is the standard permutation mapping that, which when applied to a set will shuffles the order of its elements [93]. Here it is used to describe how the eigenstates are redistributed when a trajectory crosses a BC. For instance, if the permutation exchange the order of the first two elements of $\tilde{b}_0$ across a BC k, then $\pi_k(b_{1,2}) = b_{2,1}$, and $\pi_k(b_i) = b_i$ for $i > 2$. Figure 4.2(b) illustrates the relation between the s- and b-frames calculations as expressed by Eqs. (4.2) and (4.3) .

The above discussion can be directly mapped into linear algebra by using representation theory. To do so, we define the vectors $\boldsymbol{s}_0 = (s_1, s_2, ..., s_n)^\mathsf{T}$ and $\boldsymbol{b}_0 = (b_1, b_2, ..., b_n)^\mathsf{T}$. In the s-frame, we will fix $\boldsymbol{s}_0$ and allow $\boldsymbol{b}$ to vary in order to represent the change in configuration. In the b-frame, we just do the opposite. For instance, if after crossing a BC, eigenstate 1 moves to branch n, eigenstate 2 moves to branch 1 and eigenstate n moves to branch 2, this will be expressed as $\boldsymbol{b}_1 = (b_n, b_1, ..., b_2)^\mathsf{T}$ in the s-frame; and $\boldsymbol{s}_1 = (s_2, s_n, ..., s_1)^\mathsf{T}$ in the b-frame. After a loop completes its full cycle, the final vector is then compared with the initial one to determine the exchange relations between the eigenstates. For instance, if the above vector was the final result, the exchange relations will be: $\{s_1, s_2, ..., s_n\} \to \{s_n, s_1, ..., s_2\}$, which means that after the evolution s_1 became s_n, s_2 became s_1 and s_n became s_2.

We can now express the action of the permutation operators π_k by the matrices P_{π_k} whose elements are obtained according to the rule $P_{\pi_k}(m,l) = 1$ if $b_l = \pi_k(b_m)$, and 0 otherwise[94]. In the s- and b-frames, the redistribution of the eigenstates across the branches in Eqs. (4.2) and (4.3) can be then described by:

$$\boldsymbol{b}_\sigma = \{\mathcal{P}[\prod M_{\sigma(j)}]\}^{-1}\boldsymbol{b}_0, \tag{4.4}$$

$$\boldsymbol{s}_\sigma = \mathcal{P}[\prod M_{\sigma(j)}]\boldsymbol{s}_0, \tag{4.5}$$

where $M_k = P_{\pi_k}^{-1}$. In arriving at the above equation, we have used standard results from group theory: $P_{\pi_2 \circ \pi_1} = P_{\pi_1} P_{\pi_2}$ and $P_{\pi^{-1}} = P_\pi^{-1}$.

In the rest of this manuscript, we adopted the b-frame with matrices M. This approach offers a clear advantage: the order of the matrices acting on the state vectors $\boldsymbol{s}$ is consistent with the order of crossing the BCs. As we will see shortly, this will allow us to develop the topological features of the equivalent loops in a straightforward manner. Finally, we note that if crossing a BC from one direction to another is associated with a matrix M, the reverse crossing will be described by M^{-1}. In some cases (such as with EP2), we can have $M^{-1} = M$ but this is not the general case.

Our discussion so far focused on developing the general formalism by assuming that the eigenstates of the system are somehow classified according to a certain criterion. This is equivalent to say that we divide the associated Riemann surface into different

sheets, each harboring a solution branch. Of course, one can pick any such criterion to classify the solutions. In previous studies that involved one EP of order two or three, the eigenstates were classified based on the analytical solution of the associated characteristic polynomial. This however has two drawbacks: It generates relatively complex branches on the Riemann sheet; and it cannot be applied for discrete Hamiltonians having dimensions larger than four since analytical solutions do not exist for polynomials of order five or larger. Thus our analysis above is useful only if one can find a sorting scheme that circumvents the above problems. Interestingly, such a sorting scheme is easy to find. Particularly, we can sort the eigenstates based on the ascending (or descending) order of the real or imaginary parts of their eigenvalues. This scheme can be easily applied to any system of arbitrarily high dimensions. Moreover, it lends itself to straightforward numerical implementations. To compute the permutation operator π_k and its associated matrix M_k across a BC k, one chooses an infinitesimal trajectory that crosses the BC and calculates how the eigenvalues evolve along this trajectory, comparing their order before and after crossing the BC. That will immediately provide information about the permutations. We illustrate this using a concrete example later.

4.2.2 Equivalent loops and homotopy

Here we employ the predictive power of our formalism to address the following question: are there any global features that characterize the equivalence between different loops in the parameter space regardless of their geometric details? In answering this question, we will first focus on the stroboscopic case and later discuss the implication for the dynamical behavior.

Here, two loops are called equivalent if they lead to identical static eigenstates exchange. It is generally believed that two similar loops in the parameter space starting at the same point and encircling the same EPs in the same direction are equivalent. Surprisingly, we will show below that this common belief is wrong.

In general two loops will be equivalent if they have the same matrix product in Eq. (4.5). This can occur for two unrelated loops which we will call accidental equivalence. However, we are particularly interested in establishing the conditions that guarantee this equivalence. To do so, we invoke the notion of homotopy between loops. In topology, two simple paths (a simple path is a one that does not intersect itself), having the same fixed endpoints in a space S, are called homotopic if they can be continuously deformed into each other[95]. If the two endpoints of a path are identical, this path is a loop with the identical endpoint as a basepoint. The space S here will

be a two-dimensional (2D) punctured parameter space after removing all EPs. Based on these definitions, we can now state the main results of this section: Homotopy is a sufficient condition for equivalence between loops; Loops that are connected by free homotopy (continuous deformation between loops without any fixed points) can be equivalent for some starting points and inequivalent for others.

In order to validate this statement, we consider a generic Hamiltonian having a number of EPs and, without any loss of generality, we focus only on a subset of the spectrum as shown in Fig. 4.3. The axes on the figures represent any two parameters of the Hamiltonian. We define the space S to be the two-dimensional parameter space excluding the EPs. Figure 4.3(a) depicts a loop ⓐ that encircles two EPs starting from point z in the counterclockwise (CCW) direction. Consequently, its final permutation matrix is given by $M_p M_o$. Consider now what happens when loop ⓐ is deformed continuously to a new loop. Apart from the trivial case where the deformation does not change the number or the order of BC crossing, different interesting scenarios can arise as illustrated in Fig. 4.3(b)–(e). Particularly, in Fig. 4.3(b), the deformation can take place only by crossing additional EP, where it is clear that the new matrix product of loop ⓑ ($M_p M_r M_o M_r^{-1}$) is in general different than the initial one. In this case, the two loops are not necessarily equivalent (unless accidental equivalence takes place). In the case illustrated in Fig. 4.3(c), the deformation can change the number of the crossed BCs in pairs traversed consecutively back and forth but without crossing any EP. Here the two loops ⓐ and ⓒ are also equivalent

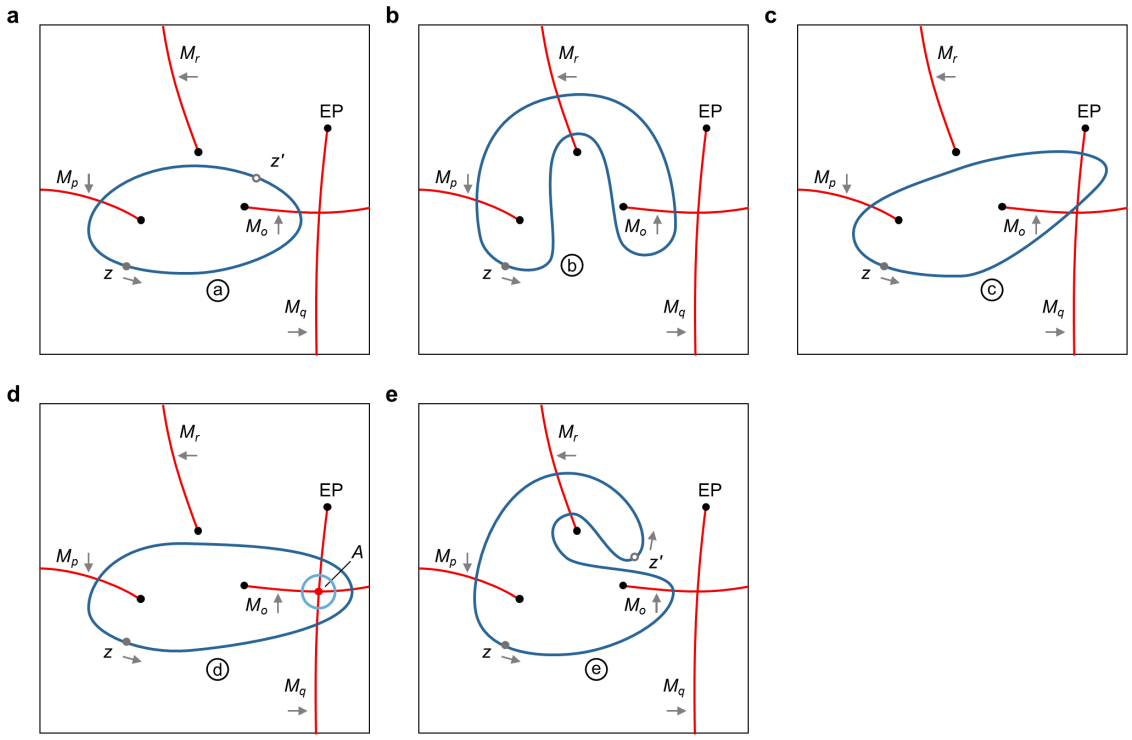

Figure 4.3: Homotopy between loops. Illustration of equivalence between homotopic loops in the parameter space of a generic Hamiltonian. (a) Loop ⓐ encloses two exceptional points (EPs) associated with matrices M_o and M_p. (b) Loop ⓑ encloses the same two EPs yet it cannot be deformed into loop ⓐ without crossing EP associated with M_r. Consequently it has a different matrix product (assuming not accidental equivalence). On the other hand, loops ⓒ and ⓓ in (c) and (d) can be deformed into ⓐ without crossing any EP. As a result, they are equivalent (have the same matrix product) as shown in the text. (e) A peculiar case of free homotopy is presented. Loop ⓔ is homotopic with ⓐ for the starting point z but not for z'. As a result, the two loops are equivalent for the former point but not for the latter. The discussion here is very generic and can be extended easily to any other configuration of EPs and branch cuts (BCs). As a side note, we emphasize that the choice of the BCs is not unique. However, while different partitioning will lead to a new set of matrices, the final results and the topological relations between the loops are invariant. Black dots represent EPs, red lines are the BCs and the blue loops are the encircling trajectories.

because the matrix product is still the same: $M_p M_q^{-1} M_q M_o = M_p M_o$. Alternatively, the deformation shown in Fig. 4.3(d) changes the number of the crossed BCs in pairs

traversed back and forth but not consecutively. In this case, the final matrix product is given by $M_p M_q^{-1} M_o M_q$. It is not immediately clear if this product is equivalent to $M_p M_o$. However, since the intersection point of the BCs (point A in Fig. 4.3(d)) is not an EP, then by definition, encircling point A with a loop that does not enclose any EP must give the identity operator. In terms of matrices, this translates into $M_o M_q M_o^{-1} M_q^{-1} = I$, or $[M_o, M_q] = 0$, where I is the identity matrix. Consequently, $M_p M_q^{-1} M_o M_q = M_p M_q^{-1} M_q M_o = M_p M_o$, i.e. loops ⓓ and ⓐ are equivalent.

Finally we can also have a loop similar to ⓔ as shown in Fig. 4.3(e). This probably the most intriguing situation. For a starting point at z, both loops ⓐ and ⓔ have the same matrix product $M_p M_o$ which is consistent with the fact that they can be deformed into one another without crossing any EP. On the other hand, for a different starting point such as z', the matrix product of loop ⓔ is given by $M_r^{-1} M_o M_p M_r$, i.e. different than that of loop ⓐ, which is given by $M_o M_p$. Note that for this starting point, the two loops cannot be deformed into each other without crossing any EP. In topology, a continuous deformation that does not involve fixed points is called free homotopy. Here loops ⓐ and ⓔ are connected by free homotopy, i.e. they are in general equivalent only for a subset of all the possible starting points. This completes our argument.

The above discussion focused only on the stroboscopic case. However, as we will show in the explicit example presented in the next section, homotopy is also relevant to

the dynamical encircling of EPs. Particularly, our numerical calculations show that homotopic loops can have the same outcome, despite the failure of the adiabatic perturbation theory. These results can be better understood by considering the evolution of the loops on the full three-dimensional (3D) Riemann surface as we further discuss later.

4.2.3 Illustrative examples

We now discuss a concrete numerical example to demonstrate the application of our formalism and confirm the various predictions of the previous discussion. We emphasize that the example considered below is not a special case. It was merely chosen because it is complex enough to exhibit the exotic effects before, yet not too complex to impede physical implementations.

Consider the following Hamiltonian:

$$H = \begin{bmatrix} i\gamma & J & 0 & 0 \\ J & 0 & \kappa & 0 \\ 0 & \kappa & 0 & J \\ 0 & 0 & J & -i\gamma \end{bmatrix}, \tag{4.6}$$

where i is the imaginary unit, κ & J are coupling coefficients and γ is the non-Hermitian parameter. In what follows, the four eigenvalues of H will be investigated

as a function of the complex κ by fixing $J = \gamma = 1$ (in certain physical platforms such as optics, it might be practically easier to fix all the parameters and change γ, but that will not affect the main conclusions of this work).

Under these conditions, H has three pairs of EPs at $\kappa = \pm 1$, $\pm\sqrt{2\sqrt{3}-3}$, $\pm i\sqrt{2\sqrt{3}+3}$, which we will denote by EP_1, EP'_1, EP_2, EP'_2, EP_3, EP'_3, respectively. In each group, $\mathrm{EP}'_{1,2,3}$ has same properties as $\mathrm{EP}_{1,2,3}$. The Riemann surface and the distribution of the EPs in the complex κ plane are shown in Fig. 4.4a and b, respectively.

As discussed previously, the first step in our approach is to identify a simple sorting method. Here we chose to sort the eigenvalues according to the magnitude of their real parts as shown in Fig. 4.4(a) where every branch is distinguished by a distinct color. From this figure, we can also identify the features of the EPs as follows: EP_1 & EP'_1 are of second order and connect branches 2 and 3; EP_2 & EP'_2 are of second order and connect branches 1 and 2 on one hand, and branches 3 and 4 on the other; and finally EP_3 & EP'_3 are of second order and connect branches 1 and 3 as well as branches 2 and 4 (In fact all the four surfaces of $\mathrm{Re}[\lambda]$ are connected at EP_3 & EP'_3 and one has to look at the $\mathrm{Im}[\lambda]$ surface to infer the connectivity). Equivalently, the surface connectivity across the EPs can be characterized by using a two-dimensional plane spanned by the real and imaginary parts of κ along with the BC lines that separate the different solution branches and the information on

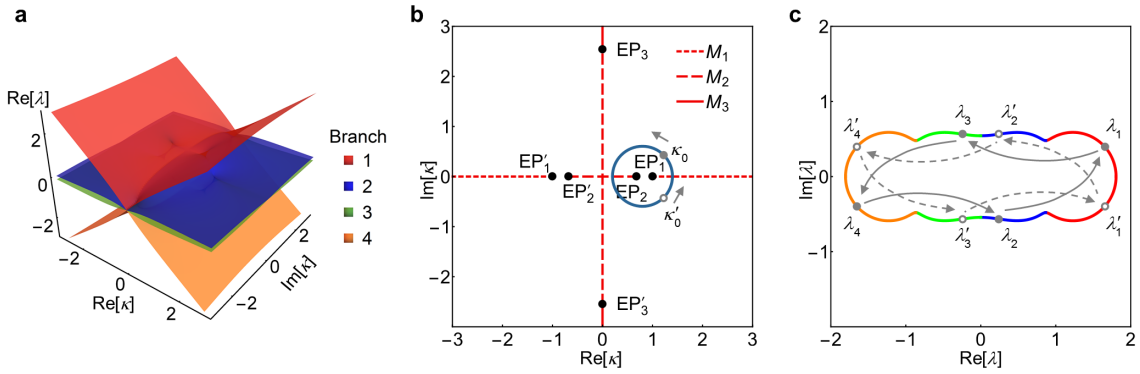

Figure 4.4: Numerical illustration of our approach. (a) The branches of Riemann surface of the real part of eigenvalues of H in Eq. (6.3) are distinguished by different colors according to the magnitude of Re[λ]. (b) The exceptional points (EPs) (black dots) and their corresponding branch cuts (BCs) (red lines) are illustrated. Each BC is related with a permutation matrix $M_{1,2,3}$ in Eq. (4.7). One closed loop (blue line) encircles EP_1 and EP_2 counterclockwise (CCW), starting from κ_0 or κ_0' (the solid or hollow gray points) on the loop. Loops intersecting with BCs would lead to eigenvalues moving from one branch to another, and result in the swap of eigenstates finally. (c) The stroboscopic evolution of complex eigenvalues are plotted as a parametric function of κ when it moves along the loop CCW. The eigenvalues at the starting point are labeled as gray points (solid or hollow) on their trajectory. The colors in the eigenvalue trajectory represent which branch the eigenvalues are located at instantaneously. The joints of two colors are where the κ crosses the BCs. The gray points (solid or hollow) and arrows illustrate the evolution of eigenvalues for starting from κ_0 or κ_0', and therefore the evolution of eigenstates is $\{s_1, s_2, s_3, s_4\} \to \{s_3, s_1, s_4, s_2\}$ and $\to \{s_2, s_4, s_1, s_3\}$, respectively.

the transition between the different branches across each line. The latter can be expressed in terms of permutation matrices. Our sorting scheme of the eigenvalues of H results in six BCs as shown in Fig. 4.4(b), but one can identify only three different permutation matrices:

$$M_1 = \begin{bmatrix} 1 & 0 & 0 & 0 \\ 0 & 0 & 1 & 0 \\ 0 & 1 & 0 & 0 \\ 0 & 0 & 0 & 1 \end{bmatrix}, \quad M_2 = \begin{bmatrix} 0 & 1 & 0 & 0 \\ 1 & 0 & 0 & 0 \\ 0 & 0 & 0 & 1 \\ 0 & 0 & 1 & 0 \end{bmatrix}, \quad M_3 = \begin{bmatrix} 0 & 0 & 0 & 1 \\ 0 & 0 & 1 & 0 \\ 0 & 1 & 0 & 0 \\ 1 & 0 & 0 & 0 \end{bmatrix}. \tag{4.7}$$

The correspondence between these matrices and the BCs is depicted in Fig. 4.4b. It is not difficult to see that the above matrices have the following properties: $M_1^2 = M_2^2 = M_3^2 = I$, and $[M_1, M_3] = [M_2, M_3] = 0$.

We now focus on the stroboscopic encircling of EPs. As illustrative example, we consider the loop encircling both EP_1 and EP_2, as shown in Fig. 4.4(b). Clearly, the final exchange relation is determined by the product of M_1 and M_2. Since $[M_1, M_2] \neq 0$, one has to be more specific about the starting point and direction. For sake of illustration, let us choose CCW direction, and κ_0 or κ_0' as the starting point. In the first case, the loop intersects the BC associated with M_2 first before it crosses that of M_1. As such, we have $M_1 M_2 (s_1, s_2, s_3, s_4)^{\mathsf{T}} = (s_2, s_4, s_1, s_3)^{\mathsf{T}}$, which in turn implies the exchange $\{s_1, s_2, s_3, s_4\} \to \{s_3, s_1, s_4, s_2\}$. Similarly, the starting point κ_0' will give $M_2 M_1 (s_1, s_2, s_3, s_4)^{\mathsf{T}} = (s_3, s_1, s_4, s_2)^{\mathsf{T}}$ which leads to $\{s_1, s_2, s_3, s_4\} \to \{s_2, s_4, s_1, s_3\}$. These exchange relations are also evident from the eigenvalues trajectories in Fig. 4.4(c). Another important consequence for the absence of commutation between M_1 and M_2 is that $M_2 M_1 M_2 M_1 \neq I$. Hence encircling the loop in Fig. 4.4(b) twice still lead to nontrivial exchange. For example, the state s_1 will evolve into s_3, s_4 and s_2 after encircling the loop one, two, and three times, respectively. We have also confirmed (not shown here) that our formalism can produce the results for the 3×3 Hamiltonians, where encircling two EPs of order two can equivalent to encircling a third order EP[40, 92, 96].

We further elucidate on the topological features of equivalent loops in the context of the example given by Eq. (6.3). In this case, the space S would be the space spanned by $\mathrm{Re}[\kappa]$ and $\mathrm{Im}[\kappa]$ after removing the points $\mathrm{EP}_{1,2,3}$ and $\mathrm{EP}'_{1,2,3}$. By inspecting the two loops ① and ② in Fig. 4.5(a), it is clear that they are not homotopic for the starting point κ_0. Indeed the net permutation matrix associated with loop ① is $M_1M_2M_1M_2$, resulting in $\{s_1, s_2, s_3, s_4\} \to \{s_4, s_3, s_2, s_1\}$. However, the permutation matrix associated with loop ② is $M_1M_3M_1M_3 = I$. Consequently their exchange relations are in general different as shown in Fig. 4.5(b) and (c).

Next, we investigate a scenario that highlights the case of free homotopy. The two loops ③ and ④ in Fig. 4.5(d) are similar (enclose the same EPs), yet they are not homotopic for the starting point κ_0, i.e. they cannot be transformed into one another while keeping the starting point fixed and without crossing EP_2. Thus the two loops are not necessarily equivalent. Indeed the net redistribution matrix associated with loop ③ is M_1, resulting in $\{s_1, s_2, s_3, s_4\} \to \{s_1, s_3, s_2, s_4\}$; while for loop ④, the permutation matrix is $M_2M_1M_2$, which gives $\{s_1, s_2, s_3, s_4\} \to \{s_4, s_2, s_3, s_1\}$. On the other hand, if we consider the same loops ③ and ④ but with a different starting point κ'_0, they are homotopic and the net permutation matrix is M_1 for both loops. Figure 4.5(e) and (f) confirms these results.

So far we have discussed the stroboscopic (or static) exchange between the eigenstates

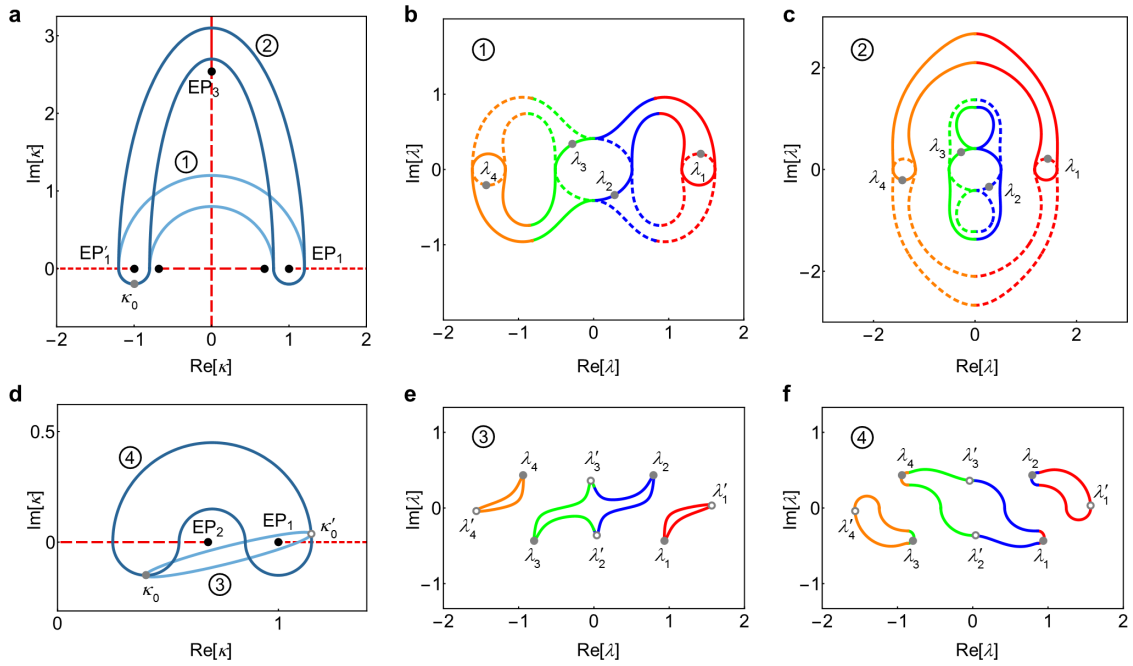

Figure 4.5: Numerical example of homotopic relations between loops. (a) Two similar loops ① and ② encircle the exceptional points EP_1 and EP'_1. The two loops are non-homotopic for any starting point including κ_0 (gray point) (which is considered for the example), since they cannot be deformed into one another without crossing EP_3. Their corresponding matrix product is $M_1M_2M_1M_2$ and I, respectively. This is confirmed by their eigenvalue trajectories as shown in (b) and (c). (d)The two similar loops ③ and ④ are non-homotopic for the starting point κ_0 but homotopic for κ'_0. This is also reflected in the exchange relations of the eigenvalues as shown in (e) and (f). Black dots represent EPs, red lines are the BCs and the blue loops are the encircling trajectories.

as a result of encircling EPs. Whereas this type of evolution can be in general accessed experimentally (see refs. [72, 73, 74] for the case of second order EPs), recent theoretical and experimental efforts are painting a different picture for the dynamic evolution, showing that the interplay between gain and loss will inevitably break adiabaticity[75, 76, 77, 78, 79, 91]. It will be thus interesting to investigate whether the homotopy between the loops (or its lack for that matter) has any impact on the

dynamic evolution. Here we do not attempt to answer this question rigorously but will rather consider illustrative examples. To do so, we focus again on the loops ③ and ④ shown in Fig. 4.5(d), and we perform a numerical integration to compute the dynamical evolution around these loops starting from either κ_0 or κ_0'. As we discussed before, the loops are similar for both initial conditions but homotopic only for the later one. The computational details are presented in Appendix 4A but the main results confirm our conclusion. When the two loops are homotopic (i.e when the initial point on the loop is κ_0') any initial state s_i, with $i = 1, 2, 3, 4$, will end up at state s_2 regardless of the considered loop. For similar but non-homotopic loops (i.e when the initial point on the the loop is κ_0), the initial states on loop ③ always evolve to s_3 while those on loop ④ will evolve to s_1. These results suggest that homotopy between the loops plays a much greater role than just describing the static exchange between the states.

Finally, in order to gain more insight into the topological equivalence (or nonequivalence) between loops that encircle the same EPs and how they affect the dynamic evolution, we plot the Riemann surface that corresponds to Fig. 4.5(d) together with the stroboscopic loops ③ and ④ in Fig. 4.6. As we have seen before, these two loops encircle the same EP starting from κ_0 yet they are not equivalent. This feature becomes more transparent when we consider the full 3D Riemann surface with its four sheets. Particularly, we see that the exceptional point EP_2 unfolds into two different

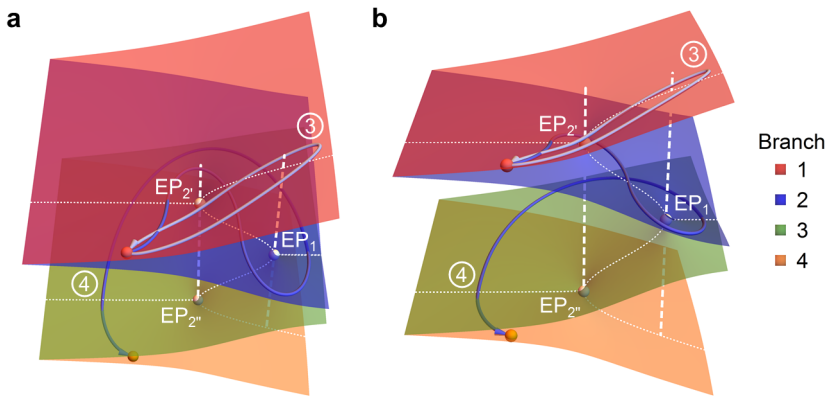

Figure 4.6: Riemann surface and homotopy between loops. Two different perspectives for the four-sheets Riemann surface (associated with the real parts of the eigenvalues) that corresponds to Fig. 4.5(d) are depicted in (a) and (b). The two loops ③ and ④ (blue lines) that encircle EP_1 (white point) in the two-dimensional (2D) parameter space are also shown. As explained in the text, the homotopy test (performed parameter space) for these two loops shows that they are not equivalent, which results in different stroboscopic and dynamic features. On the Riemann surface, this property becomes even more evident by noting that the two loops span different sheets. The red point stands for eigenvalue λ_1 (corresponding to eigenstate s_1) at the initial parameter point. This state will evolve to itself or to the orange point along loop ③ and ④, respectively. The dashed white lines are vertical lines emanating from the exceptional points (EPs) to illustrate the fact that the projections of the two loops considered here encircle EP_1 but not EP_2. The white dotted lines illustrate the eigenvalue bifurcation across the EPs on the Riemann surface.

points $EP_{2'}$ and $EP_{2''}$ connecting different sheets. As a result, two trajectories starting from the same point can evolve on different manifolds in 3D space despite the fact that their projection in the 2D parameter space will always encircle the same EP. This in turn explains the difference in the dynamic evolution associated with the two loops. From a practical perspective, these results are very important in the following sense. Recently, the chirality of dynamic encircling of EPs was demonstrated experimentally and studied theoretically. It was shown that the dynamic evolution is very robust which can be potentially useful for several applications such as non-reciprocal light

propagation[97] and one way polarization conversion[77]. Our results indicate that when considering more complicated devices, one must take into account the complex EP landscape before making any statement about robustness of the dynamics.

4.2.4 Implementations

Here we discuss some possible implementations to observe some of the exotic effects studied in this work. In general several platforms such as photonics, acoustics, optomechanics, microwaves and electronics can be used. For sake of clarity, here we restrict our discussion to photonic systems. The implementation of the Hamiltonian H can be achieved by using four coupled resonators or waveguides as depicted schematically in Fig. 4.7(a) and (b). From the mathematical point of view, these two systems are equivalent. In the resonator arrangement, the gain and loss coefficients can be varied with time by changing the pumping beam and the system can be probed by studying the scattering coefficients under certain inputs, which can be experimentally implemented by coupling the outer resonators to waveguides as shown in Fig. 4.7(a). On the other hand, the waveguide structure provides more control since, in addition to varying the gain/loss as a function of the propagation distance z, here one can also vary the real-valued coupling coefficients (by engineering the distance between the adjacent waveguides) as well as the propagation constants of the waveguides (by tuning the width or height of the guiding channels). Some of these

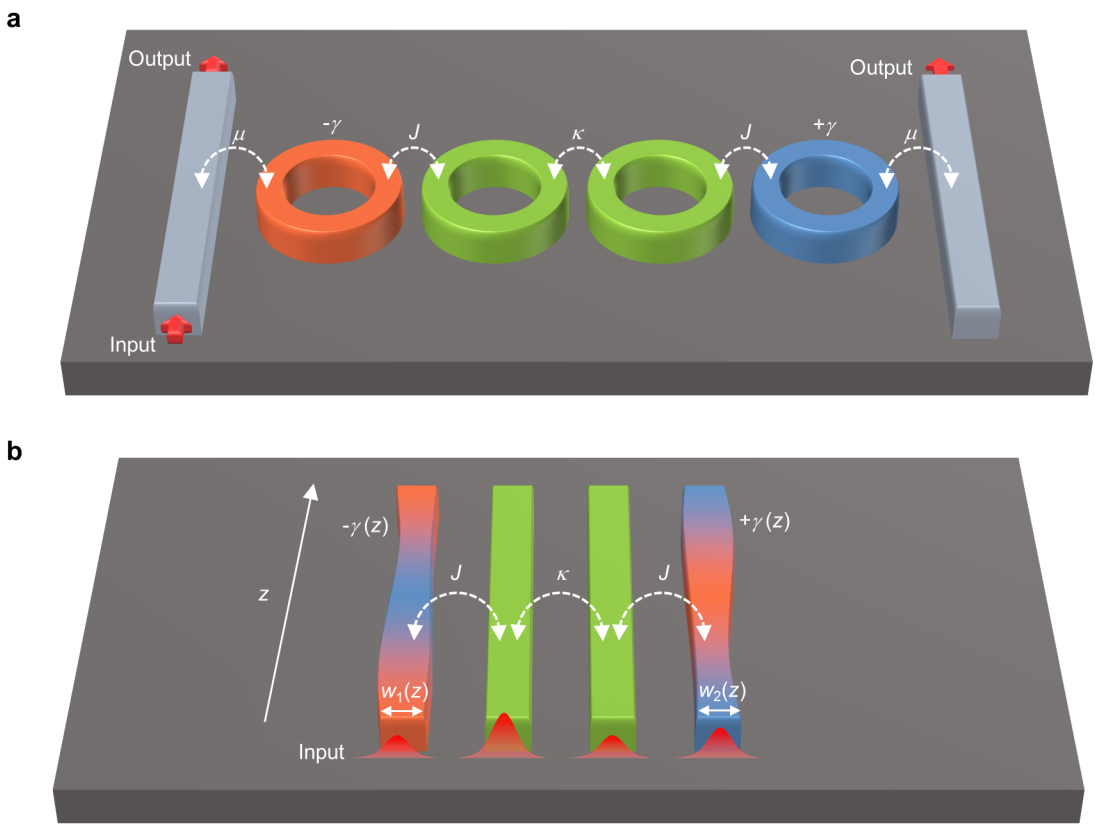

Figure 4.7: Photonic implementations. Possible photonic platforms for implementing and testing the encircling of multiple exceptional points (EPs) in (a) microring resonators; and (b) waveguides. The gain/loss can be controlled via the pumping (represented schematically by different colors, orange for gain, blue for loss, and blue for neutral.) while the coupling between adjacent elements can be tailored by engineering the edge-to-edge distance. Finally the resonant frequency (or propagation constants) can be tuned by varying the resonator (waveguide) dimensions. For stroboscopic encircling, several samples have to be fabricated, each of which corresponds to a different operating point. The eigenvalues are then plotted and connected smoothly to form the adiabatic loop as having been done before. The dynamic encircling on the other hand requires changing the parameter of one sample as a function of time (distance) in resonators (waveguides) platforms. Figure b illustrates how this can be achieved in waveguides. Particularly, the propagation constants can be varied along the prorogation distance z by changing waveguide dimensions, such as the width for example. The gain/loss can be controlled along z by engineering the spatial profile of the optical pump. White arrows indicate the coupling while red thick arrows represent the input/output signal.

ideas have been recently already explored in refs. [96, 97]. Notably, photonic implementations of the work in ref. [97] (dealing with systems that exhibit only one EP) has been recently reported[98]. Further progress will thus enable the experimental investigations of systems having multiple EPs similar to those studied here.

To confirm that these control parameters (gain, loss, propagation constants and real coupling coefficients) provide enough degrees of freedom to observe the exotic effects, we have investigated the encircling of EPs associated with the Hamiltonian H when the coupling remains constant while changing only the gain/loss values of the outermost waveguides and their propagation constants, i.e. the real and imaginary parts of γ, respectively (see Appendix 4B).

Note that for the stroboscopic encircling, one needs to build different samples, each of which is tuned to a single operating point. The eigenvalues are then measured and plotted to study the exchange relations. On the other hand, one sample with parameters that vary with distance suffices to study the dynamic encircling of EPs as has been shown in refs. [78, 79] for simple systems having only one EP.

4.3 Conclusions

In conclusion, we have introduced a general formalism based on permutation groups and representation theory for describing the stroboscopic encircling of multiple EPs. By using this tool, we uncovered the following counterintuitive results: trajectories that enclose the same EPs starting from the same parameters and traveling in the same direction, do not necessarily result in an identical exchange between the states. Instead, we have shown that this equivalence can be established only between homotopic loops. Additionally, we have also discussed the implication of these results for the dynamic encircling of EPs.

4.4 Appendix

Appendix 4A: Numerical calculation of dynamic evolution

Here we present the details of the numerical calculations for the dynamic evolution. First, we choose the point $\kappa_0 = (0.4, -0.15)$ in Fig. 4.8. Next, choose the loop ④ in

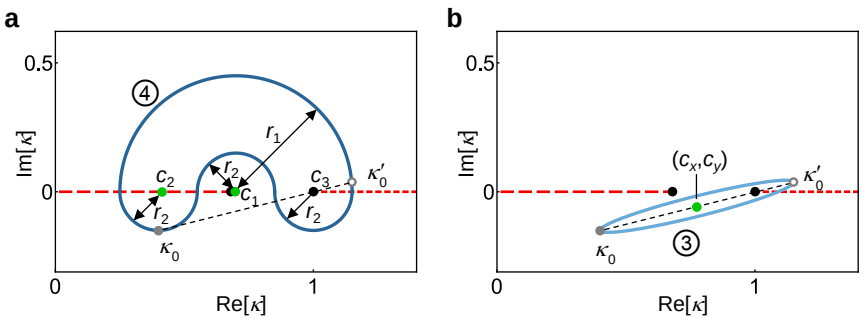

Figure 4.8: Trajectories of dynamical evolutions. The details of loops ③ and ④ (blue lines) used in the numerical simulation of dynamic evolution of eigenstates in the main text are illustrated in (a) and (b). Loop ③ is a titled ellipse with the line connecting κ_0 and κ_0' (solid and hollow gray points) as the major axis. The center of ellipse is at (c_x, c_y) (the green point). Loop ④ is a combination of one large semi-circle and three identical small semi-circles. The centers of semi-circles are labeled as $c_{1,2,3}$ with green points and c_3 locates at one exceptional point (EP). The radii are lebeled as $r_{1,2}$.

Fig. 4.8(a) as:

$$\mathrm{Re}[\kappa(\tau)] = \begin{cases} c_1 + r_1\cos(\omega\tau), & \tau \in [0, T/4) \\ c_2 + r_2\cos(\omega\tau), & \tau \in [T/4, T/2) \\ c_1 - r_2\cos(\omega\tau), & \tau \in [T/2, 3T/4) \\ c_3 + r_2\cos(\omega\tau), & \tau \in [3T/4, T] \end{cases}, \tag{4.8a}$$

$$\mathrm{Im}[\kappa(\tau)] = \begin{cases} r_1\sin(\omega\tau), & \tau \in [0, T/4) \\ r_2\sin(\omega\tau), & \tau \in [T/4, T] \end{cases}, \tag{4.8b}$$

where $c_1 = 0.7$, $c_2 = 0.4$ and $c_3 = 1$. Note that the centers of the semicircles associated with loop ④ in Fig. 4.8(a) are given by the coordinates $(c_{1,2,3}, 0)$. The associated radii are $r_1 = 0.45$ and $r_2 = 0.15$. The quantity $T = 4\pi/\omega$ is the time

needed to complete one cycle. The exact position of point κ_0' can be now chosen to be the intersection between the line passing through κ_0 and EP_1 and the top large semi-circle, and $\kappa_0' \approx (1.148, 0.03711)$.

Finally, loop ③ in Fig. 4.8(b) was chosen to be a titled ellipse with the line connecting κ_0 and κ_0' as the major axis. This ellipse has semi-major axis $a \approx 0.3858$, focal distance $c = a - 0.002$ and a rotating angle $\theta = \arctan\frac{1}{4}$. Therefore the parametric function of loop ③ is:

$$\mathrm{Re}[\kappa(\tau)] = c_x + a\cos(\omega\tau)\cos\theta - b\sin(\omega\tau)\sin\theta, \tag{4.9a}$$

$$\mathrm{Im}[\kappa(\tau)] = c_y + a\cos(\omega\tau)\sin\theta + b\sin(\omega\tau)\cos\theta, \tag{4.9b}$$

where $b = \sqrt{a^2 - c^2}$ is the semi-minor axis of the ellipse and $(c_x, c_y) = (c_2 + a\cos\theta, -r_2 + a\sin\theta)$ is the center of the ellipse.

In all simulations, we chose the encircling speed $\omega = 10^{-4}$. For each loop, the encircling in the counterclockwise/clockwise is performed by the parametrization $\tau = t_0 \pm t$, with $t \in [0, T]$ for loop ④, and $t \in [0, T/2]$ for loop ③ . Here $\tau = t_0$ corresponds to the relevant starting point: for points κ_0 and κ_0', $t_0 = \frac{3T}{8}, \frac{65T}{10^4}$ for loop ④; and $t_0 = \frac{T}{4}, 0$ for loop ③.

Appendix 4B: Varying gain/loss instead of coupling

To confirm that these control parameters (gain, loss, propagation constants and real coupling coefficients) provide enough degrees of freedom to observe the exotic effects, we briefly investigate the encircling of EPs associated with the Hamiltonian H again but this time we fix the couplings and change only the gain/loss parameters of the outermost waveguides and their propagation constants, i.e. the real and imaginary parts of the parameter γ, respectively.

Figure 4.9(a) shows two different loops in the parameter space spanned by Re[γ] and Im[γ]. Both loops encircle only EP_1, yet they are topologically inequivalent since: Loop ② cannot be deformed into loop ① without crossing EP_2; and the permutation matrices M_1 and M_2 (which are, incidentally, similar to those defined in Eq. (4.7) associated with $EP_{1,2}$) do not commute. Thus, indeed a system of four coupled waveguides with variable gain/loss and propagation constants can be used to study the topological equivalence between encircling loops in the parameter space.

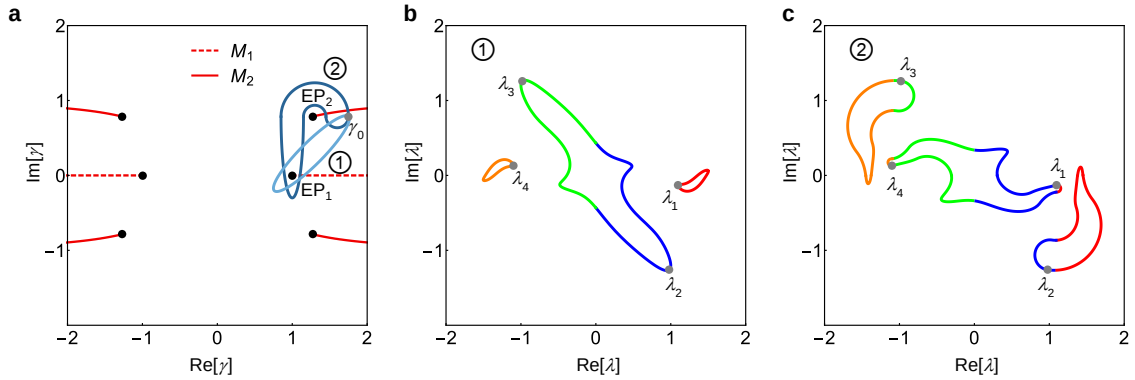

Figure 4.9: Case study using complex propagation constants. In the example considered in the previous section, we have studied H as we vary the complex coupling coefficients. While this is not impossible, it is rather difficult to achieve experimentally. An easier approach that lends itself to an easier experimental implementation is to change the complex propagation constant which corresponds to changing the real propagation constants and the gain/loss factors. Here we confirm that the main features of this work can be still observed under these conditions. (a) The exceptional points landscape of H in a two-dimensional parameter space spanned by Re[γ] and Im[γ]. One can identify two topologically inequivalent loops (blue lines) that encircle the exceptional point EP$_1$. (b) and (c) show the eigenvalue exchange relations associated with these two loops, confirming their nonequivalence. Black dots represent exceptional points, red lines are the branch cuts. The colors along the eigenvalue trajectory indicate the branch at which the relevant eigenvalue is located.

Chapter 5

Sensing with exceptional surfaces

5.1 Introduction

Exceptional points (EP) are peculiar singularities that arise in non-Hermitian Hamiltonians when two or more eigenstates coalesce [27, 28, 29, 30, 31, 32]. The resultant reduction in the eigenstate space dimensionality renders these points very sensitive to any external perturbations. Current research works in non-Hermitian and parity-time (PT) symmetric physics [1, 2] have so far focused on systems supporting isolated EPs in a reduced parameter space. This strategy has allowed researchers to investigate

The contents in this chapter were previously published in Physical Review Letters 122 (15), 153902 (2019). Refer Appendix A.4 for granted permission to be republished.

certain important aspects of non-Hermitian systems and gain insight into their behavior [8, 11, 12, 13, 22, 52, 99, 100, 101, 102, 103, 104, 105, 106, 107, 108]. This however comes at a price: isolated EPs are very sensitive to unavoidable fabrication errors or experimental uncertainty (e.g. small variation in the experimental conditions). To better appreciate this point, consider the current implementations of photonic EPs based on PT-symmetric coupled elements [8, 11, 12, 99] or engineered back reflection [19, 21, 38, 109]. In both of these geometries, which have been recently exploited to demonstrate ultra-responsive optical sensors [20, 21], the design parameters have to be tailored precisely in order to force the system to operate at an EP. In the PT-symmetric implementation [20], the resonant frequencies of the two rings have to be identical; the gain/loss profiles have to be exactly balanced; and the difference between the gain and loss values has to match the coupling coefficient between the two resonators. Alternatively, in the single ring implementation [19, 21, 38, 109], the sizes and locations of the nanoscatterers next to the ring have to be controlled with high precision during the fabrication. To overcome these difficulties, various research teams employ clever techniques (such as micro-heaters and movable fiber tips, tunable coupling, etc) in order to actively and continuously tune the studied systems in the vicinity of the EPs. Beyond these important proof-of-concept demonstrations, it will be extremely useful for practical sensing applications to advance new design concepts that decouple the effects of fabrication errors and experimental uncertainties from perturbations caused by measurements.

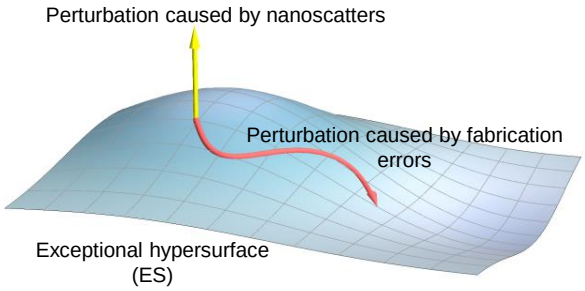

Figure 5.1: A non-Hermitian photonic structure can combine robustness together with sensitivity if it exhibits a hypersurface of exceptional points with the following properties: (1) Undesired perturbations due to fabrication imperfections and experimental uncertainties shift the spectrum across the surface, leaving the system at an EP; (2) Perturbations accounting for the quantities to be measured force the spectrum out of the surface, i.e. away from EPs.

In this chapter, we present a new non-Hermitian photonic structure that exhibits an exceptional hypersurface (ES) embedded in a high-dimensional parameters space. This, in turn, provides additional degrees of freedom that can be exploited to combine robustness with enhanced sensitivity. Particularly, robustness can be achieved if the system's response is tailored such that a large class of fabrication errors and experimental uncertainties shift the operating point along the ES. On the other hand, enhanced sensitivity can arise if the perturbation due to the measurements forces the spectrum away from the ES, causing large splitting of the resonant frequency (as compared to that associated with diabolic points (DP) [110, 111, 112, 113, 114, 115, 116]). This generic concept is illustrated schematically in Fig. 5.1. Here we show that this concept can be implemented by using standard photonic technology, which paves the way towards practical applications of non-Hermitian photonic sensors.

5.2 Theoretical analysis

5.2.1 Eigenvalues analysis based on coupled mode theory

To this end, we consider the structure depicted schematically in Fig. 5.2. It consists of a single microring resonator coupled to a waveguide. One end of this waveguide is terminated by a mirror while the other end is assumed to be reflectionless (see Appendix 5A for the effect of finite small reflectivity). Within the context of coupled mode theory, the above structure in the absence of the scatterer can be described by the effective Hamiltonian:

$$i\frac{d}{dt}\begin{bmatrix}\tilde{a}_{\mathrm{cw}}\\ \tilde{a}_{\mathrm{ccw}}\end{bmatrix} = H_{\mathrm{ES}}\begin{bmatrix}\tilde{a}_{\mathrm{cw}}\\ \tilde{a}_{\mathrm{ccw}}\end{bmatrix}, H_{\mathrm{ES}} = \begin{bmatrix}\omega_0 - i\gamma & 0\\ \alpha\mu^2 & \omega_0 - i\gamma\end{bmatrix} \tag{5.1}$$

where $\tilde{a}_{\mathrm{cw,ccw}}$ are the field amplitudes of the clockwise (CW) and counterclockwise (CCW) modes, ω_0 is the resonant frequency, γ is the cavity loss rate which can be decomposed into intrinsic absorption, radiation loss, and loss to the waveguide (i.e. $\gamma = \gamma_{\mathrm{abs}} + \gamma_{\mathrm{rad}} + \mu^2/2$), and μ quantifies the coupling rate between the resonator and the waveguide. In addition, $\alpha = r_m \exp(i2\phi_3)$ where r_m is the field reflection coefficient at the mirror and $\phi_3 = \beta_w L_3$. Here β_w is the propagation constant of the waveguide and the distances L_3 are depicted in Fig. 5.2. Note that the above

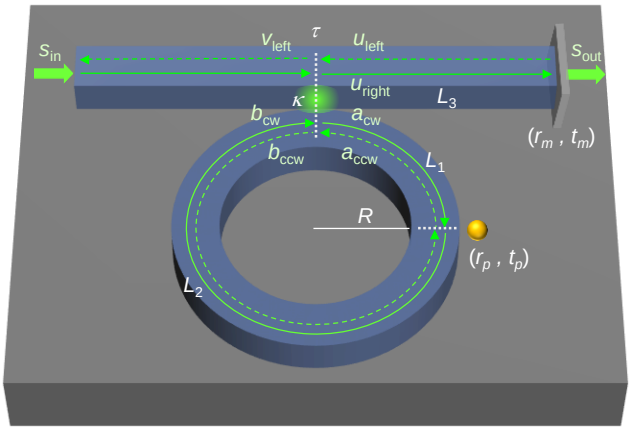

Figure 5.2: Schematic diagram of the proposed photonic structure that satisfies the criteria mentioned in Fig. 5.1. It consists of a microring resonator coupled to a waveguide that has a mirror on one side and reflectionless at the other end. The relevant design parameters are indicated in the figure. In the absence of any reflective perturbations, the system exhibits an EP. Any variations of the coupling coefficients or the resonant frequency of the cavity will still leave the system at an EP. On the other hand, if a nanoscatterer (or any other form of reflective perturbations) comes to the vicinity of the ring, it will introduce a bidirectional coupling between the clockwise (CW) and counterclockwise (CCW) waves and shift the system away from the EP which in turn will leave a fingerprint on the emission spectrum of the system (if used in the lasing regime) or the power scattering spectrum (if operated in the amplification regime).

form of the Hamiltonian does not imply that the system is nonreciprocal, i.e. the transmission between the input and out ports is the same if the role of the two ports is reversed.

The eigenvalues of H_{ES} as written in the bases $\exp(-i\omega t)$, together with the associated eigenvectors $\tilde{\mathbf{a}}_{1,2}$ are given by:

$$\begin{aligned} \omega_{1,2} &= \omega_0 - i\gamma, \\ \tilde{\mathbf{a}}_{1,2} &= (0,1)^{\mathsf{T}}. \end{aligned} \tag{5.2}$$

The spectrum of the Hamiltonian H_{ES} features an EP with two identical eigenmodes characterized by a finite CCW component and a null CW component. Importantly, this is even true for any value of ω_0, γ and $\alpha\mu^2$. In other words, there is hypersurface spanned by all possible values of these parameters where the system remains at an EP. For instance, if the fabricated system has extra (less) loss, stronger (weaker) coupling to the waveguide or a shift in its resonance frequency from the original targeted values, the system will be still located at an EP without the need for any external tuning. Only perturbations that introduce differential loss, frequency mismatch or additional couling between the two modes (CW and CCW) can affect the system performance. However, these perturbations do not arise naturally in our proposed design since any change in the size of the resonator or its coupling to the waveguide will affect both modes symmetrically (see Appendix 5B). This unique feature provides unprecedented robustness that cannot be achieved in standard non-Hermitian systems that rely on isolated EPs in the design parameter space. However, in the presence of a nanoscatterer located in the vicinity of the ring resonator, the interaction between the scatterer and the evanescent field of the optical modes introduces a bidirectional coupling between the CW and CCW modes, which are described by additional corrections of the same order to both off-diagonal matrix elements of H_{ES}, say ϵ. If we further assume that ϵ is much smaller than other matrix elements, it is straightforward to show that the splitting of the eigenfrequency is $\Delta\omega \equiv |\omega_1 - \omega_2| \sim \sqrt{\epsilon}$. In standard waveguide-coupled microring resonators operating at a diabolic point, this

splitting will be rather ϵ. Thus, in addition to its robustness, the proposed system is expected to also provide enhanced sensitivity.

5.2.2 Frequency splitting based on scattering matrix method

In order to put this discussion on a more solid ground while at the same time elucidate on the relevant experimental parameters, we study the above structure using the scattering matrix method (SMM) [117, 118, 119]. Here we assume that the system is probed via the waveguide by a signal s_{in}. We then proceed to calculate the output signal s_{out} as a function of the input frequency for different levels of perturbation by a nanoscatterer, which we quantify by its location as well as reflection/transmission coefficients r_p/t_p, respectively.

The scattering matrices associated with the evanescent coupling region S_c, the partially reflective mirror, and nanoscatterer are given by:

$$S_c = \begin{bmatrix} \tau & i\kappa \\ i\kappa & \tau \end{bmatrix}, \; S_m = \begin{bmatrix} t_m & ir_m \\ ir_m & t_m \end{bmatrix}, \; S_p = \begin{bmatrix} t_p & ir_p \\ ir_p & t_p \end{bmatrix}, \tag{5.3}$$

where κ is the coupling between the waveguide and ring resonator, τ is the transmission and they satisfy $\kappa^2 + \tau^2 = 1$ (assuming no loss); $r_{m,p}$ and $t_{m,p}$ are the reflection and transmission coefficients of the mirror and scatterer, respectively, and satisfy $r_{m,p}^2 + t_{m,p}^2 = 1$ (again assuming no loss). All these parameters are real positive

numbers.

The electric fields components of Fig. 5.2, with the internal components calculated at the coupling regions (dashed lines of Fig. 5.2) are then given by [118]:

$$\begin{aligned}
\begin{bmatrix} u_{\text{right}} \\ a_{\text{cw}} \end{bmatrix} &= S_c \begin{bmatrix} s_{\text{in}} \\ b_{\text{cw}} \end{bmatrix}, \\
\begin{bmatrix} v_{\text{left}} \\ b_{\text{ccw}} \end{bmatrix} &= S_c \begin{bmatrix} u_{\text{left}} \\ a_{\text{ccw}} \end{bmatrix}, \\
\begin{bmatrix} b_{\text{cw}} \exp(-i\phi_2) \\ a_{\text{ccw}} \exp(-i\phi_1) \end{bmatrix} &= S_p \begin{bmatrix} a_{\text{cw}} \exp(i\phi_1) \\ b_{\text{ccw}} \exp(i\phi_2) \end{bmatrix}, \\
\begin{bmatrix} s_{\text{out}} \\ u_{\text{left}} \exp(-i\phi_3) \end{bmatrix} &= S_m \begin{bmatrix} u_{\text{right}} \exp(i\phi_3) \\ 0 \end{bmatrix}.
\end{aligned} \tag{5.4}$$

Note that material and radiation loss as well as gain can be incorporated in the imaginary components of the phases $\phi_{1,2,3}$. It is straightforward to drive the formula for the transmission spectrum from the above set of equations.

By doing so, we obtain:

$$\frac{s_{\text{out}}}{s_{\text{in}}} = \frac{e^{i\phi_3} t_m [(1 + e^{2i\phi})\tau - e^{i\phi}(1 + \tau^2) t_p]}{1 + e^{i2\phi}\tau^2 - 2e^{i\phi}\tau t_p - e^{2i\phi'} r_m r_p \kappa^2} \equiv \frac{N}{D}, \tag{5.5}$$

where $\phi = \phi_1 + \phi_2$ and $\phi' = \phi_2 + \phi_3$, with $\phi_{1,2} = \beta_r L_{1,2}$ and $\phi_3 = \beta_w L_3$. In general, the values of propagation constants associated with the ring and straight waveguides, $\beta_{r,w}$, can be complex with the imaginary parts accounting for the possible radiation

and material loss as well as the gain (loss due to coupling to the waveguide is treated separately). For reasons that will be clear shortly, we are particularly interested in the case of active devices where the microring exhibits enough optical gain to bring the system at or close to the lasing condition (for completeness we treat the passive case in Appendix 5C). Under either of these conditions, the lasing or the transmission spectrum (respectively) is dominated by the the poles of the power scattering coefficient $T = |s_{\text{out}}/s_{\text{in}}|^2$, or equivalently the zeros of D. To characterize the performance of the proposed structure, we thus study the behavior of D as a function of the particle reflectivity r_p and the input frequency parametrized by ϕ (we do not take the waveguide dispersion into account at this moment), i.e. $D \equiv D(r_p, \phi)$.

For any set of design parameters and a specific value of r_p, the lasing conditions is achieved for values of $\phi \equiv \phi_D$ satisfying the equation $D(r_p, \phi_D) = 0$, which gives $\exp(i\phi_D^{\pm}) = \tau^{-1}(t_p \pm i\sqrt{r_p^2 - \exp(2i\phi')r_m\kappa^2 r_p})$. The maximum frequency splitting $\Delta\phi \equiv \text{Re}[\phi_D^+ - \phi_D^-]$ occurs when $\exp[2i\text{Re}(\phi')] = -1$. As a side comment, we note that $\text{Im}[\phi_D] = -\kappa^2/2$, which implies the lasing threshold occurs when the gain is enough to compensate for the radiation/material loss as well as the loss due to coupling to the waveguide, as one would expect. By writing $r'_m = r_m \times |\exp(2i\phi')|$ we find:

$$\Delta\phi = 2\sqrt{r_p^2 + r'_m\kappa^2 r_p}. \tag{5.6}$$

In Eq. (5.6), $r'_m\kappa^2$ is the effective unidirectional coupling from CW mode to CCW

mode. By noting that in our systems, both r_m and $|\exp(2i\phi')| = \exp(-2\mathrm{Im}[\phi'])$ are in the order of unity (since the system is assumed to operate below but close to the lasing threshold), we arrive at:

$$\Delta\phi_{\mathrm{EP}} \approx \begin{cases} 2\kappa\sqrt{r_p}, & r_p \ll \kappa^2 \\ 2r_p, & r_p \gg \kappa^2 \end{cases}, \tag{5.7}$$

$$\Delta\phi_{\mathrm{DP}} = 2r_p. \tag{5.8}$$

Equation (5.7) is the central result of this work. It confirms the existence of an operating regime ($r_p \ll \kappa^2$) where the frequency splitting scales with the square root function of the perturbation, which is the hallmark of enhanced sensitivity near a second-order EP. Beyond this regime, the splitting is linear as in standard sensors operating at a diabolic point. Intuitively, as the perturbation due to the scatterer shifts the system far away from the EP, the extra sensitivity is lost. In comparison, as shown by Eq. (5.8), which describes the same non-Hermitian system in the absence of the mirror (i.e. operating at a DP), the splitting is linear from the very beginning.

In the active scattering regime, when the gain brings the system relatively close to the lasing point but remains below the lasing threshold, the transmission peaks can be obtained by solving Eq. (5.5). Not surprisingly, here also the locations of the transmission peaks are dominated by the zeros of $D(r_p, \phi)$, which again results in a

square-root dependence of the frequency splitting as we have confirmed numerically.

5.3 Implementation and full-wave simulation

Having discussed the essential features of the proposed structure, we now confirm our predictions by performing two-dimensional(2D) full-wave Finite-Difference Time-Domain (FDTD) simulations [120] using realistic material platforms. Particularly, we study a 2D version of the schematic shown in Fig. 5.2. It consists of a microring resonator having a refractive index $n_2 = 1.45$, a radius $R = 10$ μm, and a width $w = 0.8$ μm. The ring is coupled to a waveguide having the same material and width. The edge-to-edge separation between the ring and the waveguide is chosen to be $d = 0.6$ μm, corresponding to $\kappa^2 = 0.028$. A mirror with reflectivity $r_m = 0.99$ is introduced at one end of the waveguide via a 50-nm-thick silver layer. To simulate the perturbation induced by a nanoscatterer, we use a disk assumed to be of the same material with the waveguide and vary its radius in the simulation from 20 nm to 100 nm. The disk is located at 3 o'clock with a fixed distance $h = 0.1$ μm from its center to the outside of the microring. Based on the chosen position of the nanoscatterer, we set L_3=10.075 μm, which results in an optimal operation (defined by the maximum frequency splitting and peak visibility) for a test particle having a 30 nm radius. Finally, the background material is assumed to be air of $n_1 = 1$. In our simulations, the device is probed by a TE-polarized broad bandwidth pulse with

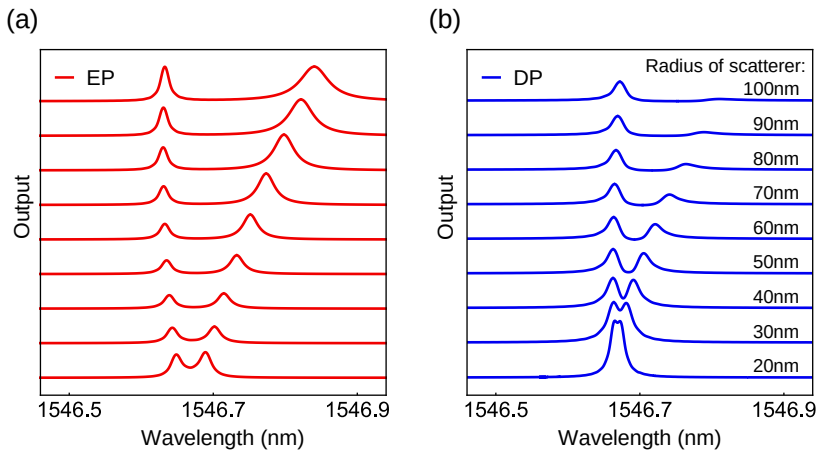

Figure 5.3: Finite difference time domain simulations for a system similar to that of Fig. 5.2. (a) and (b) plot the spectrum splitting as a function of nanoscatterer size. Clearly, the EP-based structure demonstrates superior performance in terms of the splitting magnitude and the visibility of the resonance peaks.

central frequency at $f = 193.4$ THz or equivalently $\lambda = 1550$ nm (almost matching one of the longitudinal modes of the microring) launched from the left side of the waveguide. In order to isolate the relevant transmission peaks in our simulations, we used a dispersive gain function as described in Appendix 5D.

Figures 5.3(a) and (b) show the transmission spectrum for the cases of EP and DP, respectively for the parameters listed in the figure caption. Evidently, the EP-based device exhibits a significant advantage, demonstrating larger splitting and clear transmission peaks. Note that the location of one transmission peak remains almost invariant while the other experience red-shift. This can be explained by the scatterer-induced coupling between different wave components [121**?**]. A more quantitative explanation based on perturbation theory is also provided in Appendix 5E. Figure

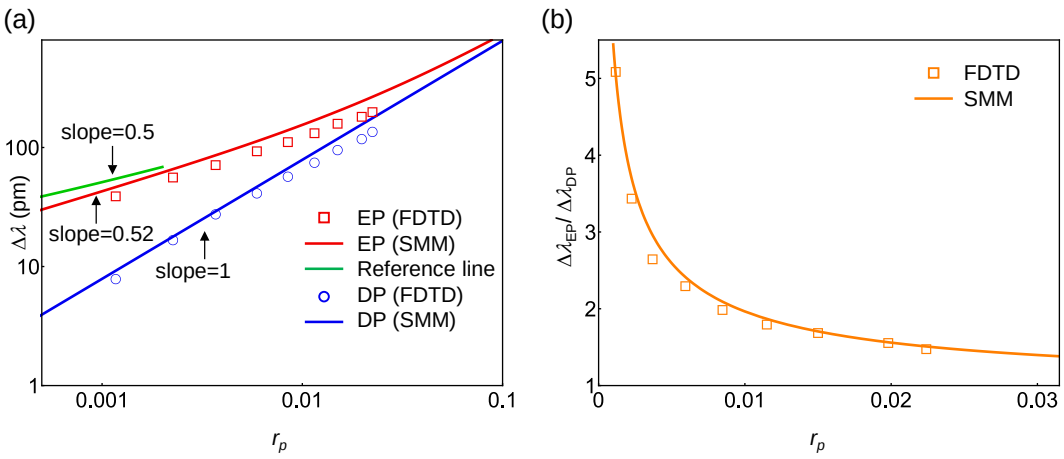

Figure 5.4: Sensitivity enhancement as a function of the nanoscatterer radius. Clearly the EP sensor has a better performance than a sensor operating at a DP for smaller scatterer, making this device valuable for measuring small perturbations. In producing the solid lines, we first used FDTD simulations to simulate subsystems of the full structure to extract the design parameters (for example, using the waveguide and mirror only without the resonator to compute the mirror reflectivity; or the ring resonator only and the scatterer to compute the scatterer reflectivity, etc). Next, we used these extracted parameters in our analytical formulas (4-6) together with the definition of ϕ in order to produce the solid lines.

5.4(a) plots a log-log scale of the slopes characterizing the magnitude of the splitting, where the superior performance of EP is evident. This conclusion is better illustrated in Fig. 5.4(b), which depicts the enhancement factor (defined as the ratio of the splitting in the EP case normalized by that of the DP case) of the proposed sensor as a function of the nanoscatterer reflectivity r_p when the scatterer size is varied from 20 nm to 100 nm (Appendix 5F). These figures also demonstrate the excellent agreement between the FDTD (square points) and the scattering matrix method (solid lines).

5.4 Conclusions

In conclusion, we have proposed a new class of non-Hermitian sensors that operate at exceptional surfaces as opposed to isolated exceptional points. This new paradigm provides more degrees of freedom that can be exploited to combine a certain degree of robustness against fabrication tolerance (which is crucial for real-life applications) together with the enhanced sensitivity associated with exceptional points. We also expect our proposed system to demonstrate some robustness against the type of thermal fluctuations studied recently in [122] (see Appendix 5G). Interestingly, it was recently shown that non-Hermitian Hamiltonians with unidirectional coupling (i.e. similar to that used in our proposed work) can exhibit superior performance even in the quantum regime [123]. We anticipate that our results, together with recent work on exceptional surface in photonic crystals [124], will open a host of new possibilities for sensing applications using practical non-Hermitian devices. Importantly, the proposed design concept presented here can be implemented in other physical platforms such as acoustics or microwaves.

5.5 Appendix

Appendix 5A: Eliminating reflection from input port

As we discussed in the main text, an important condition for our proposed system to function properly is to eliminate or minimize (compared to other parameters) the reflection from the input port. In the context of laser engineering, various techniques have been developed to minimize port reflection. These include cleaving the waveguide end at slanted angles [125, 126] and using anti-reflection coatings [127]. Power reflection values as low as $\sim 10^{-7}$ have been reported [125]. In addition to these methods, one can also utilize absorption. For instance, if the far end of the waveguide is coupled to a resonator that has a high loss, then, the total reflection can be further reduced by orders of magnitude. The use of optical circulators with high isolation ratios is another approach [128]. Recently, a novel technique based on Kramers-Kronig relation was also proposed to eliminate reflections [129]. We plan to explore these different design strategies in future work. In our simulations, this reflection was eliminated by implementing absorbing boundary conditions at that port [120].

Appendix 5B: Effect of surface roughness and resonator's shape

As we mentioned in the main text, our proposed structure of Fig. 5.2 is robust against a certain class of perturbation that includes a variation in the mirror reflectivity, the ring size and the strength of the coupling between the ring and the waveguide. However, other perturbation that does not belong to this class must be considered. Particularly, two classes of perturbation are important: (1) those induced by resonator shape variation; and (2) those arising from surface roughness. Both types can introduce additional coupling between the CW and CCW modes [109, 130, 131]. If the magnitude of these coupling is strong, it will degrade the device performance. We note however that current fabrication technology is mature enough to avoid these perturbations. For example, microtoroid and microsphere resonators with close to perfect geometry are routinely fabricated [132, 133, 134]. Also surface roughness in silica, silicon and silicon nitride platforms can be currently reduced below 0.5 nm, which is far smaller than the particle sizes considered here (larger than 20 nm). The crucial observation here is that, as long as the scattering induced by the surface roughness is much smaller than the scattering by the nanoparticle, the system will still operate in the vicinity of the EP and demonstrate the enhancement described by the square root splitting. In fact, our FDTD simulations inevitably introduce some

parasitic reflection due to the finite mesh size (smallest size used in our simulations was 10 nm which introduces numerical surface roughness), yet excellent agreements between these simulations and the analytical predictions are observed.

Appendix 5C: Passive EP sensors

In the main text, we considered the operation of the system only in the amplification and lasing regimes. Here, for completeness, we also analyze the passive structure, i.e. when no gain is applied. Under this condition, the transmission spectrum is dominated by the zeros of numerator term N in Eq. (5.5), denoted by ϕ_N, which correspond to dips in the transmission and given by:

$$\exp(i\phi_N) = Kt_p \pm \sqrt{K^2 t_p^2 - 1}, \tag{5.9}$$

where $K = (\tau + 1/\tau)/2$. By recalling that $\kappa = \sqrt{1-\tau^2}$, and noting that in our system $\kappa \ll 1$ (in fact, $\kappa \sim 0.167$ in our FDTD simulations), we find that $K \sim 1 + \frac{\kappa^4}{8} + O(\kappa^6)$, which leads to a complex frequency splitting $\phi_N^{\pm} = \pm\sqrt{r_p^2 - \kappa^4/4}$. Thus, only when $r_p > \kappa^2/2$, $\Delta\phi_N \equiv \phi_N^+ - \phi_N^- = 2\sqrt{r_p^2 - \kappa^4/4}$ is real and correspond to two dips in the transmission spectrum. When $r_p > \kappa^2/2$, the complex splitting correspond to a change in the modal lifetime [135]. These results apply equally for DPs and EPs.

The situation becomes drastically different if we consider the reflected signal instead

of the transmitted one as we have done so far. In this case, we are interested in the quantity:

$$\frac{v_{\text{left}}}{s_{\text{in}}} = \frac{ie^{-2i\phi_3}[e^{2i\phi}r_m - 2e^{i\phi}t\tau r_m + \tau^2 r_{\text{m}} - e^{2i(\phi-\phi')}r\kappa^2]}{1 + e^{i2\phi}\tau^2 - 2e^{i\phi}\tau t_p - e^{2i\phi'}r_m r_p \kappa^2}. \tag{5.10}$$

By assuming $r_m \sim 1$ and $\exp(2i\phi') \sim -1$, the reflection vanishes (i.e. $v_{\text{left}} = 0$) when:

$$\exp(i\phi_N) = \frac{\tau}{1 + r_p\kappa^2}(t_p \pm i\sqrt{r_p^2 + \kappa^2 r_p}). \tag{5.11}$$

As expected, $\text{Im}(\phi_N) = \frac{\kappa^2}{2}$ which gives the condition for critical coupling [136]. Surprisingly however, in this case, we have $\text{Re}(\phi_N) = \pm\sqrt{r_p^2 + \kappa^2 r_p}$. Thus for very small values of r_p, the splitting is $\sim 2\kappa\sqrt{r_p}$ as in the active device.

Appendix 5D: Gain dispersion

The material gain in the FDTD simulation is assumed to depend on the light frequency via a Lorentz dispersion model:

$$\varepsilon_{\text{total}}(\omega) = \varepsilon + \frac{\varepsilon'\omega_0^2}{\omega_0^2 - 2i\delta\omega - \omega^2} \tag{5.12}$$

with $\varepsilon = 1.45^2$; $\omega_0 = 1.2179 \times 10^{15}$ rad/s (corresponding to $\lambda = 1546.7$ nm); $\delta = 2\times10^{12}$ rad/s; $\varepsilon' = -4.5\times10^{-7}$ corresponds to an imaginary index around -4.7×10^{-5} at resonance.

Appendix 5E: Asymmetric shift in the transmission peaks

As noted in the discussion associated with Fig. 5.3, the frequency splitting induced by the scatterer is asymmetric with respect to the center frequency of the microring resonator in the absence of any scattering. This effect is discussed in Refs. [128**?**]. Following a similar line of arrangement, here we present a more quantitative explanation of this observation. To do so, we consider the field distribution associated with the two standing waves. The particle breaks the continuous rotational symmetry of the ring, resulting in two standing wave modes. The electric field profiles of these modes are arranged in a such a way that the particle is located at the antinode of one mode (Fig. 5.5(a)), and the node of the other (Fig. 5.5(b)). According to the perturbation analysis of Maxwell's equations [137], the first-order correction to the eigenvalues (resonant frequencies), of modes $|E_{1,2}\rangle$ are given by: $\omega_{1,2}^{(1)} \propto \langle E_{1,2}| \hat{V}_P |E_{1,2}\rangle$, where $\hat{V}_P$ represents the perturbation due to the scatterer (variation in geometry and/or refractive index). If we now consider an ideal limiting case where $\hat{V}_P$ can be treated as a delta function, we find that $\langle E_2| \hat{V}_P |E_2\rangle = 0$ (because $|E_2\rangle = 0$ at the location of the scatterer). Conversely, $\langle E_1| \hat{V}_P |E_1\rangle$ is a finite, non-zero quantity. This simplification illustrates intuitively the reason for the asymmetric shift in the peaks locations.

In reality, the scatterer is not a delta function and its real geometry can be taken into account by using the formal perturbation analysis [137]. This will still result in

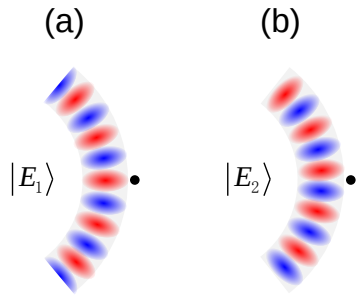

Figure 5.5: A schematic figure (not simulations) that shows the electric field distribution of standing wave modes of a microring resonator in the presence of a scatterer. The scatterer is located at the antinode/node of the two modes $|E_{1,2}\rangle$, respectively.

a stronger shift for ω_1 than for ω_2. We point out that such elaborate perturbation analysis is not necessary in our current work since our FDTD simulations treat the effect of the particle non-perturbatively.

Appendix 5F: Reflection from nanoscatterer

In our scattering matrix formalism, the scatterer was quantified via its reflection r_p and transmission t_p coefficients, respectively. To extract these parameters for realistic designs, we used FDTD simulations for the structure shown in the inset of Fig. 5.6. It consists of a half ring and the scatterer. A ring waveguide mode is launched from the top in the CW direction and the reflected CCW and transmitted CW waves are measured at the top (detector D_1) and lower (detector D_2) ports. Absorbing boundary conditions are added at these ports to avoid undesired reflections. The reflection coefficient as a function of the scatterer size is shown in Fig. 5.6. Note

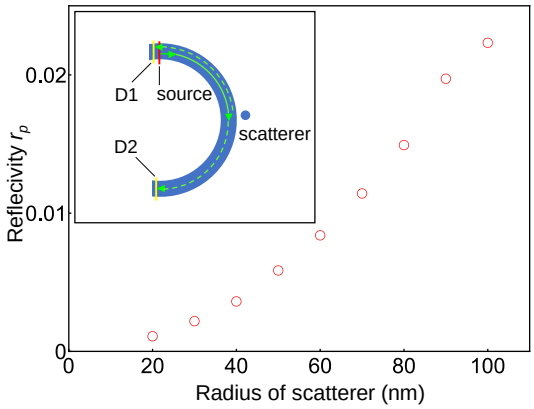

Figure 5.6: An input wave having wavelength 1550 nm is launched from the top port of the half ring waveguide. The reflected wave is measured by a numerical detector (D_1) located to the left of the input. Similarly, the transmission is obtained by D_2. A perfectly matched layer (PML) is used to avoid unphysical reflections.

that, while in the scattering matrix formalism we assumed real values of r_p, and that $t_p^2 + r_p^2 = 1$, we have not made any such assumptions in the FDTD calculations (in fact, according to FDTD, $t_p^2 + r_p^2 = 0.988$ for a 100 nm scatterer). Despite that, good agreement between both methods is observed.

This can be understood by noting that for small particle sizes (small compared to the wavelength of the probe light), the light-particle interaction is well described within the Rayleigh scattering regime. In this case, the phase of the scattered light (reflected and transmitted in our case) is not very sensitive to the particle size. This fact was further analyzed in details in [138] where it was shown that the combined phase of the reflection and transmission coefficients remains negligible for particle sizes of 100 nm (see Fig. 2(c) of [138]). By extrapolating to the case where the particle is absent, we can infer that this imply that the individual phases of the reflection and transmission

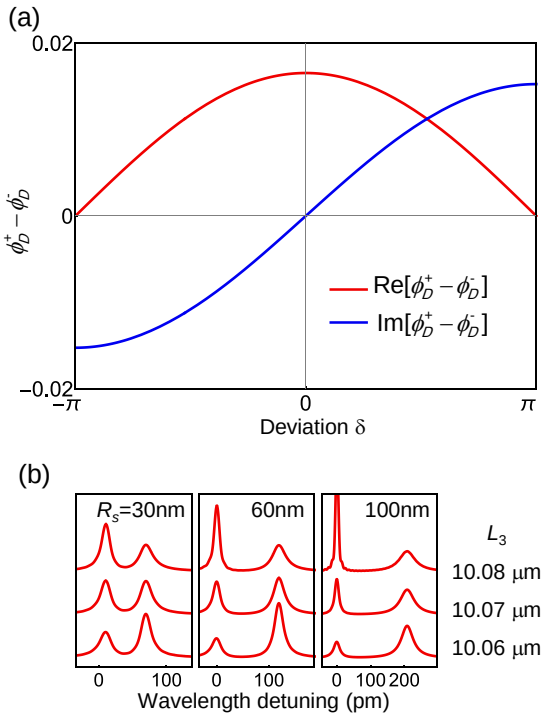

Figure 5.7: (a) Real and imaginary parts of $\phi_D^+ - \phi_D^-$ for a 30-nm scatterer as a function of the phase associated with the amplitude reflection coefficient δ as obtained using scattering matrix formalism. As explained in the text, the derivative of the curves at $\delta = 0$ indicate that the frequency splitting is less sensitive to the phase variations than the values of the transmission peaks themselves. This observation is confirmed by using full wave FDTD simulations for different scatterer size (R_s) in (b). In these simulations the phase was varied by changing the location of the mirror.

coefficients are negligible. Even more, in this regime, it was predicted that the actual shape of the particle does not matter (see section IV.A of Ref. [38]). Even if this small variation is taken into account in the analytical model, as it turns out the frequency splitting as expressed by $\mathrm{Re}[\phi_D^+ - \phi_D^-]$ is not very sensitive to this quantity. To see that, we plot $\mathrm{Re}[\phi_D^+ - \phi_D^-]$ and $\mathrm{Im}[\phi_D^+ - \phi_D^-]$ as a function of the phase δ in Fig. 5.7. In doing so, we use the expression $\exp(i\phi_D^{\pm}) = \tau^{-1}(t_p \pm i\sqrt{r_p^2 - \exp(2i\phi')r_m\kappa^2 r_p})$ and assume that $r_p = |r_p|e^{i\delta}$. Clearly, $\frac{\partial(\mathrm{Re}[\phi_D^+ - \phi_D^-])}{\partial\delta}|_{\delta=0} = 0$.

Thus the frequency splitting is sensitive only to the second order variation of the phase. Note however, that the derivative of $\mathrm{Im}[\phi_D^+ - \phi_D^-]$ (which indicates the differential lasing thresholds at resonant frequencies) is finite. This latter observation means that the values of the transmission peaks (which depends on distance to the lasing thresholds at the corresponding frequencies) can be sensitive to the phase. To confirm these predictions, we have conducted a series of additional numerical studies for different scatterer sizes. In order to control the phase, we have changed the mirror location with a resolution of 10 nm as shown in Fig. 5.7. In accord with our analysis, we observe that the frequency splitting between the peaks is less sensitive to the change of the mirror position (or equivalently to the resultant additional phase factor) than the values of the peaks themselves.

Appendix 5G: Temperature sensitivity

In addition to being robust against fabrication errors, our proposed device can also withstand wide range of temperature variation, which can be quickly checked by noting that the thermal coefficient of silica dn/dT is around 12×10^{-6} K^{-1} [139]. Assuming a ring resonator of radius $R = 10$ μm and a temperature change is $\Delta T =$ 20 K. The estimated length $L_2 + L_3$ corresponding to ϕ' can be equal to the perimeter

of the ring, the shift in the value of ϕ' is:

$$\Delta\phi' = \frac{4\pi^2 R \frac{dn}{dT} \Delta T}{\lambda} = 0.06, \tag{5.13}$$

which is very small and does not affect the performance significantly. Note that the thermal expansion of silica, $\approx 0.5 \times 10^{-6}$ K^{-1}, can be safely neglected.

Thus our analysis shows that a temperature variation within ± 20 K around the optimal operation point can be easily tolerated by our device.

Chapter 6

Exceptional points-based optical amplifiers

6.1 Introduction

The quest for new photonic devices and functionalities is currently pushing the limit for novel design paradigms and material platforms. One of the most fundamental processes in optical science and engineering is signal amplification. Current amplification mechanisms include incoherent pumping (atomic or band inversion followed

The content in this chapter was accepted by Physical Review Applied. It can aslo be found at arXiv:1904.13005

by stimulated emission) or coherent pumping (such as in nonlinear wave mixing processes). Based on their geometry, semiconductors optical amplifiers (OAs) [140, 141] can be classified into traveling [142] or standing [143] waves devices. The former offers a larger bandwidth of operation at the expense of the attainable gain values and footprint (few millimeters in length). On the other hand, the latter can have larger gain due to the power recycling in the resonator which allows for a much smaller device size, suitable for large scale integration. However, the same resonant condition leads to a very narrow bandwidth. This fundamental limitation pertinent to cavity-based optical amplifiers (and generally also electronic and microwave amplifiers) is known as the gain-bandwidth product and is often expressed as: $\chi = \sqrt{G} \cdot B = \text{const.}$ [144], where G is the maximum gain and B is the bandwidth (which is usually defined as full width at half maximum (FWHM) of the power gain curve — here we adopt this definition). Relaxing this constraint beyond its standard scaling will enable a new level of integration for high-performance photonic circuits. Going beyond the standard gain-bandwidth limit has been studied in parametrically driven coupled-mode systems [145, 146, 147, 148, 149]. There one combines parametric amplification with frequency conversion processes, which effectively removes the instability introduced by the amplification process. Such multi-tone setups require well controlled pump-amplitudes and demand strong external driving, which can be rather challenging for the operation of the amplifier in terms of its stability. Thus it would be desirable to develop simpler designs which exhibit improved gain-bandwidth behavior.

In this chapter, we introduce a new OA scheme based on optical resonators operating at exceptional points (EPs) – a special type of singularities that arise in non-Hermitian Hamiltonians when two or more eigenstates coalesce [1, 2, 29, 32]. We show that the gain-bandwidth product of the proposed device scales differently from that of standard resonators, which leads to superior performance without requiring any additional control tones. These predictions are confirmed by performing full-wave finite-difference time-domain (FDTD) analysis using realistic microring resonator geometries and material parameters.

6.2 Theoretical analysis

6.2.1 Amplification at diabolic points

To this end, we consider the structure shown in Fig. 6.1. It consists of a microring resonator coupled to two identical waveguides, one of which is terminated by a mirror and the other is used as an input/output port. Optical gain is applied to the ring where the amplification process takes place. In the absence of the mirror, the system has two independent eigenmodes with identical resonant frequencies ω_0: clockwise (CW) and counterclockwise (CCW); i.e. it operates at a diabolic point (DP). Under this condition and by using temporal coupled mode theory (TCMT) [150, 151], we

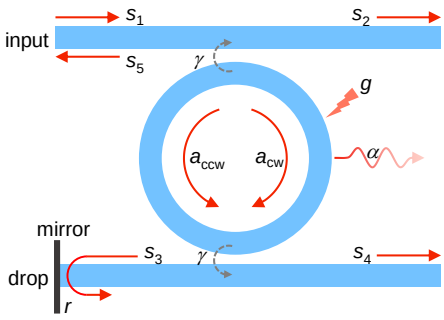

Figure 6.1: Schematic structure of an optical amplifier (OA) based on microring resonator working at an exceptional point (EP). The input s_1 will couple into the microring resonator (coupling rate γ) and be amplified by the pumping gain g. The clockwise mode $a_{\rm cw}$ will couple into counterclockwise mode $a_{\rm ccw}$ while the opposite is not true because of the mirror at the drop port. The output s_5 will be amplified in this process. Here r is the magnitude of the field reflection coefficient of mirror and α is the decay rate due to radiation and material loss.

find the scattering coefficient between the input (s_1) and output (s_3) ports:

$$s_{31} \equiv \frac{s_3}{s_1} = \frac{2\gamma}{i(\omega-\omega_0)+2\gamma+\alpha-g}, \tag{6.1}$$

where α is the decay rate due to loss (radiation and material loss excluding those caused by coupling to the waveguides); γ is the loss rate due to coupling to each of the two waveguides; g is the applied gain rate and ω is the input signal angular frequency. From Eq. (6.1), we obtain the following expressions for maximum power amplification at resonance $G_{\rm DP} \equiv |s_{31}(\omega_0)|^2 = 4\gamma^2/(2\gamma+\alpha-g)^2$, and the bandwidth (in terms of angular frequency): $B_{\rm DP} = 2(2\gamma+\alpha-g)$. The gain-bandwidth product can then be expressed as $\chi_{\rm DP} = \sqrt{G_{\rm DP}}\cdot B_{\rm DP} = 4\gamma$. The subscript DP here emphasizes that these quantities are obtained for an OA operating at a DP.

6.2.2 Amplification at exceptional points

We now investigate the behavior of the same system in the presence of the mirror. We first do so by using the temporal coupled mode theory:

$$\begin{aligned}
\frac{da_{\mathrm{cw}}}{dt} &= [i(\omega_0-\omega)-2\gamma-\alpha+g]a_{\mathrm{cw}}+\sqrt{2\gamma}s_1,\\
\frac{da_{\mathrm{ccw}}}{dt} &= [i(\omega_0-\omega)-2\gamma-\alpha+g]a_{\mathrm{ccw}}+\sqrt{2\gamma}s_3\cdot re^{i\phi},\\
s_3 &= -\sqrt{2\gamma}a_{\mathrm{cw}},\\
s_5 &= -\sqrt{2\gamma}a_{\mathrm{ccw}},
\end{aligned} \tag{6.2}$$

where we consider s_5 to be the output port, a_{cw} and a_{ccw} are the amplitude of the resonator mode in CW and CCW direction, r is the magnitude of the field reflection coefficient of the mirror, and $\exp(i\phi)$ is an additional phase due to reflection and propagation in the waveguide. In the absence of any input signal, the above system is described by the following effective coupled mode equations:

$$i\frac{d}{dt}\begin{bmatrix}a_{\mathrm{cw}}\\ a_{\mathrm{ccw}}\end{bmatrix} = H\begin{bmatrix}a_{\mathrm{cw}}\\ a_{\mathrm{ccw}}\end{bmatrix}, H=\begin{bmatrix}\Omega & 0\\ -2i\gamma re^{i\phi} & \Omega\end{bmatrix}, \tag{6.3}$$

where $\Omega=\omega-\omega_0-i(2\gamma+\alpha-g)$. Interestingly, H is a non-diagonalizable Jordan matrix that features a chiral EP [152], which has also been implemented using nanoscatterers arrangements [19, 38].

Under external driving from port s_1, the scattering coefficient between input and output ports is:

$$s_{51} \equiv \frac{s_5}{s_1} = \frac{4re^{i\phi}\gamma^2}{[i(\omega-\omega_0)+2\gamma+\alpha-g]^2}. \tag{6.4}$$

This solution is valid only below the lasing threshold $g = 2\gamma+\alpha$. Importantly, the scattering coefficient s_{51} exhibits a double pole as compared to the single pole in Eq. (6.1). As we will see shortly, this will have drastic consequences. Under these conditions, the maximum value of the amplification is $G_{\rm EP} \equiv |s_{51}(\omega_0)|^2 = 16r^2\gamma^4/(2\gamma+\alpha-g)^4$. On the other hand, the bandwidth is given by $B_{\rm EP} = 2F(2\gamma+\alpha-g)$ with $F = \sqrt{\sqrt{2}-1} \approx 0.64$. The subscript EP here emphasizes that these quantities are obtained when the system operates at a chiral EP. When comparing these results with those obtained for the DP-based amplifiers, we find that the bandwidth in the current scenario is reduced by a factor of F, while the gain is enhanced according to the quadratic relation $G_{\rm EP} = r^2 G_{\rm DP}^2$. This leads to:

$$\chi_{\rm EP} \equiv G_{\rm EP}^{1/4} \cdot B_{\rm EP} = 4F\sqrt{r}\gamma. \tag{6.5}$$

Equation (6.5) is one of the central results of this work. It shows that the gain-bandwidth product for the EP regime scales differently than for the case of DP. As we will demonstrate below, this provides superior performance over the standard amplifier operating at DP. To facilitate the comparison between the two scenarios (EP vs DP), we set $r \approx 1$, which can be achieved in realistic implementations.

6.2.3 Comparison between amplification at EP and DP

We first consider the case when the two amplifiers based on EP and DP respectively have the same bandwidth. This occurs for different levels of pumpings related by $\tilde{g}_{\mathrm{EP}} = F^{-1}\tilde{g}_{\mathrm{DP}} + 2(1 - F^{-1})$, where $\tilde{g} = (g - \alpha)/\gamma$, and α, γ are identical for both amplifiers but g is different. Under these conditions, the amplification enhancement factor η_G is:

$$\eta_G \equiv \frac{G_{\mathrm{EP}}}{G_{\mathrm{DP}}} = \frac{4F^4}{(2 - \tilde{g}_{\mathrm{DP}})^2}. \tag{6.6}$$

The amplification enhancement for identical bandwidth is plotted in Fig. 6.2(a), together with the pumping relation to achieve identical bandwidth (inset). Above point p (where $\tilde{g}_{\mathrm{DP}} = 2\sqrt{2}F^2 \approx 1.17$), we have $\eta_G > 1$, i.e., the EP-based amplifier outperform the DP one. Notably, the value of the amplification enhancement factor increases rapidly as the two amplifiers approach the lasing condition at $\tilde{g}_{\mathrm{DP}} = \tilde{g}_{\mathrm{EP}} = 2$.

Next, we consider the situation where both amplifiers have the same maximum amplification ($G_{\mathrm{EP}} = G_{\mathrm{DP}}$) but different bandwidth. This condition can be met if $\tilde{g}_{\mathrm{EP}} = 2 - \sqrt{2(2 - \tilde{g}_{\mathrm{DP}})}$. In this case, the bandwidth enhancement factor η_B is given by:

$$\eta_B \equiv \frac{B_{\mathrm{EP}}}{B_{\mathrm{DP}}} = \frac{\sqrt{2}F}{\sqrt{2 - \tilde{g}_{\mathrm{DP}}}}. \tag{6.7}$$

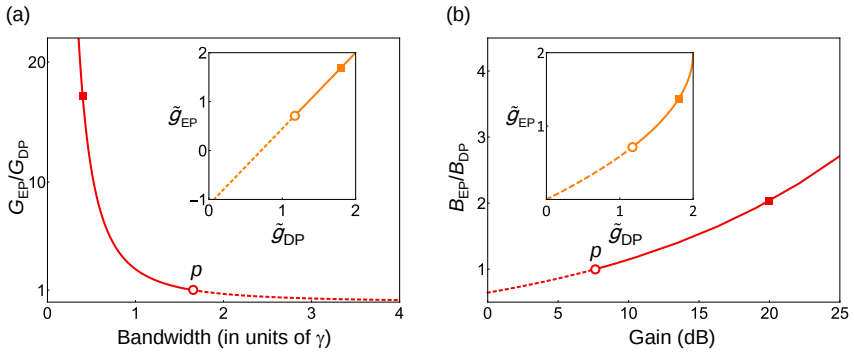

Figure 6.2: (a) Amplification enhancement for EP-based OA (as compared with standard DP-based resonators) as a function of their identical bandwidth as measured in units of γ. (b) Same as in (a) but for bandwidth enhancement as a function of the identical amplification. The insets in (a) and (b) plot the relations between the material gain values that are necessary to achieve identical bandwidth or amplification respectively (see text). Finally, the squares indicate the parameters used in the full wave simulation later.

Figure 6.2(b) depicts η_B for increasing power amplification, together with the pumping relations as a function of $\tilde{g}_{\mathrm{DP}}$. As before, the critical point p (identical to that of Fig. 6.2(a)) divides the operation domain into two regimes with $\eta_B < 1$ (dashed line) and $\eta_B > 1$ (solid line). Similar to the previous case, the value of η_B increases rapidly (eventually diverging) close to the lasing condition $\tilde{g}_{\mathrm{DP}} = \tilde{g}_{\mathrm{EP}} = 2$ (not shown in the figure).

Our discussion clearly demonstrates that operating at an EP can provide superior performance with very large values of η_G or η_B. However, from a practical perspective, the operating point should be chosen sufficiently away from the lasing threshold to avoid noise induced instabilities that can force the system into the lasing regime. Based on the detailed implementation and noise level, this can pose an upper limit

on the enhancement factors.

6.3 Implementation and full-wave analysis

We have so far discussed the operation of our proposed EP-based OAs based on the optical coupled mode theory. In order to confirm these predictions, we explore realistic implementations by performing two-dimensional (2D) full-wave FDTD simulations [120]. Particularly, we study a 2D version of the schematic shown in Fig. 6.3. The geometric and physical parameters are all listed in the figure caption.

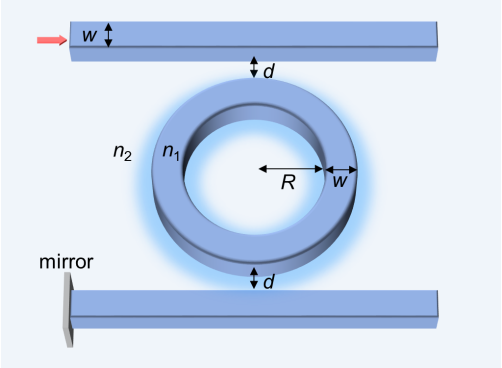

Figure 6.3: A schematic diagram of the proposed photonic structure used in our FDTD simulations. The geometric and material parameters are assumed to be the following: waveguide width $w = 0.25$ μm (for both the straight and the ring waveguides), ring radius $R = 5$ μm, edge-to-edge distances between the ring and waveguides $d = 0.15$ μm. To implement the mirror, we assume a thin layer of silver with a thickness of 100 nm. The material refractive index is $n_1 = 3.47$ (corresponding to semiconductor materials such as silicon or AlGaAs) and the background index is taken to be $n_2 = 1.44$. These values have been used before in DP-based microring amplifiers. Finally, we model the applied gain by considering a gain curve with a finite bandwidth.

The transmission of the passive resonators used in our simulations based on DP or

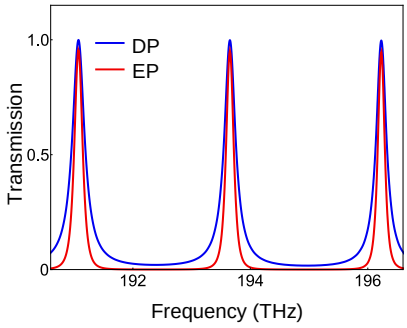

Figure 6.4: The transmission of the DP-based and EP-based resonators without any material gain. Then a material gain based on Lorentz model as discussed in the text was applied to the microring resonator.

EP without any material gain is shown in Fig. 6.4. The operating resonant frequency is located at $f_0 = 193.652$ THz, with free spectral range (FSR) of 2.58 THz. The maximum transmission for the DP-based resonator is 0.998, indicating $\alpha/\gamma = 0.002$, which is a small quantity. The maximum transmission for the EP-based resonator is 0.952, which can be used to deduce the value of reflection coefficient $r^2 = 0.954$ — consistent with the $r^2 = 0.953$ obtained from a direct FDTD simulation test on reflectivity of the mirror.

In our simulations, the applied material gain has a finite bandwidth as expressed by the Lorentz model:

$$\varepsilon(\omega) = \varepsilon_{\mathrm{b}} + \frac{\varepsilon' \omega_0^2}{\omega_0^2 - \omega^2 - 2i\delta\omega}, \tag{6.8}$$

where ε_{b} is the permittivity of background material in the absence of any gain/loss or dispersion; ω_0 is operating resonant frequency of the microring; $\delta = 10^{13}$ rad/s is gain curve linewidth; ε' is a constant. To proceed with the computations, we set the

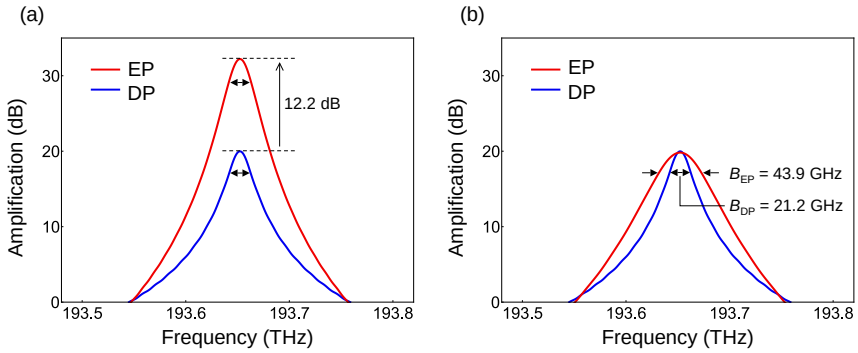

Figure 6.5: Full-wave FDTD simulations for EP and DP-based amplifiers operating close to $\lambda = 1.55$ μm and having (a) identical bandwidth; and (b) identical maximum amplification respectively. The superior performance larger amplification in (a) and bandwidth in (b) is evident in both cases. The operating points of both scenarios correspond to the square dots in Figs. 6.2(a) and (b) correspondingly. Excellent agreement is between the FDTD results and the coupled mode theory is observed in both cases. The details of the design parameters used in our simulations are listed in the text.

value of ε' for every case and use FDTD to calculate the maximum amplification at resonant. This quantity can be then used to obtain the normalized gain values $\tilde{g}_{\rm DP}$ and $\tilde{g}_{\rm EP}$ (see the formulas for $G_{\rm DP}$ and $G_{\rm EP}$), which in turn allows us to compare our FDTD results with Eqs. (6.6) and (6.7).

Figures 6.5(a) and (b) depict the simulation results for the two different scenarios discussed above, i.e. equal bandwidth or equal maximum amplification. The tuning of the amplifiers to operate in either of these regimes is done by setting up the correct gain parameters. Particularly, in the simulations of Fig. 6.5, we used $\varepsilon' = -2.133 \times 10^{-4}$ for the DP amplifier; $\varepsilon' = -2.00194 \times 10^{-4}$ and $\varepsilon' = -1.6198 \times 10^{-4}$ for the EP amplifiers of Figs. 6.5(a) and (b), respectively. As shown in Fig. 6.5(a), for fixed bandwidth of 21.2 GHz, a large amplification enhancement factor is achieved

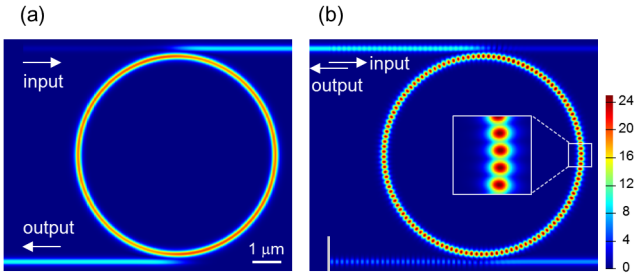

Figure 6.6: Electric field distributions associated with: (a) DP-based, and (b) and EP-based amplifier for the resonant frequency when they both have equal gain (i.e. corresponding to the case of Fig. 6.5 (b)). The inset in (b) highlights the interference pattern between the CW and CCW components in the latter case. The legend colors represent the value if the electric field normalized by the value of the input field.

with $\eta_G = 16.7$, corresponding to 12.2 dB. On the other hand, Fig. 6.5(b) shows that for an equal maximum amplification of 20 dB, the bandwidth in the EP case can be doubled, $\eta_B = 2.1$. These results, which have been obtained by using full-wave FDTD, are consistent with theoretical values predicted by coupled mode theory and clearly indicate the potential utility of the proposed structure.

Finally, Fig. 6.6 plots the field distribution for the two cases of DP and EP amplifiers (corresponding to the structure of Fig. 6.3 without and with the mirror) for the scenario depicted in Fig. 6.5(b) at resonance. In the EP case, one can observe the interference pattern that results in due to the coexistence of CW and CCW waves. Note that minimum of the field (see inset) is not zero, which can be understood by recalling that the CCW component has larger amplitude (due to amplification) than the CW component. This can be also confirmed by inspecting the time evolution of the fields (not shown here).

6.4 Conclusions

The scaling features of the gain-bandwidth products associated with the geometry shown in Fig. 6.1 can be understood intuitively by noting that light traverses the ring twice in the forward and backward directions, which explains gain enhancement. This observation raises the question of whether one can achieve the same performance by concatenating two ring resonators. As we discuss in Appendix 6A, this is indeed possible and gives exactly the same results. Interestingly, even in this latter case, one can show that the system exhibits a second-order EP, though an unusual one (see Appendix 6A for detailed discussion). This provides an advantage in terms of scalability since one can add more microrings to obtain even higher order poles with far more superior performance. However, from a practical perspective, this latter design (with concatenated rings) will be more prone to fabrication errors (all the different ring parameters have to exactly match) and will require more complex pumping scheme. This is in contrast to the design of Fig. 6.1 which does not suffer from these problems.

Another possible implementation that can combine the enhanced performance with the robustness is the S-bend ring resonator, which is also known to provide unidirectional coupling [153, 154, 155]. As shown in Appendix 6B, the output power demonstrates similar scaling behavior with that of EP-based OAs with a mirror.

In conclusion, we have introduced a new design paradigm for optical amplifiers based on chiral exceptional points. An important feature of the proposed structure is the unique scaling of its gain-bandwidth product which is different from standard amplifiers, and allows for achieving more gain or larger bandwidth of operation. Mathematically, these results can be understood by noting that operating at an EP results in a double pole in the scattering coefficients (as opposed to a single pole in the standard DP case). Importantly, we have explored realistic implementations using current photonics technology to implement these amplifiers based on chiral exceptional points (for completeness, we have also confirmed these conclusions for parity-time-(PT-)based EP in Appendix 6C).

6.5 Appendix

Appendix 6A: Cascaded amplifiers and exceptional points

In the EP-based amplifier proposed in Fig. 6.1, light travels from port s_1 to s_3, gets reflected and travels back to the same input port in the opposite direction. This intuitive picture can explain the enhacement in the net amplification. It also raises the question of whether it is possible to achieve the same functionality by concatenating two ring resonators. By referring to Fig. 6.7(a), it is not difficult to see that this

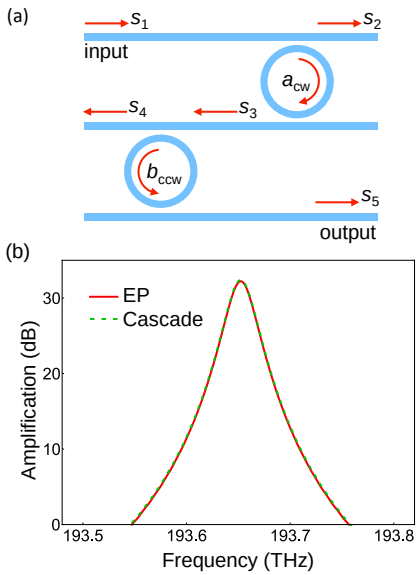

Figure 6.7: (a) A cascaded amplifier can achieve the same functionality as the structure in Fig. 1 with $r\exp(i\phi) = 1$, as confirmed in (b) using FDTD.

structure has identical scattering coefficient to that of Fig. 6.1 with $r\exp(i\phi) = 1$. This is also confirmed by using FDTD with $\varepsilon' = -2.00194 \times 10^{-4}$, as shown in Fig. 6.7(b).

At first sight, this may seem surprising but interestingly, the system in Fig. 6.7 also has a chiral EP since mode a_{cw} couples to b_{ccw} while the opposite is not true. In fact, here there is also another chiral EP arising from the unidirectional coupling from b_{cw} to a_{ccw}, which would allow the amplifier to work for backward propagating light as well. Interestingly, this scheme can be used to build amplifiers with higher order EPs by just cascading as many rings as needed, thus provides a clear advantage in terms of scalability. In practice, however, this system will be more prone to fabrication errors since it will require all the rings to have identical parameters within a small margin of

error (disorder in the coupling parameters will not affect the chiral EP). Additionally, it will also require a complex pumping scheme and more power consumption to provide gain to all the rings. On the other hand, the structure proposed in Fig. 6.1 does not suffer from these problems. Particularly, any variation in the ring parameter will affect both modes equally which will shift the central frequency but retain the same gain-bandwidth relation. Additionally, it contains only one ring and thus requires simpler pumping and less power consumption.

6.5.1 Appendix 6B: S-bend ring resonator

Another possible implementation that can combine the enhanced performance with the robustness is the S-bend ring resonator shown in Fig. 6.8. This structure is also known to provide unidirectional coupling [153, 154, 155]. By using the scattering matrices $S_j = \begin{bmatrix} t_j & i\kappa_j \\ i\kappa_j & t_j \end{bmatrix}$ (with $t_j^2 + \kappa_j^2 = 1$, where $j = 1, 2, 3, 4$) at each junction (denoted by the dashed black lines in Fig. 6.8), we obtain the relation between the electric field amplitudes a_{cw} and a_{ccw} at the beginning and end of each section along the ring between any two junctions. This, in turn, can be used to calculate the scattering coefficients. Particularly, when $S_2 = S_4$ and $S_3 = I$, where I is the unit

matrix (i.e. remove the lower waveguide altogether), we obtain

$$u_{51} \equiv \frac{u_5}{u_1} = \frac{2\Gamma t_2 \kappa_1^2 \kappa_2^2 \exp(i\omega\tau)}{[1 - \Gamma t_1 t_2^2 \exp(i\omega\tau)]^2}, \tag{6.9}$$

where $\Gamma = \exp[-2\pi \mathrm{Im}(n_{\mathrm{eff}})L/\lambda]$ is the round trip gain of ring resonator, and $\tau = \mathrm{Re}(n_{\mathrm{eff}})L/c$. Here n_{eff} is the effective index of ring waveguide mode, L is the circumference of the ring waveguide and λ is the free space wavelength. The maximum amplification (at resonant frequency) and the bandwidth are then found to be:

$$\begin{aligned} G_{\mathrm{S}} &= \frac{4\Gamma^2 t_2^2 \kappa_1^4 \kappa_2^4}{(1 - \Gamma t_1 t_2^2)^4}, \\ B_{\mathrm{S}} &= 2F \frac{1 - \Gamma t_1 t_2^2}{\sqrt{\Gamma t_1} t_2} \tau^{-1}. \end{aligned} \tag{6.10}$$

Consequently, the gain-bandwidth product is given by:

$$\chi_{\mathrm{S}} \equiv G_{\mathrm{S}}^{1/4} \cdot B_{\mathrm{S}} = 2\sqrt{2} F \kappa_1 \kappa_2 t_1^{-1/2} \tau^{-1}, \tag{6.11}$$

with the right hand side being a constant. This last expression reveals that the gain-bandwidth product in the S-bend geometry scales in a similar fashion to the structure shown in Fig. 6.1. From an experimental perspective, one can add the second waveguide and measure the output from u_4, where it can be shown that the output power demonstrates similar scaling behavior.

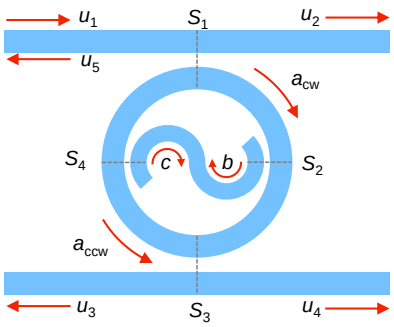

Figure 6.8: The S-bend ring can provide a unidirectional coupling between CW and CCW mode. This structure is studied with scattering matrices S_j $(j = 1, 2, 3, 4)$ in the four coupling regions (dashed lines).

Appendix 6C: Amplifiers at EPs in PT symmetric dimers

In order to make the connection between our results here and the work on PT symmetry; and at the same time illustrate that the predicted superior performance of EP-based amplifiers is general and not restricted to the geometry investigated in the main text, we consider an amplifier based on the archetypal PT symmetric dimer [1, 2, 7, 8, 9, 11, 12, 52, 156] shown in Fig. 6.9(a). It consists of two identical microrings coupling with each other with coupling rate κ. Both rings have the same radiation loss and coupled to identical waveguides with equal coupling coefficients. Additionally, we assume that the top ring has a material gain g while the lower ring

has an additional loss factor $-g$. By using TCMT, we obtain:

$$\begin{aligned}
\frac{da_{\mathrm{cw}}}{dt} &= [i(\omega_0-\omega)-\gamma-\alpha+g]a_{\mathrm{cw}} + i\kappa b_{\mathrm{ccw}} + \sqrt{2\gamma}s_1, \\
\frac{db_{\mathrm{ccw}}}{dt} &= [i(\omega_0-\omega)-\gamma-\alpha-g]a_{\mathrm{ccw}} + i\kappa a_{\mathrm{cw}}, \\
s_3 &= -\sqrt{2\gamma}b_{\mathrm{ccw}}.
\end{aligned} \tag{6.12}$$

By solving the above system, we obtain the expression for the steady state transfer function:

$$s_{31} \equiv \frac{s_3}{s_1} = \frac{-2ig\gamma}{i[(\omega-\omega_0)+\gamma+\alpha]^2+\kappa^2-g^2}. \tag{6.13}$$

Note that this solution is valid only below the lasing threshold $g^2 = \kappa^2+(\gamma+\alpha)^2$. The system exhibits an EP when $g = \kappa$. Under this condition, the maximum amplification is given by $G_{\mathrm{PT}} = 4g^2\gamma^2/(\gamma+\alpha)^4$ while the bandwidth take the value $B_{\mathrm{PT}} = 2F(\gamma+\alpha)$. Interestingly, in contrasts to the structure investigated in the main text, here the bandwidth is independent of the gain. In other words, the gain-bandwidth product can be made arbitrary large by judicious choice of the design parameters and the applied gain — a feature that was previously noted for linear microwave amplifiers based on wave mixing processes [145, 157], though without establishing the connection with the physics of exceptional points. To illustrate this point, Figure 6.9(b) depicts a comparison between the three different structures of Fig. 6.1 (with and without a mirror) and Fig. 6.9(a). Here we choose $\alpha \approx 0$ and identical γ for all three

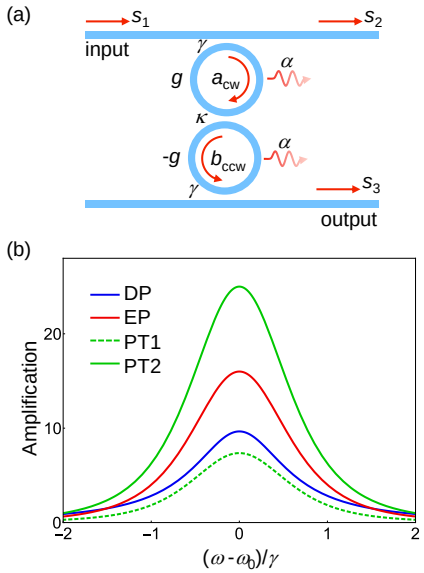

Figure 6.9: (a) A PT dimer based optical amplifier having an exceptional point at $g = \kappa$. (b) Comparison between the strcuture in (a) and those in Fig. 6.1 (with and without a mirror) for identical γ and assuming $\alpha = 0$, when $g_{\mathrm{PT1}} = 1.36\gamma$ (dashed green line) and $g_{\mathrm{PT2}} = 2.5\gamma$ (solid green line). Clearly, one can increase the amplification of the PT amplifier while at the same time maintain the same bandwidth. From a practical perspective however, increasing the amplification requires stronger coupling κ (i.e. smaller separation between the two rings) which is limited by the fabrication tolerance.

devices. The bandwidth of PT-based amplifier is $2F\gamma \approx 1.28\gamma$. This same bandwidth can be achieved for the other two geometries by setting $g_{\mathrm{DP}} = (2 - F)\gamma \approx 1.36\gamma$ and $g_{\mathrm{EP}} = \gamma$. When $g_{\mathrm{PT}} = g_{\mathrm{DP}}$, the PT system exhibits lower amplification as shown by the dashed green line in Fig. 6.9(b). However, in theory, the maximum amplification can be increased indefinitely by increasing g_{PT} without affecting the bandwidth. For example, by choosing $g_{\mathrm{PT}} = 2.5\gamma$, the maximum amplification of the PT structure can significantly surpass that of the other two scenarios while at the same time maintaining the same bandwidth (solid green line in Fig. 6.9(b)).

From a practical perspective however, increasing the gain bandwidth product will require fabricating samples with stronger coupling between the two rings which is obviously limited by the minimum achievable edge-to-edge separation between the rings. Additionally, the PT geometry is very sensitive to fabrication errors and tolerance as well as uncertainties in the operating conditions such as thermal effects for instance.

Chapter 7

Summary

First, we have investigated the maximum possible amplification scales with the power of the order of the EPs N in the PT phase. Our results provide a valuable insight into the generic behavior near EPs which may help direct future research in this field. In addition, our work opens up a new set of intriguing questions that merit future investigations. For example, do systems having higher order EPs exhibit the same dynamics locally close to the EPs? In such a case, the power law dependency discovered here would be universal. However, it is also possible that Hamiltonians that do not have the form of H_N behaves differently. We note however that, to date, Hamiltonians of the form H_N are the only systematic approach to realize arbitrarily higher order EPs in discrete arrangements. Another interesting question is how

nonlinear interactions come into play when the amplification leads to large intensities that trigger various nonlinear effects? One of the very important directions with practical consequences is the problem of laser linewidth near EPs. Whereas a direct extrapolation from the original work of Petermann [33] predicts a divergent linewidth at EPs, recent analysis by Yoo et al. [53] demonstrated that the linewidth enhancement is finite. Our work here provides an intuitive framework for understanding the amplification of noise near EPs and hints that the even larger enhancement factors should be expected near higher order EPs. It would be of interest to fully develop this link either by using similar analysis to that of [53] or other statistical methods [158].

Then, by introducing the concept of PT phase diagram, we revisited the PT phase transition across EPs and demonstrated that crossing an EP in the parameter space does not necessarily lead to phase transition. Our work provides a new twist and a deeper understanding for the physics of non-Hermitian systems near EPs, with potential implication in various fields such as photonics [2], acoustics [66, 159] and electronics [22, 108, 160]. Particularly, the recent important work on driving Floquet PT symmetric systems offer a natural platform for confirming our predictions experimentally [161].

In Chapter 4, the stroboscopic encircling EPs problem was studied and a general formalism based on permutation groups and representation theory was introduced. We

have shown that trajectories that enclose the same EPs starting from the same parameters and traveling in the same direction, do not necessarily result in an identical exchange between the states. Instead, this equivalence can be established by invoking the topological notion of homotopy. Our work may find applications in various fields including the recent interesting work on the relationship between exceptional points and topological edge states[162, 163]. Finally, we would like to comment on potential experimental platforms that can be used to observe the effects discussed here. In principle, any non-Hermitian system where the Hamiltonian parameters can be controlled is a good candidate.

In Chapter 5 and 6, we proposed a new design paradigm for sensors and optical amplifiers that operate at exceptional surfaces as opposed to isolated exceptional points. This new paradigm provides more degrees of freedom that can be exploited to combine a certain degree of robustness against fabrication tolerance together with the enhanced sensitivity associated with exceptional points. In the application of optical amplifiers, the proposed structure provides unique scaling of its gain-bandwidth product which is different from standard amplifiers, and allows for achieving more gain or larger bandwidth of operation. Our results open the door for building a new generation of on-chip optical devices with superior performance, which can prove beneficial for both classical and quantum optics applications. Finally, we emphasize that our proposed scheme can be directly mapped into other physical systems such as microwaves and acoustics.

References

[1] El-Ganainy, R.; Makris, K. G.; Khajavikhan, M.; Musslimani, Z. H.; Rotter, S.; Christodoulides, D. N. *Nat. Phys.* **2018**, *14*, 11.

[2] Feng, L.; El-Ganainy, R.; Ge, L. *Nat. Photon.* **2017**, *11*(12), 752–762.

[3] Özdemir, Ş. K.; Rotter, S.; Nori, F.; Yang, L. *Nature Materials* **2019**.

[4] Miri, M.-A.; Alú, A. *Science* **2019**, *363*(6422), eaar7709.

[5] Bender, C. M.; Boettcher, S. *Phys. Rev. Lett.* **1998**, *80*(24), 5243–5246.

[6] El-Ganainy, R.; Khajavikhan, M.; Christodoulides, D. N.; Özdemir, Ş. K. *Communications Physics* **2019**, *2*(1), 37.

[7] El-Ganainy, R.; Makris, K. G.; Christodoulides, D. N.; Musslimani, Z. H. *Opt. Lett.* **2007**, *32*(17), 2632–2634.

[8] Ruter, C. E.; Makris, K. G.; El-Ganainy, R.; Christodoulides, D. N.; Segev, M.; Kip, D. *Nat. Phys.* **2010**, *6*(3), 192–195.

[9] Guo, A.; Salamo, G. J.; Duchesne, D.; Morandotti, R.; Volatier-Ravat, M.; Aimez, V.; Siviloglou, G. A.; Christodoulides, D. N. *Phys. Rev. Lett.* **2009**, *103*(9), 093902.

[10] Ramezani, H.; Kottos, T.; El-Ganainy, R.; Christodoulides, D. N. *Phys. Rev. A* **2010**, *82*, 043803.

[11] Peng, B.; Özdemir, S. K.; Lei, F.; Monifi, F.; Gianfreda, M.; Long, G. L.; Fan, S.; Nori, F.; Bender, C. M.; Yang, L. *Nat. Phys.* **2014**, *10*(5), 394–398.

[12] Hodaei, H.; Miri, M.-A.; Heinrich, M.; Christodoulides, D. N.; Khajavikhan, M. *Science* **2014**, *346*(6212), 975–978.

[13] Feng, L.; Wong, Z. J.; Ma, R.-M.; Wang, Y.; Zhang, X. *Science* **2014**, *346*(6212), 972–975.

[14] Needham, T. *Visual Complex Analysis;* Clarendon Press, 1998.

[15] Musslimani, Z. H.; Makris, K. G.; El-Ganainy, R.; Christodoulides, D. N. *Phys. Rev. Lett.* **2008**, *100*(3), 030402.

[16] Makris, K. G.; El-Ganainy, R.; Christodoulides, D. N.; Musslimani, Z. H. *Phys. Rev. Lett.* **2008**, *100*(10), 103904.

[17] El-Ganainy, R.; Ge, L.; Khajavikhan, M.; Christodoulides, D. N. *Phys. Rev. A* **2015**, *92*(3), 033818.

[18] Teimourpour, M. H.; Ge, L.; Christodoulides, D. N.; El-Ganainy, R. *Sci. Rep.* **2016**, *6*, 33253.

[19] Wiersig, J. *Phys. Rev. Lett.* **2014**, *112*(20), 203901.

[20] Hodaei, H.; Hassan, A. U.; Wittek, S.; Garcia-Gracia, H.; El-Ganainy, R.; Christodoulides, D. N.; Khajavikhan, M. *Nature* **2017**, *548*(7666), 187–191.

[21] Chen, W.; Özdemir, Ş. K.; Zhao, G.; Wiersig, J.; Yang, L. *Nature* **2017**, *548*(7666), 192–196.

[22] Lin, Z.; Ramezani, H.; Eichelkraut, T.; Kottos, T.; Cao, H.; Christodoulides, D. N. *Phys. Rev. Lett.* **2011**, *106*, 213901.

[23] Zhu, X.; Feng, L.; Zhang, P.; Yin, X.; Zhang, X. *Opt. Lett.* **2013**, *38*, 2821–2824.

[24] El-Ganainy, R.; Dadap, J. I.; Osgood, R. M. *Opt. Lett.* **2015**, *40*(21), 5086–5089.

[25] Zhong, Q.; Ahmed, A.; Dadap, J. I.; Osgood, R. M.; El-Ganainy, R. *New J. Phys.* **2016**, *18*(12), 125006.

[26] Sakurai, J. J.; Napolitano, J. J. *Modern Quantum Mechanics;* Pearson, 2nd ed., 2010.

[27] Heiss, W. D.; Sannino, A. L. *J. Phys. A* **1990**, *23*(7), 1167.

[28] Magunov, A. I.; Rotter, I.; Strakhova, S. I. *J. Phys. B* **1999**, *32*(7), 1669.

[29] Heiss, W. D. *J. Phys. A* **2004**, *37*(6), 2455.

[30] Heiss, W. D. *J. Phys. A* **2012**, *45*(44), 444016.

[31] Rotter, I. *Phys. Rev. E* **2003**, *67*(2), 026204.

[32] Müller, M.; Rotter, I. *J. Phys. A* **2008**, *41*(24), 244018.

[33] Petermann, K. *IEEE J. Quantum Electron.* **1979**, *15*(7), 566–570.

[34] Siegman, A. E. *Phys. Rev. A* **1989**, *39*(3), 1253–1263.

[35] New, G. H. C. *J. Mod. Opt.* **1995**, *42*(4), 799–810.

[36] Berry, M. V. *J. Mod. Opt.* **2003**, *50*(1), 63–81.

[37] Lee, S.-Y.; Ryu, J.-W.; Shim, J.-B.; Lee, S.-B.; Kim, S. W.; An, K. *Phys. Rev. A* **2008**, *78*(1), 015805.

[38] Wiersig, J. *Phys. Rev. A* **2016**, *93*(3), 033809.

[39] Graefe, E. M.; Gunther, U.; Korsch, H. J.; Niederle, A. E. *J. Phys. A* **2008**, *41*(25), 255206.

[40] Gilles, D.; Eva-Maria, G. *J. Phys. A* **2012**, *45*(2), 025303.

[41] Teimourpour, M. H.; El-Ganainy, R.; Eisfeld, A.; Szameit, A.; Christodoulides, D. N. *Phys. Rev. A* **2014**, *90*(5), 053817.

[42] Heiss, W. D.; Wunner, G. *J. Phys. A* **2015**, *48*(34), 345203.

[43] Lin, Z.; Pick, A.; Lončar, M.; Rodriguez, A. W. *Phys. Rev. Lett.* **2016**, *117*, 107402.

[44] Heiss, W. D.; Wunner, G. *J. Phys. A* **2016**, *49*(49), 495303.

[45] Jing, H.; Özdemir, S. K.; Lü, H.; Nori, F. *Sci. Rep.* **2017**, *7*(1), 3386.

[46] Ding, K.; Ma, G.; Xiao, M.; Zhang, Z. Q.; Chan, C. T. *Phys. Rev. X* **2016**, *6*, 021007.

[47] Heiss, W. D. *Eur. Phys. J. D* **2010**, *60*(2), 257–261.

[48] Makris, K. G.; Ge, L.; Türeci, H. E. *Phys. Rev. X* **2014**, *4*, 041044.

[49] Bender, C. M.; Boettcher, S.; Meisinger, P. N. *J. Math. Phys.* **1999**, *40*(5), 2201–2229.

[50] Chong, Y. D.; Ge, L.; Cao, H.; Stone, A. D. *Phys. Rev. Lett.* **2010**, *105*, 053901.

[51] Longhi, S. *Phys. Rev. A* **2010**, *82*, 031801.

[52] Schindler, J.; Li, A.; Zheng, M. C.; Ellis, F. M.; Kottos, T. *Phys. Rev. A* **2011**, *84*, 040101.

[53] Yoo, G.; Sim, H.-S.; Schomerus, H. *Phys. Rev. A* **2011**, *84*, 063833.

[54] Regensburger, A.; Bersch, C.; Miri, M.-A.; Onishchukov, G.; Christodoulides, D. N.; Peschel, U. *Nature* **2012**, *488*, 167.

[55] Chang, L.; Jiang, X.; Hua, S.; Yang, C.; Wen, J.; Jiang, L.; Li, G.; Wang, G.; Xiao, M. *Nat. Photon.* **2014**, *8*, 524.

[56] Jing, H.; Özdemir, S. K.; Lü, X.-Y.; Zhang, J.; Yang, L.; Nori, F. *Phys. Rev. Lett.* **2014**, *113*(5), 053604.

[57] Makris, K.; Musslimani, Z.; Christodoulides, D. N.; Rotter, S. *Nat. Commun.* **2015**, *6*, 7257.

[58] Ge, L.; Makris, K. G.; Christodoulides, D. N.; Feng, L. *Phys. Rev. A* **2015**, *92*, 062135.

[59] Gutiérrez, O. I. Z.; Mendoza, L. F. S.; Rodríguez-Lara, B. M. *Opt. Express* **2016**, *24*(4), 3989–3998.

[60] Scharnhorst, K. *Acta Appl. Math.* **2001**, *69*(1), 95–103.

[61] Galantai, A.; Hegedus, C. J. *Numer. Linear Algebra Appl.* **2006**, *13*(7), 589–598.

[62] Jin, L.; Song, Z. *Phys. Rev. A* **2009**, *80*(5), 052107.

[63] Zhang, X. Z.; Jin, L.; Song, Z. *Phys. Rev. A* **2013**, *87*(4), 042118.

[64] Longhi, S. *Phys. Rev. A* **2013**, *88*.

[65] Bender, C. M.; Gianfreda, M.; Ozdemir, S. K.; Peng, B.; Yang, L. *Phys. Rev. A* **2013**, *88*(6), 062111.

[66] Fleury, R.; Sounas, D.; Alú, A. *Nat. Comm.* **2015**, *6*, 5905.

[67] Arkinstall, J.; Teimourpour, M. H.; Feng, L.; El-Ganainy, R.; Schomerus, H. *Phys. Rev. B* **2017**, *95*(16), 165109.

[68] Gilles, D.; Eva-Maria, G. *J. Phys. A* **2012**, *45*(2), 025303.

[69] Teimourpour, M. H.; Zhong, Q.; Khajavikhan, M.; El-Ganainy, R. In *Parity-time Symmetry and Its Applications*; Christodoulides, D., Yang, J., Eds.; Springer Singapore: Singapore, 2018; pages 261–275.

[70] Trefethen, L.; Embree, M.; Embree, M. *Spectra and Pseudospectra: The Behavior of Nonnormal Matrices and Operators;* Princeton University Press, 2005.

[71] Zhen, B.; Hsu, C. W.; Igarashi, Y.; Lu, L.; Kaminer, I.; Pick, A.; Chua, S.-L.; Joannopoulos, J. D.; Soljačić, M. *Nature* **2015**, *525*, 354.

[72] Dembowski, C.; Gräf, H. D.; Harney, H. L.; Heine, A.; Heiss, W. D.; Rehfeld, H.; Richter, A. *Phys. Rev. Lett.* **2001**, *86*(5), 787–790.

[73] Dietz, B.; Harney, H. L.; Kirillov, O. N.; Miski-Oglu, M.; Richter, A.; Schäfer, F. *Phys. Rev. Lett.* **2011**, *106*(15), 150403.

[74] Gao, T.; Estrecho, E.; Bliokh, K. Y.; Liew, T. C. H.; Fraser, M. D.; Brodbeck, S.; Kamp, M.; Schneider, C.; Höfling, S.; Yamamoto, Y.; Nori, F.; Kivshar, Y. S.; Truscott, A. G.; Dall, R. G.; Ostrovskaya, E. A. *Nature* **2015**, *526*, 554.

[75] Uzdin, R.; Mailybaev, A.; Moiseyev, N. *J. Phys. A* **2011**, *44*(43), 435302.

[76] Berry, M. V.; Uzdin, R. *J. Phys. A* **2011**, *44*(43), 435303.

[77] Hassan, A. U.; Zhen, B.; Soljačić, M.; Khajavikhan, M.; Christodoulides, D. N. *Phys. Rev. Lett.* **2017**, *118*(9), 093002.

[78] Doppler, J.; Mailybaev, A. A.; Bohm, J.; Kuhl, U.; Girschik, A.; Libisch, F.; Milburn, T. J.; Rabl, P.; Moiseyev, N.; Rotter, S. *Nature* **2016**, *537*(7618), 76–79.

[79] Xu, H.; Mason, D.; Jiang, L.; Harris, J. G. E. *Nature* **2016**, *537*(7618), 80–83.

[80] Kühner, T. D.; Monien, H. *Phys. Rev. B* **1998**, *58*(22), R14741–R14744.

[81] Greiner, M.; Mandel, O.; Esslinger, T.; Hänsch, T. W.; Bloch, I. *Nature* **2002**, *415*, 39.

[82] Kühner, T. D.; White, S. R.; Monien, H. *Phys. Rev. B* **2000**, *61*(18), 12474–12489.

[83] Browne, J. *Grassmann Algebra. Exploring applications of extended vector algebra with Mathematica;* CreateSpace Independent Publishing Platform, web draft ed., 2001.

[84] Ablowiz, M. J.; Fokas, A. S. *Complex Variables;* Cambridge University Press: Cambridge, 2003.

[85] Heiss, W. D. *Eur. Phys. J. D* **1999**, *7*(1), 1–4.

[86] Cartarius, H.; Main, J.; Wunner, G. *Phys. Rev. Lett.* **2007**, *99*(17), 173003.

[87] Mailybaev, A. A.; Kirillov, O. N.; Seyranian, A. P. *Phys. Rev. A* **2005**, *72*(1), 014104.

[88] Dembowski, C.; Dietz, B.; Gräf, H. D.; Harney, H. L.; Heine, A.; Heiss, W. D.; Richter, A. *Phys. Rev. E* **2004**, *69*(5), 056216.

[89] Nesterov, A. I.; Ovchinnikov, S. G. *Phys. Rev. E* **2008**, *78*(1), 015202.

[90] Mehri-Dehnavi, H.; Mostafazadeh, A. *J. Math. Phys.* **2008**, *49*(8), 082105.

[91] Berry, M. V. *J. Opt.* **2011**, *13*(11), 115701.

[92] Ryu, J.-W.; Lee, S.-Y.; Kim, S. W. *Phys. Rev. A* **2012**, *85*(4), 042101.

[93] Hassani, S. *Mathematical Physics: A Modern Introduction to Its Foundations;* Springer: New York, 2013.

[94] Brualdi, R. A. *Combinatorial Matrix Classes;* Cambridge University Press: Cambridge, 2006.

[95] Hatcher, A. *Algebraic Topology;* Cambridge University Press: Cambridge, 2002.

[96] Schnabel, J.; Cartarius, H.; Main, J.; Wunner, G.; Heiss, W. D. *Phys. Rev. A* **2017**, *95*(5), 053868.

[97] Choi, Y.; Hahn, C.; Yoon, J. W.; Song, S. H.; Berini, P. *Nat. Commun.* **2017**, *8*, 14154.

[98] Yoon, J. W.; Choi, Y.; Hahn, C.; Yang, K. Y.; Lee, J. Y.; Kim, G.; Hong, J. K.; Ryu, Y.; Song, S. H.; Berini, P. Vol. 10549, 2018.

[99] Brandstetter, M.; Liertzer, M.; Deutsch, C.; Klang, P.; Schöberl, J.; Türeci, H. E.; Strasser, G.; Unterrainer, K.; Rotter, S. *Nat. Commun.* **2014**, *5*, 4034.

[100] Liertzer, M.; Ge, L.; Cerjan, A.; Stone, A. D.; Türeci, H. E.; Rotter, S. *Phys. Rev. Lett.* **2012**, *108*(17), 173901.

[101] Zhong, Q.; Christodoulides, D. N.; Khajavikhan, M.; Makris, K. G.; El-Ganainy, R. *Phys. Rev. A* **2018**, *97*(2), 020105.

[102] Ambichl, P.; Makris, K. G.; Ge, L.; Chong, Y.; Stone, A. D.; Rotter, S. *Phys. Rev. X* **2013**, *3*(4), 041030.

[103] Castaldi, G.; Savoia, S.; Galdi, V.; Alù, A.; Engheta, N. *Phys. Rev. Lett.* **2013**, *110*(17), 173901.

[104] Rivet, E.; Brandstotter, A.; Makris, K. G.; Lissek, H.; Rotter, S.; Fleury, R. *Nat. Phys.* **2018**, *14*(9), 942–947.

[105] Zhang, J.; Peng, B.; Özdemir, Ş. K.; Pichler, K.; Krimer, D. O.; Zhao, G.; Nori, F.; Liu, Y.-x.; Rotter, S.; Yang, L. *Nat. Photon.* **2018**, *12*(8), 479–484.

[106] Feng, L.; Xu, Y.-L.; Fegadolli, W. S.; Lu, M.-H.; Oliveira, J. E. B.; Almeida, V. R.; Chen, Y.-F.; Scherer, A. *Nat. Mater.* **2012**, *12*, 108.

[107] Longhi, S. *Phys. Rev. Lett.* **2009**, *103*, 123601.

[108] Chen, P.-Y.; Sakhdari, M.; Hajizadegan, M.; Cui, Q.; Cheng, M. M.-C.; El-Ganainy, R.; Alú, A. *Nat. Electron.* **2018**, *1*(5), 297–304.

[109] Wiersig, J. *Phys. Rev. A* **2011**, *84*(6), 063828.

[110] Kippenberg, T. J.; Spillane, S. M.; Vahala, K. J. *Opt. Lett.* **2002**, *27*(19), 1669–1671.

[111] Kippenberg, T. J.; Tchebotareva, A. L.; Kalkman, J.; Polman, A.; Vahala, K. J. *Phys. Rev. Lett.* **2009**, *103*(2), 027406.

[112] He, L.; Özdemir, Ş. K.; Zhu, J.; Yang, L. *Phys. Rev. A* **2010**, *82*(5), 053810.

[113] Kim, W.; Özdemir, Ş. K.; Zhu, J.; Monifi, F.; Coban, C.; Yang, L. *Opt. Express* **2012**, *20*(28), 29426–29446.

[114] Zhu, J.; Özdemir, Ş. K.; Xiao, Y.-F.; Li, L.; He, L.; Chen, D.-R.; Yang, L. *Nat. Photon.* **2010**, *4*, 46.

[115] Özdemir, Ş. K.; Zhu, J.; Yang, X.; Peng, B.; Yilmaz, H.; He, L.; Monifi, F.; Huang, S. H.; Long, G. L.; Yang, L. *Proc. Natl. Acad. Sci. U.S.A.* **2014**, *111*(37), E3836–E3844.

[116] Foreman, M. R.; Swaim, J. D.; Vollmer, F. *Adv. Opt. Photonics* **2015**, *7*(2), 168–240.

[117] Yariv, A. *Electron. Lett.* **2000**, *36*(4), 321–322.

[118] Van, V. *Optical Microring Resonators: Theory, Techniques, and Applications;* CRC Press: Boca Raton, Florida, first ed., 2017.

[119] Saleh, B. E. A.; Teich, M. C. *Fundamentals of Photonics;* Wiley: Hoboken, New Jersey, second ed., 2007.

[120] Taflove, A.; Hagness, S. C. *Computational Electrodynamics: The Finite-Difference Time-Domain Method;* Artech House: Boston, London, third ed., 2005.

[121] Zhu, J.; Ozdemir, S. K.; He, L.; Yang, L. *Opt. Express* **2010**, *18*(23), 23535.

[122] Wolff, C.; Tserkezis, C.; Mortensen, N. A. *Nanophotonics* **2019**, page 0036.

[123] Lau, H.-K.; Clerk, A. A. *Nat. Commun.* **2018**, *9*(1), 4320.

[124] Zhou, H.; Lee, J. Y.; Liu, S.; Zhen, B. *Optica* **2019**, *6*(2), 190–193.

[125] Mundbrod, M. *Annual Report 2003, Optoelectronics Department, University of Ulm* **2003**.

[126] Chen, Q.; Zhou, X.; Wang, Y.; Huang, Q.; Chen, X.; Jiang, W. In *International Conference on Optical Instruments and Technology 2017*, Vol. 10622, page 8. SPIE, 2017.

[127] Kaminow, I.; Eisenstein, G.; Stulz, L. *IEEE J. Quantum Electron.* **1983**, *19*(4), 493–495.

[128] Stadler, B. J. H.; Mizumoto, T. *IEEE Photonics Journal* **2014**, *6*(1), 1–15.

[129] Ye, D.; Cao, C.; Zhou, T.; Huangfu, J.; Zheng, G.; Ran, L. *Nat. Commun.* **2017**, *8*(1), 51.

[130] Little, B. E.; Laine, J.-P.; Chu, S. T. *Opt. Lett.* **1997**, *22*(1), 4–6.

[131] Wiersig, J.; Kim, S. W.; Hentschel, M. *Phys. Rev. A* **2008**, *78*(5), 053809.

[132] Maker, A. J.; Armani, A. M. *J. Vis. Exp.* **2012**, (65), e4164.

[133] Lee, M. M.; Yao, J.; Wu, M. C. In *18th IEEE International Conference on Micro Electro Mechanical Systems, 2005. MEMS 2005.*, pages 596–599, 2005.

[134] Ji, X.; Barbosa, F. A. S.; Roberts, S. P.; Dutt, A.; Cardenas, J.; Okawachi, Y.; Bryant, A.; Gaeta, A. L.; Lipson, M. *Optica* **2017**, *4*(6), 619–624.

[135] Kippenberg, T. J. *Nat. Photon.* **2010**, *4*, 9.

[136] Yariv, A. *IEEE Photonics Technol. Lett.* **2002**, *14*(4), 483–485.

[137] Johnson, S. G.; Ibanescu, M.; Skorobogatiy, M. A.; Weisberg, O.; Joannopoulos, J. D.; Fink, Y. *Phys. Rev. E* **2002**, *65*, 066611.

[138] Zhu, J.; Zhong, Y.; Liu, H. *Photon. Res.* **2017**, *5*(5), 396–405.

[139] Toyoda, T.; Yabe, M. *J. Phys. D* **1983**, *16*(5), L97.

[140] Dutta, N. K.; Wang, Q. *Semiconductor Optical Amplifiers*, Semiconductor Optical Amplifiers; World Scientific, 2nd ed., 2013.

[141] Connelly, M. *Semiconductor Optical Amplifiers;* Springer, 2013.

[142] Hattori, K.; Kitagawa, T.; Oguma, M.; Ohmori, Y.; Horiguchi, M. *Electron. Lett.* **1994**, *30*(11), 856–857.

[143] Amarnath, K.; Grover, R.; Kanakaraju, S.; Ping-Tong, H. *IEEE Photonics Technol. Lett.* **2005**, *17*(11), 2280–2282.

[144] Clerk, A. A.; Devoret, M. H.; Girvin, S. M.; Marquardt, F.; Schoelkopf, R. J. *Rev. Mod. Phys.* **2010**, *82*(2), 1155–1208.

[145] Metelmann, A.; Clerk, A. A. *Phys. Rev. Lett.* **2014**, *112*(13), 133904.

[146] Metelmann, A.; Clerk, A. A. *Phys. Rev. X* **2015**, *5*, 021025.

[147] Metelmann, A.; Clerk, A. A. *Phys. Rev. A* **2017**, *95*, 013837.

[148] Ockeloen-Korppi, C. F.; Damskägg, E.; Pirkkalainen, J. M.; Heikkilä, T. T.; Massel, F.; Sillanpää, M. A. *Phys. Rev. X* **2016**, *6*, 041024.

[149] Chien, T.; Lanes, O.; Liu, C.; Cao, X.; Lu, P.; Motz, S.; Liu, G.; Pekker, D.; Hatridge, M. *arXiv: 1903.02102* **2019**.

[150] Vahala, K. *Optical Microcavities;* World Scientific, 2004.

[151] Fan, S.; Suh, W.; Joannopoulos, J. D. *J. Opt. Soc. Am. A* **2003**, *20*(3), 569–572.

[152] Zhong, Q.; Ren, J.; Khajavikhan, M.; Christodoulides, D. N.; Özdemir, Ş. K.; El-Ganainy, R. *Phys. Rev. Lett.* **2019**, *122*(15), 153902.

[153] Hohimer, J. P.; Vawter, G. A.; Craft, D. C. *Appl. Phys. Lett.* **1993**, *62*(11), 1185–1187.

[154] Kharitonov, S.; Bres, C.-S. *Light Sci. Appl.* **2015**, *4*, e340.

[155] Ren, J.; Liu, Y. G. N.; Parto, M.; Hayenga, W. E.; Hokmabadi, M. P.; Christodoulides, D. N.; Khajavikhan, M. *Opt. Express* **2018**, *26*(21), 27153–27160.

[156] Chang, L.; Jiang, X.; Hua, S.; Yang, C.; Wen, J.; Jiang, L.; Li, G.; Wang, G.; Xiao, M. *Nat. Photon.* **2014**, *8*(7), 524–529.

[157] Roy, T.; Kundu, S.; Chand, M.; Vadiraj, A. M.; Ranadive, A.; Nehra, N.; Patankar, M. P.; Aumentado, J.; Clerk, A. A.; Vijay, R. *Appl. Phys. Lett.* **2015**, *107*(26), 262601.

[158] Scully, M. O.; Zubairy, M. S. *Quantum Optics;* Cambridge University Press, first ed., 1997.

[159] Shi, C.; Dubois, M.; Chen, Y.; Cheng, L.; Ramezani, H.; Wang, Y.; Zhang, X. *Nat. Comm.* **2016**, *7*, 11110.

[160] Assawaworrarit, S.; Yu, X.; Fan, S. *Nature* **2017**, *546*, 387–390.

[161] Chitsazi, M.; Li, H.; Ellis, F. M.; Kottos, T. *Phys. Rev. Let.* **2017**, *119*(9), 093901.

[162] Leykam, D.; Bliokh, K. Y.; Huang, C.; Chong, Y. D.; Nori, F. *Phys. Rev. Lett.* **2017**, *118*(4), 040401.

[163] Hu, W.; Wang, H.; Shum, P. P.; Chong, Y. D. *Phys. Rev. B* **2017**, *95*(18), 184306.

Appendix A

Letters of Permission

A.1 Permission for use of materials in Chapter 2

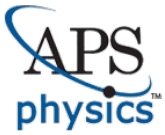

American Physical Society
Reuse and Permissions License

28-Jun-2019

This license agreement between the American Physical Society ("APS") and Qi Zhong ("You") consists of your license details and the terms and conditions provided by the American Physical Society and SciPris.

Licensed Content Information

License Number:	**RNP/19/JUN/016152**
License date:	28-Jun-2019
DOI:	10.1103/PhysRevA.97.020105
Title:	Power-law scaling of extreme dynamics near higher-order exceptional points
Author:	Q. Zhong et al.
Publication:	Physical Review A
Publisher:	American Physical Society
Cost:	USD $ 0.00

Request Details

Does your reuse require significant modifications: No

Specify intended distribution locations:	United States
Reuse Category:	Reuse in a thesis/dissertation
Requestor Type:	Author of requested content
Items for Reuse:	Whole Article
Format for Reuse:	Electronic and Print
Total number of print copies:	Up to 1000

Information about New Publication:

University/Publisher:	Michigan Technological University
Title of dissertation/thesis:	The physics and applications of exceptional points
Author(s):	Qi Zhong
Expected completion date:	Aug. 2019

License Requestor Information

Name:	Qi Zhong
Affiliation:	Individual
Email Id:	qizhong@mtu.edu
Country:	United States

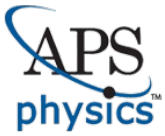

American Physical Society
Reuse and Permissions License

TERMS AND CONDITIONS

The American Physical Society (APS) is pleased to grant the Requestor of this license a non-exclusive, non-transferable permission, limited to Electronic and Print format, provided all criteria outlined below are followed.

1. You must also obtain permission from at least one of the lead authors for each separate work, if you haven't done so already. The author's name and affiliation can be found on the first page of the published Article.
2. For electronic format permissions, Requestor agrees to provide a hyperlink from the reprinted APS material using the source material's DOI on the web page where the work appears. The hyperlink should use the standard DOI resolution URL, http://dx.doi.org/{DOI}. The hyperlink may be embedded in the copyright credit line.
3. For print format permissions, Requestor agrees to print the required copyright credit line on the first page where the material appears: "Reprinted (abstract/excerpt/figure) with permission from [(FULL REFERENCE CITATION) as follows: Author's Names, APS Journal Title, Volume Number, Page Number and Year of Publication.] Copyright (YEAR) by the American Physical Society."
4. Permission granted in this license is for a one-time use and does not include permission for any future editions, updates, databases, formats or other matters. Permission must be sought for any additional use.
5. Use of the material does not and must not imply any endorsement by APS.
6. APS does not imply, purport or intend to grant permission to reuse materials to which it does not hold copyright. It is the requestor's sole responsibility to ensure the licensed material is original to APS and does not contain the copyright of another entity, and that the copyright notice of the figure, photograph, cover or table does not indicate it was reprinted by APS with permission from another source.
7. The permission granted herein is personal to the Requestor for the use specified and is not transferable or assignable without express written permission of APS. This license may not be amended except in writing by APS.
8. You may not alter, edit or modify the material in any manner.
9. You may translate the materials only when translation rights have been granted.
10. APS is not responsible for any errors or omissions due to translation.
11. You may not use the material for promotional, sales, advertising or marketing purposes.
12. The foregoing license shall not take effect unless and until APS or its agent, Aptara, receives payment in full in accordance with Aptara Billing and Payment Terms and Conditions, which are incorporated herein by reference.
13. Should the terms of this license be violated at any time, APS or Aptara may revoke the license with no refund to you and seek relief to the fullest extent of the laws of the USA. Official written notice will be made using the contact information provided with the permission request. Failure to receive such notice will not nullify revocation of the permission.
14. APS reserves all rights not specifically granted herein.
15. This document, including the Aptara Billing and Payment Terms and Conditions, shall be the entire agreement between the parties relating to the subject matter hereof.

A.2 Permission for use of materials in Chapter 3

Title:	Crossing exceptional points without phase transition
Author:	Qi Zhong et al
Publication:	Scientific Reports
Publisher:	Springer Nature
Date:	Jan 15, 2019

Creative Commons

A.3 Permission for use of materials in Chapter 4

Title:	Winding around non-Hermitian singularities
Author:	Qi Zhong et al
Publication:	Nature Communications
Publisher:	Springer Nature
Date:	Nov 15, 2018

Creative Commons

A.4 Permission for use of materials in Chapter 5

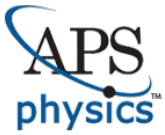

American Physical Society
Reuse and Permissions License

28-Jun-2019

This license agreement between the American Physical Society ("APS") and Qi Zhong ("You") consists of your license details and the terms and conditions provided by the American Physical Society and SciPris.

Licensed Content Information

License Number:	**RNP/19/JUN/016155**
License date:	28-Jun-2019
DOI:	10.1103/PhysRevLett.122.153902
Title:	Sensing with Exceptional Surfaces in Order to Combine Sensitivity with Robustness
Author:	Q. Zhong et al.
Publication:	Physical Review Letters
Publisher:	American Physical Society
Cost:	USD $ 0.00

Request Details

Does your reuse require significant modifications: No

Specify intended distribution locations:	United States
Reuse Category:	Reuse in a thesis/dissertation
Requestor Type:	Author of requested content
Items for Reuse:	Whole Article
Format for Reuse:	Print and Electronic
Total number of print copies:	Up to 1000

Information about New Publication:

University/Publisher:	Michigan Technological University
Title of dissertation/thesis:	The physics and applications of exceptional points
Author(s):	Qi Zhong
Expected completion date:	Aug. 2019

License Requestor Information

Name:	Qi Zhong
Affiliation:	Individual
Email Id:	qizhong@mtu.edu
Country:	United States

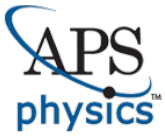

American Physical Society
Reuse and Permissions License

TERMS AND CONDITIONS

The American Physical Society (APS) is pleased to grant the Requestor of this license a non-exclusive, non-transferable permission, limited to Print and Electronic format, provided all criteria outlined below are followed.

1. You must also obtain permission from at least one of the lead authors for each separate work, if you haven't done so already. The author's name and affiliation can be found on the first page of the published Article.
2. For electronic format permissions, Requestor agrees to provide a hyperlink from the reprinted APS material using the source material's DOI on the web page where the work appears. The hyperlink should use the standard DOI resolution URL, http://dx.doi.org/{DOI}. The hyperlink may be embedded in the copyright credit line.
3. For print format permissions, Requestor agrees to print the required copyright credit line on the first page where the material appears: "Reprinted (abstract/excerpt/figure) with permission from [(FULL REFERENCE CITATION) as follows: Author's Names, APS Journal Title, Volume Number, Page Number and Year of Publication.] Copyright (YEAR) by the American Physical Society."
4. Permission granted in this license is for a one-time use and does not include permission for any future editions, updates, databases, formats or other matters. Permission must be sought for any additional use.
5. Use of the material does not and must not imply any endorsement by APS.
6. APS does not imply, purport or intend to grant permission to reuse materials to which it does not hold copyright. It is the requestor's sole responsibility to ensure the licensed material is original to APS and does not contain the copyright of another entity, and that the copyright notice of the figure, photograph, cover or table does not indicate it was reprinted by APS with permission from another source.
7. The permission granted herein is personal to the Requestor for the use specified and is not transferable or assignable without express written permission of APS. This license may not be amended except in writing by APS.
8. You may not alter, edit or modify the material in any manner.
9. You may translate the materials only when translation rights have been granted.
10. APS is not responsible for any errors or omissions due to translation.
11. You may not use the material for promotional, sales, advertising or marketing purposes.
12. The foregoing license shall not take effect unless and until APS or its agent, Aptara, receives payment in full in accordance with Aptara Billing and Payment Terms and Conditions, which are incorporated herein by reference.
13. Should the terms of this license be violated at any time, APS or Aptara may revoke the license with no refund to you and seek relief to the fullest extent of the laws of the USA. Official written notice will be made using the contact information provided with the permission request. Failure to receive such notice will not nullify revocation of the permission.
14. APS reserves all rights not specifically granted herein.
15. This document, including the Aptara Billing and Payment Terms and Conditions, shall be the entire agreement between the parties relating to the subject matter hereof.